

DESIGN FUNDAMENTALS OF PLASMONIC SUBSTRATES FOR SURFACE-ENHANCED RAMAN SCATTERING APPLICATIONS

by

Raymond A. Velez Calder

A dissertation submitted in partial fulfillment of the requirements for the degree of

DOCTOR OF PHILOSOPHY

in

Applied Chemistry

UNIVERSITY OF PUERTO RICO

MAYAGÜEZ CAMPUS

2019

Approved by:

Marco A. De Jesus Ruiz, PhD.
President, Graduate Committee

Date

Marisol Vera Colon, PhD,
Member, Graduate Committee

Date

Nilka M. Rivera Portalatin, PhD.
Member, Graduate Committee

Date

Enrique Melendez Martinez, PhD
Member, Graduate Committee

Date

Fernando J. Perez Muñoz, PhD
Representative of Graduate Studies

Date

Enrique Melendez Martinez, PhD
Chairperson of the Department

Date

ABSTRACT

The use of nanomachining methods capable of reproducible construction of nano-arrayed devices have revolutionized the field of plasmonic sensing through the introduction of rationally engineered designs. Significant strides have been made to fabricate plasmonic platforms with tailored interparticle gaps to improve their performance for surface enhanced Raman scattering (SERS) applications. Attention has now been focused on predictive modelling, such as Finite-Difference Time-Domain (FDTD), a promising tool that can advance the optimization of the SERS substrate design process by simulating the plasmonic response induced by an EM wave.

Over time a dichotomy has emerged in the implementation of SERS for analytical applications, the construction of substrates, optimization of interparticle spacing as a mean to optimize electromagnetic field-enhancement at the localized surface plasmon level, and the substrate sensitivity over extended areas to achieve quantitative performance. Furthermore, the figures of merits used to validate the SERS activity can be subject to some scrutiny due to signal enhancement mechanisms that are overlooked. Hereon is discussed several fundamental key aspects for the design of plasmonic substrates for SERS applications. FDTD case studies will be discussed thus demonstrating the importance of models for a successful design of a SERS substrate.

FDTD was used to address the plasmonic performance of a hybrid nanoarray sensing platform comprised of hexagons and ellipses. The device had already been fabricated, hence making it impossible to ascertain the contributions of each feature to the SERS experimental data. The modelling data provided valuable insight of the underlying effect that the excitation

wavelength had on the substrate. Furthermore, the plasmonic coupling of the features in the hybrid device was demonstrated thereby providing valuable insight of the excellent performance demonstrated by this design at multiple excitation wavelengths.

Finally, the SERS substrate enhancement factor (SSEF) for plasmonic Ag/SiO₂/Si Disc-on-Pillar arrays of variable pitch were contrasted with the analytical performance for quantitative applications. Experimental data were compared with those from FDTD simulations used in the optimization of the array dimensions. A self-assembled monolayer (SAM) of benzenethiol rendered highly reproducible signals (RSD ~ 4% to 10%) and EF values in the orders of 10⁶ to 10⁸ for all pitches. A remarkable correlation was observed between the modelling and the SERS experimental data after normalization with the illuminated pillars. Spectra corresponding to rhodamine 6G and 4-aminobenzoic acid demonstrated the advantages of using the more densely-packed DOP arrays (gap = 40 nm) for quantitation in spite that the strongest SSEF was attained for an interpillar gap of 400 nm.

RESUMEN

El uso de métodos capaces de construir nano-arreglos de manera reproducible ha revolucionado el campo de sensores plasmonicos con diseños radicales. Avances significativos para la fabricación de plataformas plasmonicas con el espacio entre partículas optimizadas para *Surface-Enhanced Raman Scattering* (SERS). Se ha tomado un giro hacia el modelaje predictivo, como lo es *Finite-Difference Time-Domain*, FDTD, como una herramienta prometedora para avanzar la optimización de los sustratos SERS a través de la simulación de las respuestas electromagnética.

Al pasar el tiempo ha surgido una dicotomía en la implementación de SERS para aplicaciones analíticas, la construcción de sustratos, la optimización de las dimensiones para optimizar la magnificación de los campos electromagnéticos y la extensión de la sensibilidad del sustrato para alcanzar un rendimiento cuantitativo. Mas aun, las figuras de mérito utilizadas para validar la actividad SERS han estado sujetas fuerte examinación dado que no se siempre se contemplan los mecanismos que resultan en una magnificación de la señal. De aquí comienza una discusión sobre los aspectos fundamentales para el diseño de un sustrato tipo plasmonicos para aplicaciones de SERS. Algunos casos de estudios se presentarán que demostrarán la importancia de los modelos para obtener exitosamente un diseño de un sustrato de SERS.

FDTD fue utilizado para atender la actividad plasmonicos de una plataforma de nano arreglos híbridos compuestas de hexágonos y elipses. El aparato había sido fabricado, por lo tanto, se hacía difícil poder de cifrar sus características que contribuyeron a la data experimental recopilada con SERS. La data de modelaje proveyó una visión valiosa de los efectos subyacentes que podría tener el largo de onda de excitación en el sustrato. Mas aun, el acoplamiento de los

nano arreglos híbridos fue demostrado proveyendo a su vez una clara razón de la ejecutoria excelente de un sustrato diseñado para múltiples largos de onda.

Finalmente, se hace un contraste del *SERS Substrate Enhancement Factor* (SSEF) y la ejecutoria analítica para nano-arreglos tipo plasmonicos de Disco-Sobre-Pillar (referido como DOP por sus siglas en inglés) compuesto de Ag/SiO₂/Si y de variable periodicidad para aplicaciones analíticas. Data experimental fue comparada con las simulaciones de FDTD utilizada para optimizar el sustrato. Una monocapa de tiol de benceno rindió señales altamente reproducibles (%RSD ~ 4% a 10%) y valores de SSEF en el orden de 10⁶ a 10⁸ para todas las periodicidades. Una correlación extraordinaria se observó entre los datos experimentales y las simuladas luego de normalizar las data por la cantidad de pilares iluminados. Los espectros de rodamina 6g y acido 4-aminobenzoico demostraron las ventajas de utilizar los arreglos de DOP más densamente empacados (espacio entre pilares = 40 nm) para propósitos de cuantificación a pesar de que el SSEF más fuerte corresponde al espacio entre pilares de 400 nm.

Copyright © 2019

by

Raymond Alexander Velez Calder

*First and foremost:
To the Creator of Light,
To the Light of the World,
To the Light that shows me the path,
and especially,
To the source of the Light shining within my heart:
My loving wife, Marisely,
my 1st born, Alanna Valentina,
my 2nd born, Liam Andres.*

ACKNOWLEDGEMENTS

I am forever grateful to the “Big Guy from Above.” Without Him, nothing could ever be accomplished. He has always sought a way to shine upon me. He never ceases to surprise me.

I am eternally thankful to my loving wife, Marisely Figueroa, whom has walked next to me (so I don’t feel alone), behind me (when I’ve needed a push), and in front of me (when I needed someone to pull me out). Patience has always been one of her virtues, and it has definitely paid off as we reach the end of this very important stage of our life and prepare for the next “Only-God-knows-what” mission that awaits us. I am also grateful to my family and friends that have been there one way or another (especially those anonymous heroes). My kids, Alanna Valentina and Liam Andres, for although they have no idea how to read this, they sure have been there through my countless hours of reading and writing. Granted that “playtime with daddy” was accompanied with a laptop and/or several articles, they were absolutely inspirational (especially when Alanna wanted her own keyboard so she could type things when I was writing the manuscript).

There are many other family and friends (there are far too many to mention), but I cannot let pass by this opportunity to capture just a handful: Raymond Geronimo (Gerry), Elizabeth Olan (mother sent from above), Osvaldo De Jesus (Ovy), Jorge Olan (Gogo), Sonia Olan, Wilfredo Figueroa, Magdaly Gonzalez, my peers and friends at HP, my colleagues from UTK (Sepaniak’s Lab), and my mentors at ORNL (Nick and Ivan).

I would like to thank each of my committee members: Dr. Marco De Jesus, Dr. Marisol Vera, Dr. Enrique Melendez, and Dr. Nilka Rivera Portalatin. Your patience and unique way of

teaching has forged a new set of skills that I may use (if not already) for many aspects of life.

Thank you.

A very special thanks to Dr. Marco De Jesus (my chairman, mentor, and friend) and Dr. Michael J. Sepaniak (mentor and advisor @UTK). The MS was actually warming up for what awaited me at the PhD. It has been an honor to have worked with you both. There are many valuable lessons learned and I am confident that we will cross paths again... but this time not as a padawan studying for an exam, trying to recover corrupted or lost files (I should consider buying a typewriter), or disrupting my learning curve so as to make it stand at 90°.

Finally, I would like to acknowledge the following whom believed in me enough to fund my research and/or to give me a job so that I may support my family:

- UPRM RISE-2-Best Biomedical Research Program (NIH Grant 1R25GM088023), PI (Juan Lopez Garriga, PhD), and Supporting Staff (Rosalie Ramos, Mairim Romero)
- U.S. Department of Energy, Savannah River (Grant DE-FG09-07SR22571)
- Department of Chemistry @ UPRM (Francheska Becerra)
- University of Puerto Rico, Mayagüez Campus
- HP, Inc (Aguadilla, PR)

TABLE OF CONTENTS

| | | |
|----------|---|-----------|
| 1 | INTRODUCTION..... | 1 |
| 1.1 | ELECTROMAGNETIC RADIATION | 1 |
| 1.1.1 | <i>Light as a Wave</i> | 2 |
| 1.1.2 | <i>Light as a Particle</i> | 8 |
| 1.2 | RAMAN | 9 |
| 1.3 | SURFACE-ENHANCED RAMAN SCATTERING (SERS) | 15 |
| 1.3.1 | <i>Chemical Enhancement (CE)</i> | 17 |
| 1.3.2 | <i>Electromagnetic Enhancement (EM)</i> | 19 |
| 1.3.3 | <i>Enhancement Factor</i> | 22 |
| 1.4 | FINITE-DIFFERENCE TIME-DOMAIN (FDTD) | 23 |
| 2 | FDTD PLASMONIC SIMULATIONS OF HYBRID MORPHOLOGY NANOARRAYS | 26 |
| 2.1 | INTRODUCTION | 27 |
| 2.2 | FDTD MODELLING PARAMETERS..... | 28 |
| 2.3 | FDTD MODELLING PROJECTIONS..... | 30 |
| 3 | FDTD MODELLING FOR OPTIMIZATION OF DISC-ON-PILLAR (DOP) PLASMONIC ARRAYS | 38 |
| 3.1 | INTRODUCTION | 39 |
| 3.2 | FDTD MODELLING AND PROJECTIONS | 39 |
| 4 | SURFACE-ENHANCED RAMAN SCATTERING STUDIES OF DISC-ON-PILLAR (DOP) ARRAYS: CONTRASTING ENHANCEMENT FACTOR WITH ANALYTICAL PERFORMANCE | 46 |
| 4.1 | INTRODUCTION | 47 |
| 4.2 | EXPERIMENTAL SECTION | 49 |
| 4.2.1 | <i>Disc-on-Pillar (DOP) Fabrication</i> | 49 |
| 4.2.2 | <i>SERS Substrates and Standards</i> | 53 |
| 4.2.3 | <i>Calibration Sensitivity (σ)</i> | 53 |
| 4.2.4 | <i>SERS Assessment</i> | 54 |
| 4.2.5 | <i>Raman Operational Parameters</i> | 57 |
| 4.3 | RESULTS AND DISCUSSION..... | 57 |
| 4.3.1 | <i>SERS Performance of DOP Arrays</i> | 57 |
| 4.3.1.1 | DOP Arrays: 2×2 , 4×4 , and 8×8 | 58 |
| 4.3.1.2 | DOP Region: $24 \mu\text{m} \times 24 \mu\text{m}$ | 60 |
| 4.3.2 | <i>Effects of Array Order on SERS Response</i> | 65 |
| 4.3.3 | <i>DOP Analytical Performance</i> | 67 |

| | | |
|----------|---|-----------|
| 4.3.4 | <i>DOP performance with R6G</i> | 67 |
| 4.3.5 | <i>DOP performance with 4-ABA</i> | 72 |
| 5 | CONCLUDING REMARKS | 74 |
| 6 | RECOMMENDATIONS FOR FUTURE WORKS | 76 |
| | REFERENCES | 79 |
| | APPENDIX | 86 |

LIST OF TABLES

| | |
|---|----|
| Table 2-1: Score card for $ E/E_0 ^2$ per morphology feature and excitation source. | 36 |
| Table 2-2: Contrast between FDTD Modelling projections and SERS Data ⁴⁴ | 37 |
| Table 4-1: Disc-on-Pillar (DOP) Periodic Spatial Dimensions | 51 |
| Table 4-2: DOP dimensions measured for pillar arrays ($n \times n$) or pillar regions (μm^2). Values correspond to target dimension / actual dimension with standard deviation ($n = 5$). | 52 |
| Table 4-3: DOP Pitch Order Response Factor for arrays with a 520 nm pitch. | 65 |

LIST OF FIGURES

| | |
|--|----|
| Figure 1-1: Electromagnetic Spectrum of Light. Schematic from Reference [1]..... | 2 |
| Figure 1-2: Demonstration of Gauss's law of electric fields with a dielectric system. The perturbation of the system by an electric field induces polarization of the internal charges. This regulates the flow of the electric field as it travels through the dielectric material. Schematic taken from Reference [5]..... | 4 |
| Figure 1-3: Schematic of magnet showing the direction the magnetic flux from the north pole to the south pole consistent with Gauss's Law of Magnetism..... | 5 |
| Figure 1-4: Oscillating electromagnetic wave propagating in direction k . Schematic taken from reference [1]..... | 7 |
| Figure 1-5: Schematic representation of a typical Raman spectrometer. The incident source of energy is represented by the red lines and the scattered energy is shown by the light orange lines. Optical components commonly used are shown such as the bandpass filter (used to clean the incident laser line), the Neutral Density Filter (which attenuates the incident energy), and the Edge Filter (that suppresses the incident wavelength thus allowing for the scattered frequencies to continue towards the spectrograph and detector)..... | 10 |
| Figure 1-6: Schematic representation of the different scattering processes as proposed by C. V. Raman: Stokes (Raman), Rayleigh, and anti-Stokes (Raman). Schematic from Reference [14]..... | 11 |
| Figure 1-7: Brief chronological summary of the pioneering of Surface-Enhanced Raman Scattering (SERS)..... | 16 |
| Figure 1-8: Chemical Enhancement mechanism in which (a) the resonant charge transfer is initiated by a photon creating an electron-hole pair; (b) the electron is transferred from the metal to the adsorbate; (c) relaxation of the excited molecule transfers returns an electron with adsorbate intrinsic information to the metal; and (d) electron recombines with the hole in the metal releasing a photon which carries vibrational frequencies of the adsorbate. Schematic taken from Reference [33]..... | 18 |
| Figure 1-9: Schematic of chemical enhancement via electron transfer at the Fermi level. Schematic taken from Reference [24]..... | 19 |
| Figure 1-10: Schematic of strong localization of surface plasmon in surface cavities. Schematic taken from Reference [37]. | 20 |

| | |
|---|----|
| Figure 1-11: Schematic representation of (a) SPP propagation across a substrate and (b) the induced EM field confined by the particle geometry thereby generating a LSPR. Schematic taken from reference [37]. | 21 |
| Figure 1-12: General schematic to solve for Maxwell's equations using a Yee cell. ³⁹ (a) A three-dimensional problem space divided into many cubic cells. (b) A single unit cell depicting the location of the electric fields ($E_{x,y,x}$) and magnetic fields ($H_{x,y,z}$). | 25 |
| Figure 2-1: Hybrid morphology nanoarrays used for plasmonic sensing applications. | 27 |
| Figure 2-2: Lumerical [®] FDTD platform depicting the hybrid morphology nanoarray and simulation components: monitors (yellow), simulation mesh regions (orange), and source (blue/violet arrows). | 29 |
| Figure 2-3: (Left): Schematic cross section of PEH nanoarray structural components used FDTD modelling. The following dimensions correspond to t = thickness, h = height: (a) Ag disk, $h = 25$ nm; (b) SiO ₂ on pillar top, $h = 20$ nm; (c) SiO ₂ on sidewalls, $h = 250$ nm, $t = 20$ nm; (d) Si pillar, $h = 250$ nm, (e) Ag mirror, $h = 25$ nm; (f) SiO ₂ on etched wafer surface, $h = 20$ nm. (Right) Schematic of hybrid nanoarray layout with a 200 nm gap in the point closest between both features. All dimensions are given in nm. The same setup is used for the single feature system. | 30 |
| Figure 2-4: FDTD data depicting $ E/E_0 ^2$ as a function of wavelength for the hybrid nanoarray consisting of hexagons and ellipses. Gray vertical lines indicate target excitation wavelengths. | 31 |
| Figure 2-5: FDTD data depicting $ E/E_0 ^2$ as a function of wavelength for the nanoarrays consisting of either hexagons or ellipses. Gray vertical lines indicate target excitation wavelengths for SERS applications. | 32 |
| Figure 2-6: FDTD $ E/E_0 ^2$ distribution at the xy plane for the simulated array systems: Hexagon (left), PEH Hybrid morphology (middle), and Ellipse (right). The resonance plasmons were induced using excitation sources: 780 nm (top row), 635 nm (middle row), and 528 nm (bottom row). The source polarization vector is indicated by the red arrow. | 34 |
| Figure 2-7: FDTD $ E/E_0 ^2$ distribution at the xz plane for the simulated array systems: Hexagon (left), PEH Hybrid morphology (middle), and Ellipse (right). The resonance plasmons were induced using excitation sources: 780 nm (top row), 635 nm (middle row), and 528 nm (bottom row). The source polarization vector is indicated by the red arrow. | 35 |
| Figure 3-1: Schematic of DOP structural components used FDTD modelling. The following dimensions correspond to d = diameter, h = height, i.d. = inner diameter, and o.d. = outer diameter: (a) Ag disk, $h = 25$ nm, $d = 120$ nm; (b) SiO ₂ on pillar top, $h = 20$ nm, $d = 120$ nm; (c) SiO ₂ on pillar sidewalls, $h = 155$ nm, $d = 155$ nm, i.d./o.d. = 80 nm / 100 nm; (d) Si | |

pillar, $h = 175$ nm, $d = 80$ nm; (e) Ag mirror, $h = 25$ nm, i.d. / o.d. = 120 nm / 4000 nm; (f) SiO₂ on etched wafer surface, $h = 20$ nm, $d = 1000$ nm. 40

Figure 3-2: (a) Schematic of the DOP structure with simulation components used for FDTD modelling. The yellow lines represent the location of the different monitors used. Simulation mesh areas are defined by orange boxes. (b) Near-field intensity color maps (log10 scale) as rendered by the X-Z monitor for DOP arrays with a 570 nm pitch at 630 nm incident wavelength. (c) Near-field intensity color maps (log10 scale) produced by the X-Y monitor for DOP arrays with a 570 nm pitch at 630 nm incident wavelength. The red arrows in (b) and (c) indicate the direction of the polarization vector..... 42

Figure 3-3: FDTD modelling and projections. (a) $|E/E_0|^2$ vs. Excitation wavelength for all DOP; (b) Insert corresponds to $|E/E_0|^2$ vs. Excitation wavelength for a single DOP and p160 to p240; (c) Scatter plot for $|E/E_0|^2_{\max}$ vs. Excitation wavelength for all simulated pitches; (d) Projected $|E/E_0|^2$ with a simulated excitation source of 630 nm. 43

Figure 3-4: Scatter plot for $|E/E_0|^2_{\max}$ vs. Excitation wavelength for all simulated pitches..... 45

Figure 3-5: Projected $|E/E_0|^2$ with a simulated excitation source of 630 nm. 45

Figure 4-1: General fabrication summary of DOP periodic arrays (Drawings are not to scale). (a) Previously cleaned Si Wafer; (b) Addition of ZEP520A photoresist; (c) EBL-imprinting pattern; (d) Development and descuming; (e) Application of Cr mask; (f) Substrate after Lift-off; (g) Etched Si wafer; (h) After Cr stripping; (i) SiO₂ layer growth; (j) Metallization via PVD..... 50

Figure 4-2: Si/SiO₂ DOP periodic arrays for (a) $p = 520$ nm, 2×2 ; (b) $p = 520$ nm, 8×8 ; (c) $p = 520$ nm, 8×8 (closer view of array) ; (d) $p = 160$ nm, 4×4 ; (e) $p = 160$ nm, 8×8 ; and (f) $24 \mu\text{m} \times 24 \mu\text{m}$ region with p160 DOPs. Dimensions are described in Table 4-2. 52

Figure 4-3: (a) SERS mapping of $24 \mu\text{m} \times 24 \mu\text{m}$ DOP region using $1 \mu\text{m}$ steps. The weaker response noticed at the initial $2 \mu\text{m}$ of the array perimeter is consistent with a $2 \mu\text{m}$ diameter beam spot that is scanning at $1 \mu\text{m}$ steps. The map shows the signal of the C-S band across the DOP system which suggest a consistent adsorption of BT at the Ag disc surface. (b) Mean SERS spectra of the $24 \mu\text{m} \times 24 \mu\text{m}$ DOP region using $1 \mu\text{m}$ steps at p160 and p520. The Ag mirror surrounding the pillar arrays is depicted by the lower four spectra and do not render a SERS active signal..... 62

Figure 4-4: (top) BT SERS response for $24 \mu\text{m} \times 24 \mu\text{m}$ arrays measured around the center of the region. Error bars correspond to a standard deviation of 3 measurements with a CV of the SERS response ranging from 1.5% to 5.2% for each pitch. (middle) MAP as a function of pitch for a $2.0 \mu\text{m}$ laser beam spot. (bottom) BT SERS response after normalization with MAP and calculated SSEF..... 64

Figure 4-5: (a) SERS spectra for R6G (1.19×10^{-3} M) for a center measurement of the $24 \mu\text{m} \times 24 \mu\text{m}$ region for p140, p160, p270, p520, and p870 arrays. (b) 773 cm^{-1} band corresponding to the R6G xanthene in-plane bending. Spectra were polynomial baseline corrected. All spectra are offset in the y-axis for clarity..... 69

Figure 4-6: R6G working curves (5.95×10^{-6} M to 1.19×10^{-3} M) using (a) p160 and (b) p520. The error bars for both p160 and p520 correspond to duplicate measurements at each calibration level. The dashed blue lines are the linear best fit for each period. Signal saturation for the 773 cm^{-1} band is estimated at 1.44×10^{-4} M for p520 (vertical dash-dot-dash line in graph b)..... 70

Figure 4-7: Contrasting SERS spectra of 4-aminobenzoic acid obtained using $24 \mu\text{m} \times 24 \mu\text{m}$ DOP regions with a pitch of 160 nm and 520 nm. The spectra are offset in the y-axis for clarity. 73

Figure 6-1: Proposed conformation for PEH arrays in which transversal axis of the hexagon and ellipse (indicated by green dashed arrow) are aligned with the polarization vector (red arrow) in order to enhance the plasmonic response..... 77

Figure 6-2: Proposed Nanoarrays for increased plasmonic sensing and feasible manufacturing based on current studies performed. 78

LIST OF APPENDIX

| | |
|---|----|
| APPENDIX..... | 86 |
| APPENDIX 1. BT SAM TEMPORAL STUDY..... | 87 |
| APPENDIX 2. MAXIMUM ALLOWABLE PILLARS (MAP) | 92 |
| APPENDIX 3. DOP ARRAYS: SUPPLEMENTAL INFORMATION | 94 |
| APPENDIX 4. DOP PITCH ORDER RESPONSE FACTOR (Φ)..... | 98 |

LIST OF ABBREVIATIONS

| | |
|-------------------|---|
| 4-ABA | 4-aminobenzoic acid |
| 4-ABT | 4-aminobenzenethiol |
| Ag | silver |
| A _L | area of laser spot |
| ALD | atomic layer deposition |
| A _P | area occupied by one pillar |
| A _{top} | Area of disc top |
| a.u. | arbitrary units |
| A _{wall} | Area disc side wall |
| BT | benzenethiol |
| <i>c</i> | speed of light in vacuum, 3.0×10^8 m/s |
| CCD | Charge Coupled Device |
| CE | Chemical Enhancement |
| cm ⁻¹ | reciprocal centimeters |
| cnts/s | counts per second |
| Cr | chromium |
| C-S | carbon-sulfur bond |
| CV | Coefficient of Variation |
| DIW | deionized water |
| DOP | Disc-on-Pillar |
| E | Energy |

| | |
|-------------------|---|
| EBL | Electron Beam Lithography |
| EF | Enhancement Factor |
| EM | Electromagnetic |
| EMF | electromagnetic field |
| EtOH | ethanol |
| F | fluorine |
| FDTD | Finite-Difference Time-Domain |
| HeNe | Helium-Neon laser |
| HOMO | Highest Occupied Molecular Orbital |
| IPA | isopropyl alcohol |
| I_{surf} | SERS response of molecules |
| I_{t15} | C-S band intensity for the incubation times at 15 minutes |
| I_{t1200} | C-S band intensity for the incubation times at 1200 minutes |
| I_{vol} | normal Raman response of molecules |
| J | Joules |
| kcal/mol | kilocalories per mol |
| kV | kilovolts |
| LSP | Localized Surface Plasmon |
| LSPR | Localized Surface Plasmon Resonance |
| LUMO | Lowest Unoccupied Molecular Orbital |
| m | meters |
| M | mol/L |

| | |
|-------------------|---|
| MAP | Maximum Allowable Pillars |
| mW | milliwatts |
| nm | nanometers |
| N ₂ | gaseous nitrogen |
| NA | numerical aperture |
| N _{surf} | Average number of molecules adsorbed on the substrate surface |
| N _{vol} | Average number of molecules per scattering volume |
| PBC | Periodic Boundary condition |
| PEH | Parallel Ellipse Hexagon |
| PML | Perfectly Matched Layer |
| PVD | physical vapor deposition |
| R ² | Correlation Coefficient |
| R6G | rhodamine 6G |
| r _L | laser spot radius |
| s | seconds |
| SAM | self-assembled monolayer |
| SCS | Single Crystal Silicon |
| SEF | SERS Enhancement Factor |
| SSEF | SERS Substrate Enhancement Factor |
| SEM | scanning electron microscope |
| SERS | Surface-Enhanced Raman Scattering |
| Si | silicon |

| | |
|------------------|---------------------------|
| SiO ₂ | silicon dioxide |
| SPP | Surface Plasmon Polariton |
| <i>t</i> | time |
| t15 | 15 minutes |
| t1200 | 1200 minutes |
| WD | working distance |

LIST OF SYMBOLS

| | |
|-------------------------|---|
| \AA | angstrom |
| r_{eq} | bond length at equilibrium |
| ν_j | bond vibrational frequency |
| σ | calibration sensitivity |
| $(r - r_{eq})$ | change in bond length |
| \cos | cosine |
| C | Coulombs+ |
| $\vec{\nabla} \times$ | Curl Operator |
| $^{\circ}\text{C}$ | degrees Celsius |
| Δ | delta |
| ΔG_{ads} | delta Gibbs adsorption energy |
| $\vec{\nabla} \cdot$ | divergence operator |
| Φ | DOP pitch order response factor |
| ρ_v | electric charge density, C/m^3 |
| \vec{J} | electric current density |
| \vec{E} | electric field |
| E_0 | electric field amplitude |
| \vec{D} | electric flux density, C/m^2 |
| λ_0 | excitation source wavelength |
| ν | frequency or wavenumber, cm^{-1} |

| | |
|--------------------|--|
| λ | lambda, wavelength, nm |
| \vec{B} | magnetic flux density |
| \vec{H} | magnetic field |
| μ | magnitude of dipole moment |
| $ E/E_0 _{\max}^2$ | maximum near field enhancement |
| r_{\max} | maximum separation distance between bonded atoms |
| λ_{\max} | maximum wavelength |
| μm | micrometers |
| $ E/E_0 ^2$ | near field enhancement |
| ∂^2 | partial second derivative |
| μ_r | permeability |
| μ_0 | permeability of free space |
| ϵ_r | permittivity or dielectric constant |
| ϵ_0 | permittivity of free space |
| π | pi |
| h | Plank's constant, 6.626×10^{-34} J·s |
| α_0 | polarizability at equilibrium |
| α | polarizability of the molecule |
| ν' | scattered photon frequency |
| E' | scattered energy of the molecule |
| $\nu_{\text{C-S}}$ | vibrational frequency of C-S |

1 INTRODUCTION

Spectroscopy comprises analytical techniques that study the interactions of light with matter. It is well known that light has a dual nature where it can behave like a particle and a wave. Spectroscopy capitalizes on both these characteristics in order to obtain intrinsic information of any given physical system studied. In general, an external source generates the electromagnetic radiation of which the initial energy undergoes changes that are induced by the system components. These energy differences can be associated to molecular properties such as atomic structure, intermolecular bonds, and intramolecular interactions. Hereon is discussed the key aspects pertaining to electromagnetic radiation that are pivotal for a fundamental understanding of vibrational spectroscopic techniques corresponding to Raman and Surface-Enhanced Raman Scattering (SERS). Also, the predictive nature of Finite-Difference Time-Domain (FDTD) simulations for the propagation of the electromagnetic waves for prototype SERS substrates is presented.

1.1 Electromagnetic Radiation

Light is generally associated to a tangible effect of energy that is visually appreciated by the most common detector known to mankind: the human eye. Yet, it is well known amongst the scientific community that light is composed of radiation that is invisible and visible, where the latter corresponds to a significantly small amount of the electromagnetic spectrum (Figure 1-1).¹ Also, it has been well established that light has a dual nature where it is comprised of waves

(electromagnetic) and particles (photons).^{2, 3} The different components of the duality of light were introduced independently by James C. Maxwell, Max Plank, and Albert Einstein.

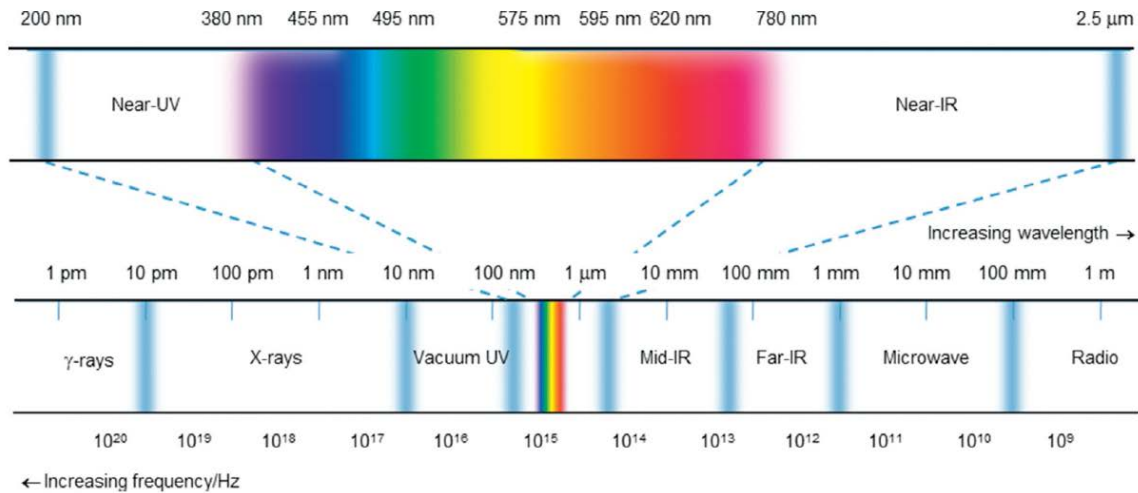


Figure 1-1: Electromagnetic Spectrum of Light. Schematic from Reference [1].

1.1.1 Light as a Wave

James Clerk Maxwell reported his *dynamical theory of the electromagnetic field* in 1865.⁴ He believed that distant particles could act upon each other, either by attraction or repulsion, due to the electromagnetic phenomena resulting from their surrounding mediums. This phenomenon was referred to by Maxwell as an electromagnetic (EM) wave which he found to travel at the speed of light independent of the frequency. The many mathematical equations which Maxwell used to describe this system were later reduced to only four laws which are known today as Maxwell's Equations of electromagnetism.⁴

Maxwell's equations describe the propagation of an electromagnetic field based on the following laws: Gauss's law for electric fields, Gauss's law for magnetism, Faraday's law, and

Ampere's law. Hence, Maxwell's equations can be seen as an interpretation of how the aforementioned laws explain the electromagnetism in succinct manner.⁵

Gauss's law for electric fields indicates an electric charge at any point in space will produce a divergence of the electric flux that is equal to electric charge within the volume of the system (Eq. 1-1).

$$\vec{\nabla} \cdot \vec{D} = \rho_v \quad (1-1)$$

where

$\vec{\nabla} \cdot$ = Divergence Operator

\vec{D} = Electric Flux Density, C/m²

ρ_v = Electric Charge Density, C/m³

also,

$$\vec{D} = \epsilon \vec{E} \quad (1-2)$$

ϵ = permittivity

\vec{E} = Electric Field

It can be inferred from Equation (1-1) that if the charge density within that space is negative, then the electric flux will converge within the system. On the other hand, if the charge density is positive, then the electric flux will flow in an outwards direction from the system. Hence, Gauss's law of electric fields demonstrates that an electric charge can act as a source for an electric field.

Finally, Gauss's law for electric fields is of particular importance for systems comprised of dielectric materials (Eq. 1-2). Consider a system consisting of a dielectric material that has been placed within an electric field (Figure 1-2).⁵ The charges within the system will be polarized thereby inducing an internal electric field different from the external.

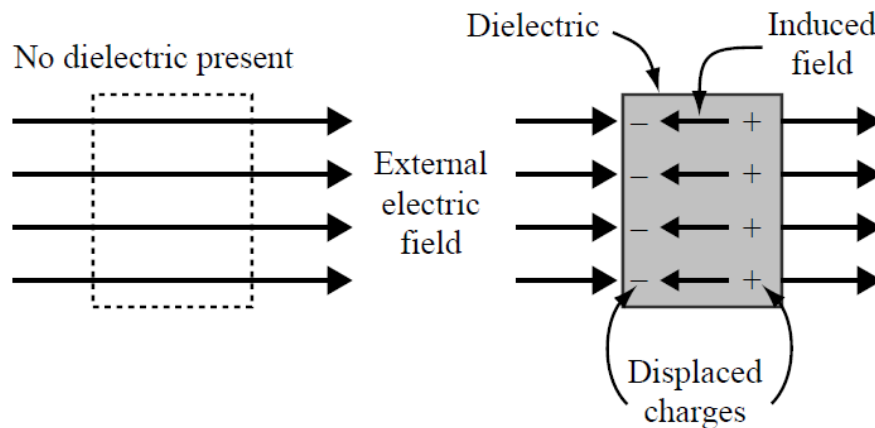


Figure 1-2: Demonstration of Gauss's law of electric fields with a dielectric system. The perturbation of the system by an electric field induces polarization of the internal charges. This regulates the flow of the electric field as it travels through the dielectric material. Schematic taken from Reference [5].

Gauss's law for magnetism (Eq. 1-3) states that the divergence for the magnetic flux at any point in space is zero (0). Considering the schematic of a magnet, it is not possible to separate the north pole from the south pole (Figure 1-3). Furthermore, the outward flux and inward flux of the magnetic fields form a closed loop that are equivalent in opposite directions, hence, the net magnetic flux is zero (0).

$$\vec{\nabla} \cdot \vec{B} = 0 \quad (1-3)$$

where:

\vec{B} = Magnetic Flux Density

also,

$$\vec{B} = \mu H \quad (1-4)$$

where:

μ = permeability

H = Magnetic Field

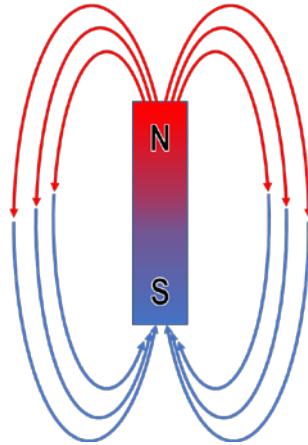


Figure 1-3: Schematic of magnet showing the direction the magnetic flux from the north pole to the south pole consistent with Gauss's Law of Magnetism.

Faraday's law is given by (Eq. 1-5) where it states a circulating electric field is produced by a magnetic flux that changes with time. Unlike charge-based electric fields, induced fields have no origin or terminating points, hence, they have a continuous nature.

$$\vec{\nabla} \times \vec{E} = - \frac{\partial \vec{B}}{\partial t} \quad (1-5)$$

where:

$\vec{\nabla} \times =$ curl operator

Ampere 's Law (Eq. 1-6) indicates that a circulating magnetic field is generated by an electric current combined with a time-varying electric field.

$$\vec{\nabla} \times \vec{H} = \frac{\partial \vec{D}}{\partial t} + \vec{J} \quad (1-6)$$

where:

\vec{J} = Electric Current Density

It is the final two Maxwell's equations discussed (Eq. 1-5 and Eq. 1-6) which begin to show the continuous nature of the EM waves. For instance, a change in the magnetic flux will produce a circling electric field (Eq. 1-5), whereas a change in the electric flux will induce a circling magnetic field (Eq. 1-6) which will induce a change in the electric field and so forth. This process will continue in an oscillatory manner given rise to the propagation of the EM waves (Figure 1-4). After onerous derivations and mathematical transformations of Maxwell's equations (which are well documented elsewhere), the general wave equations for the propagating electric and magnetic waves are given by Equation (1-7) and Equation (1-8) respectively.^{6,7}

$$\nabla^2 \vec{E} = \mu_0 \varepsilon_0 \frac{\partial^2 \vec{E}}{\partial t^2} \quad (1-7)$$

$$\nabla^2 \vec{B} = \mu_0 \varepsilon_0 \frac{\partial^2 \vec{B}}{\partial t^2} \quad (1-8)$$

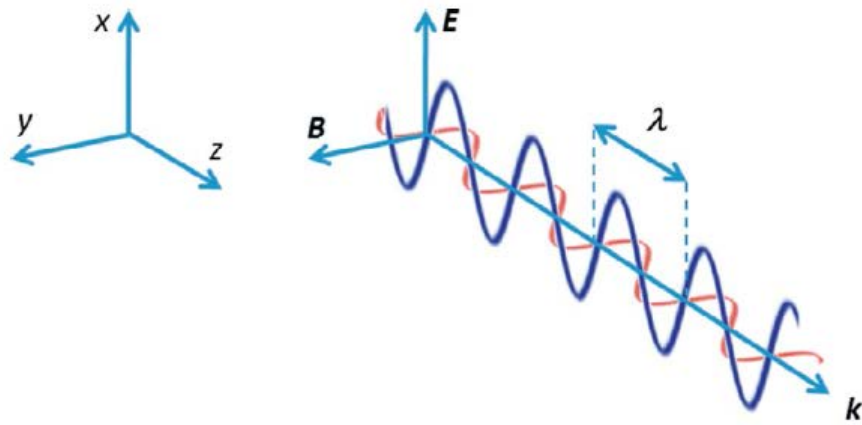


Figure 1-4: Oscillating electromagnetic wave propagating in direction k . Schematic taken from reference [1].

1.1.2 Light as a Particle

Plank and Einstein were pioneers of a new perspective of the nature and structure of light that revolutionized the classical treatment of electromagnetism presented by Maxwell. Plank suggests that light had discrete energy levels with his theory of blackbody radiation.⁸ However it was Einstein, using his experiment of the Photoelectric Effect, that named the discrete particles of light as quanta (photons). He also postulated, as Plank already had done, that these are of quantized energy which could be absorbed and emitted when interacting with atoms.^{9, 10} The energy of a photon is given by:

$$E = h\nu \quad (1-9)$$

where:

h = Plank's constant, 6.626×10^{-34} J·s

ν = Frequency of light

The wavelength (λ) is related to ν by the speed of light in vacuum (c) as described in the following equation:

$$\nu = \frac{c}{\lambda} \quad (1-10)$$

Combining [Eq. 9] and [Eq. 10] gives:

$$E = \frac{hc}{\lambda} \quad (1-11)$$

1.2 Raman

Sir Chandrasekhara Venkata Raman, herein referred to as C.V. Raman, unexpectedly started his studies of light scattering while observing the Mediterranean and Red Seas on his way to a conference at Oxford during 1921.^{11, 12} Using a Nicol prism to suppress the reflection of the sky on the surface water, C.V. Raman postulated that the observed color of the deep blue sea is an effect of the diffraction of light by water molecules. The following years were highly productive for C.V. Raman reaching an innovation apex when reporting in 1928 a new type of radiation, of which we know today as Raman vibrational spectroscopy.¹³

As a general description of Raman, a monochromatic light source is focused through different optical components (i.e. holographic filters, light attenuation lenses) and directed towards a sample (Figure 1-5). The instrumentation used for the initial experiments by C. V. Raman were rudimentary and can be considered a simplified version relative to modern day tooling. Nonetheless, the primary optical components required to effectively harness the inelastic Raman scattering were present (i.e. light source, color filters, telescope, and detector).

It should be noted that C. V. Raman invoked the quantum mechanical treatment of light by suggesting that the incident photon is partially absorbed by the molecule and another portion is scattered as a new quanta with the characteristic molecular frequency.¹³ Despite that there were many questions to be answered referent this new type of radiation, the observations made by C. V. Raman, although bewildering to the scientific community of his time, were not far off in this first publication from what is known today as the Raman effect.

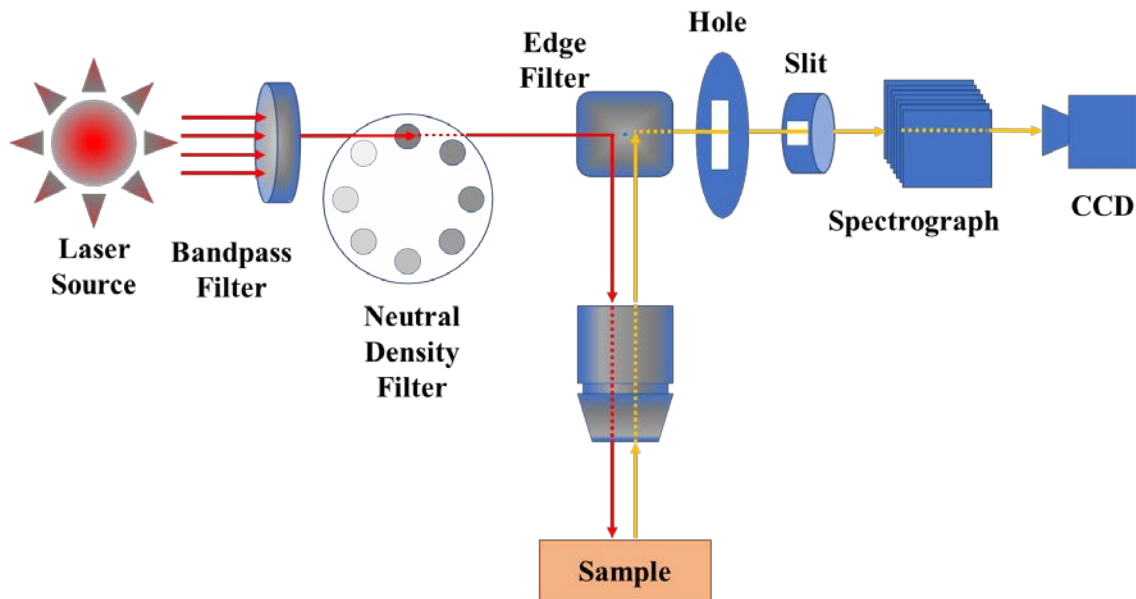


Figure 1-5: Schematic representation of a typical Raman spectrometer. The incident source of energy is represented by the red lines and the scattered energy is shown by the light orange lines. Optical components commonly used are shown such as the bandpass filter (used to clean the incident laser line), the Neutral Density Filter (which attenuates the incident energy), and the Edge Filter (that suppresses the incident wavelength thus allowing for the scattered frequencies to continue towards the spectrograph and detector).

It is well known that molecules existing in their ground state may interact with photons (light) in two manners: (1) the photon is absorbed by the molecule or (2) the photon is scattered. In order for the energy to be absorbed, it must be resonant to the vibrational frequencies of the molecule. In contrast, with scattering, the photon induces a dipole due to a change in polarization of the molecular electron cloud. The energy exchange between the photon and the molecule elevates the latter to a virtual state that does not correspond to any of its quantized energy states. Consequently, the light is scattered either with the same frequency (Rayleigh) or

different frequency (Raman) as the incident radiation (Figure 1-6).^{14, 15} By definition, Raman scattered photons of lower frequency than the incident radiation are known as Stokes bands whereas those with greater frequency are referred to as anti-Stokes.

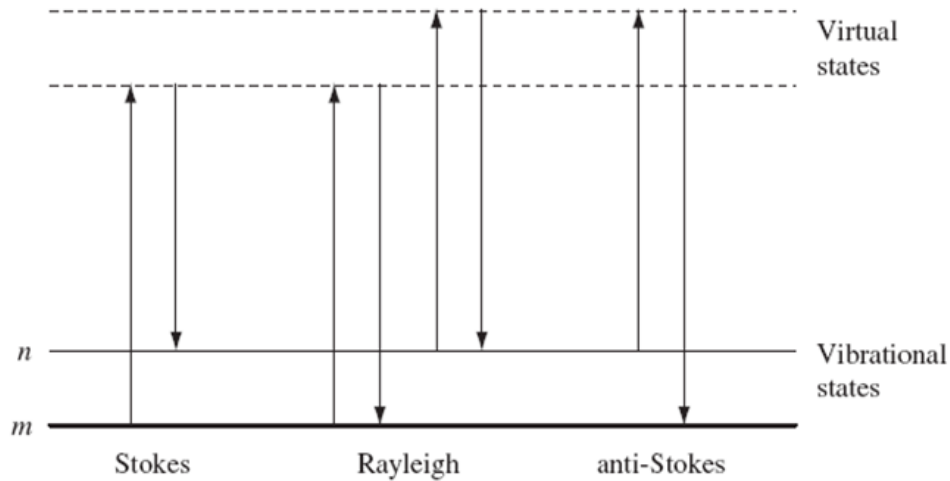


Figure 1-6: Schematic representation of the different scattering processes as proposed by C. V. Raman: Stokes (Raman), Rayleigh, and anti-Stokes (Raman). Schematic from Reference [14].

Considering the energy level schematic (Figure 1-6) and the conservation of energy for a molecule that is interacting with a photon (Eq. 1-12)

$$h\nu + E = h\nu' + E' \quad (1-12)$$

where:

ν = incident photon frequency

ν' = scattered photon frequency

E = incident energy of the molecule

E' = scattered energy of the molecule

then [Eq. 1-12] becomes:

$$\Delta E = h(\nu' - \nu) \quad (1-13)$$

As a result, the following scattering classifications are consistent with Figure 1-6:

Rayleigh (elastic) scattering, $\Delta E = 0$

Stokes (inelastic) scattering, $\Delta E < 0$

Antistokes (inelastic) scattering, $\Delta E > 0$

To best describe the Raman effect, consider placing a molecule within the oscillating electric field of an EM wave as described previously (Section 1.1.1). The EM wave will displace the electron cloud thereby inducing a dipole moment, hence, polarizing the molecule.¹⁵ The polarization of the molecule can be described as follows:

$$\mu = \alpha E \quad (1-14)$$

where:

μ = magnitude of the induced dipole moment

α = polarizability of the molecule

E = electric field strength

The strength of the electric field is given by:

$$E = E_0 \cos(2\pi\nu t) \quad (1-15)$$

where:

E_0 = electric field amplitude

ν = EM wave frequency

Combining Equations (1-14) and (1-15) gives the following:

$$\mu = \alpha E_0 \cos(2\pi\nu t) \quad (1-16)$$

In summary, Equation (1-16) describes the induced dipole moment as the result of the interaction between an EM wave and a molecule that are oscillating at the same frequency. The following equations describe the processes consistent with the elastic and inelastic scattering comprised by the Raman effect.^{14, 15}

The change in bond length is given by $(r - r_{eq})$ where the second term is the bond length at equilibrium (Eq. 1-17). The polarizability at equilibrium is represented by α_0 .

$$\alpha = \alpha_0 + (r - r_{eq}) \frac{\partial \alpha}{\partial r} \quad (1-17)$$

Simple harmonic motion is described in Equation (1-18)] where r_{max} is the maximum separation distance between the bonded atoms and ν_j is the bond vibrational frequency.

$$r - r_{eq} = r_{max} \cos(2\pi\nu_j t) \quad (1-18)$$

Substitution of Equation (1-18) in Equation (1-17) gives the following:

$$\alpha = \alpha_0 + \left(\frac{\partial \alpha}{\partial r}\right) r_{max} \cos(2\pi\nu_j t) \quad (1-19)$$

As a final step, Equation (1-19) is substituted in Equation (1-16), thus giving Equation (1-20) which comprises the elastic and inelastic scattering from molecular vibrations induced by the changes in polarizability due to EM wave.

$$\begin{aligned} \mu = & \alpha_0 E_0 \cos(2\pi\nu_j t) + \\ & \frac{E_0}{2} r_{max} \left(\frac{\partial \alpha}{\partial r} \right) \cos[(2\pi(\nu - \nu_j)t] + \\ & \frac{E_0}{2} r_{max} \left(\frac{\partial \alpha}{\partial r} \right) \cos[(2\pi(\nu + \nu_j)t] \end{aligned} \quad (1-20)$$

The first term of [Eq. 20] represents the Rayleigh scattering occurring at the same excitation frequency (ν) of the EM wave source. The second and third terms correspond to the Stokes ($\nu - \nu_j$) and anti-Stokes ($\nu + \nu_j$) scattering. In summary, one of the most significant attributes of Raman is that scattered photons carry a rich amount of information of the interacted molecules.¹⁵ Identification can be deduced because the displacement of the structural components will render changes in the polarizability of the molecule. Consequently, vibrational frequencies that are intrinsic of the molecular structure (i.e. bond length, bond type) will be detected because of the perturbations induced by the EM wave.

1.3 Surface-Enhanced Raman Scattering (SERS)

Raman scattering is an information rich vibrational spectroscopy technique that has emerged as a promising tool for a diversity of sensing applications. Raman key aspects include (1) it provides structural and mechanistic information of matter, (2) the intensity can be attenuated to be a non-destructive tool to test samples prone to thermal degradation, (3) samples can be in any of its states (i.e. solid, liquid, gas), (4) water is a weak Raman scatterer, hence it can be applied to many industrial green-friendly applications, and (5) there are well-established

spectral correlation tables to render unequivocal identification of samples. Notwithstanding its benefits since its discovery in 1928 by C.V. Raman, the wide implementation of the technique in routine chemical analysis has been limited due to its inherently low cross section that leads to only one out of every 10^7 molecules to exhibit a scattering response.¹³ It was not until the 1970's where the SERS effect was pioneered through independent studies performed by Fleischmann, Jeanmaire, Van Duyne, and Moskovits (Figure 1-7).¹⁶⁻¹⁹ All coincided in observing significant Raman signal enhancements resulting from interactions between adsorbates and a roughened silver surface.

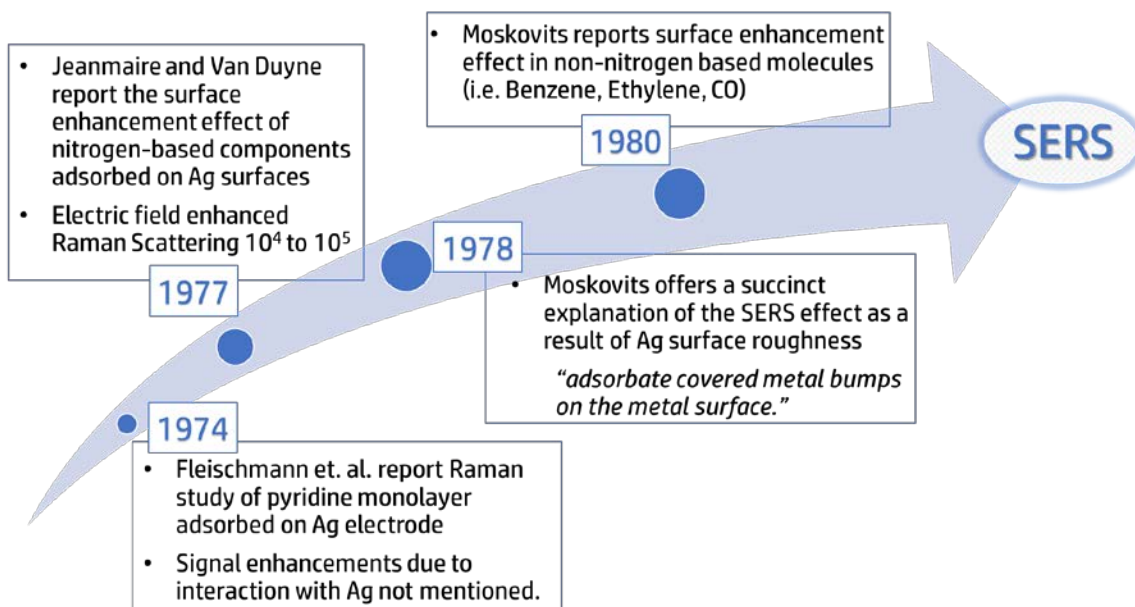


Figure 1-7: Brief chronological summary of the pioneering of Surface-Enhanced Raman Scattering (SERS).

A unified treatment of the SERS phenomena has not been fully elucidated which could be attributed to it being a relatively young mode of spectroscopic analysis.²⁰⁻²⁹ However, there is consensus that the enhancement of the vibrational frequencies for a molecule in the vicinity of a metallized nanoparticle can be attributed to chemical and electromagnetic enhancement mechanisms, of which the latter is attributed the major contributor.

1.3.1 Chemical Enhancement (CE)

The SERS chemical enhancement (CE) is hypothesized to consist of different mechanisms that are triggered by the chemisorption of the analyte (referred to as a sorbate for the context of this discussion) to the surface active sites of the metal.^{21, 27, 30-32} One such is a resonant charge transfer (CT), a photoinduced mechanism occurring when the excitation source frequency is resonant to the metal-adsorbate interfacial electronic transitions (Figure 1-8).³³ The resonant CT is considered to work in conjunction with the EM since it amplifies the SERS signal based on a temporary induced state (as in the case of a plasmon).^{24, 32}

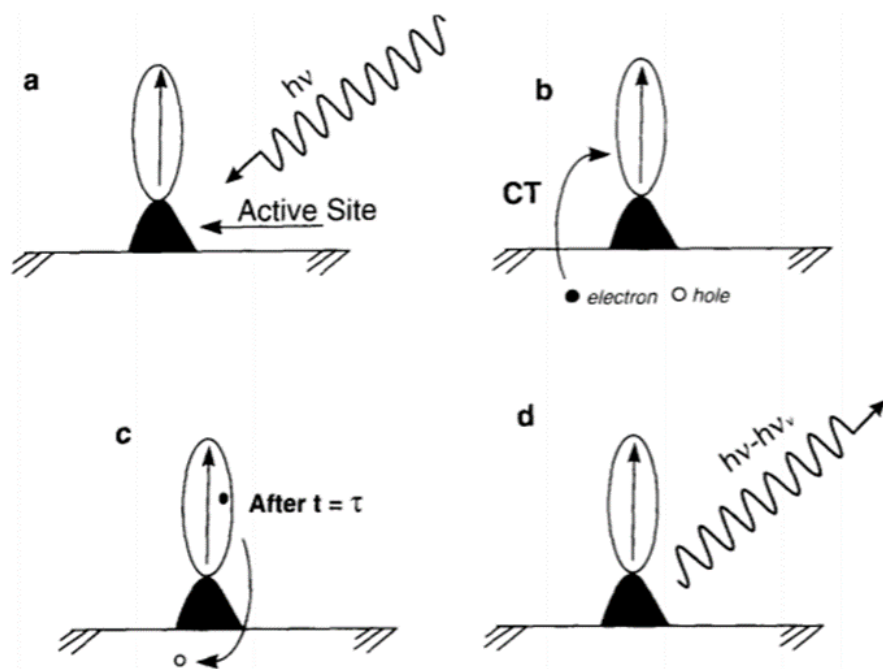


Figure 1-8: Chemical Enhancement mechanism in which (a) the resonant charge transfer is initiated by a photon creating an electron-hole pair; (b) the electron is transferred from the metal to the adsorbate; (c) relaxation of the excited molecule transfers returns an electron with adsorbate intrinsic information to the metal; and (d) electron recombines with the hole in the metal releasing a photon which carries vibrational frequencies of the adsorbate. Schematic taken from Reference [33].

Two additional CE mechanisms places the HOMO and LUMO of the adsorbate and the metal within the Fermi level of the latter (Figure 1-9).^{24, 34, 35} An electron is transferred from the metal's HOMO to the adsorbates LUMO or from the adsorbates LUMO to the metal's HOMO.

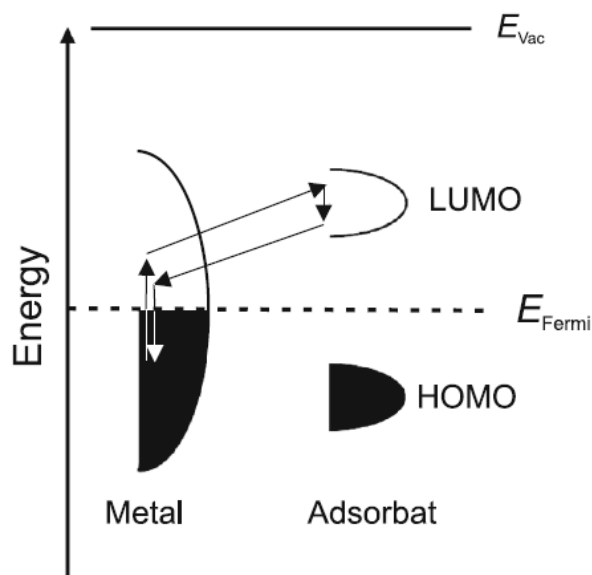


Figure 1-9: Schematic of chemical enhancement via electron transfer at the Fermi level. Schematic taken from Reference [24].

Despite that the principles behind CE are yet to be fully elucidated, the enhancements generally reported are from 10 to 100.^{32, 36} Careful development of electronic orbitals of the participating molecules and onerous calculations are required in order to demonstrate (to some extent of clarity) both CE mechanisms. This results in complex theoretical mathematical modeling which is considered at times (with no means of subtracting any intellectual merit) not fulfilling for an improvement that is surpassed by at least 10^4 with plasmonic mechanisms.

1.3.2 Electromagnetic Enhancement (EM)

Enhancement factors from 10^7 to 10^{10} have been attributed to the electromagnetic (EM) enhancement.^{20, 32} This effect is the result of a nanoscale field confinement known as surface plasmons which are generated by the collective oscillation of free electrons on the roughened

metal surface. Any molecules that are in the vicinity of the near field enhancement produced by the EM wave will undergo a Raman signal amplification. Spectral bands will be rendered of the molecule in reference to the substrate surface.

It should be noted that EM enhancements differ from CE mainly that the latter require direct adsorption of the analyte to the metal surface, whereas the first needs only for the molecule of interest to be in the vicinity of the near field enhancement generated. A limitation of the EM enhancement pertains to the spatial offset of the molecule from the generated plasmon. This means that the further the molecule is from the induced electric field on the metalized surface, the weaker the Raman signal is expected to be.

Surface plasmons are a collective oscillation of free metal electrons that have coupled to the EM wave with a preference to surface cavities (Figure 1-10).³⁷ Surface plasmons can either be a surface plasmon polariton (SPP) or a localized surface plasmon resonance (LSPR) which generally is referred to as a *hot spot*.

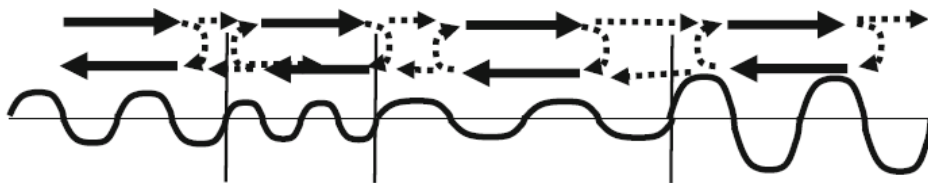


Figure 1-10: Schematic of strong localization of surface plasmon in surface cavities. Schematic taken from Reference [37].

In the case of the first, SPPs can be viewed as the propagation of the plasmon across the metal-dielectric interface. On the other hand, a LSPR is the confinement of the EM wave to a stationary point that is defined by a discontinuity on substrate surface (i.e. a grating, indentations, roughness). LSPRs are generated at closed geometrical boundaries where the EM wave is

concentrated. The surface charge density is significantly increased at this point thus amplifying the Raman response of molecules in the vicinity. Schematic representations of SPP and LSPR are given in Figure 1-11.

Optimization of SERS substrates in general are focused in (1) tailoring the geometric properties of the substrate surface in order to obtain stronger LSPRs and (2) increasing the number of available hot spots for surface interactions with analytes. Subsequent chapters will provide a more detailed description of the optimization of SERS substrates and corresponding figures of merits (i.e. Enhancement Factors).

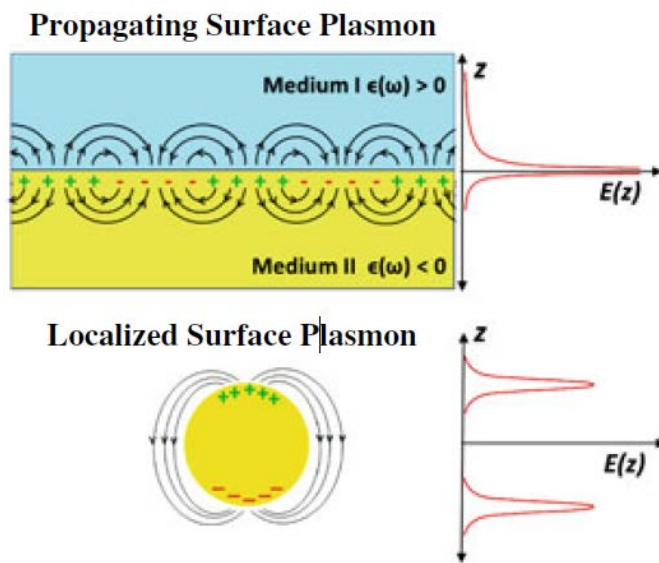


Figure 1-11: Schematic representation of (a) SPP propagation across a substrate and (b) the induced EM field confined by the particle geometry thereby generating a LSPR. Schematic taken from reference [37].

1.3.3 Enhancement Factor

The enhancement factor (EF) is the figure of merit generally used to assess the performance of a SERS substrate. There are various iterations to this formula, yet the most common version is presented for this section is:

$$EF = \frac{N_{\text{vol}} I_{\text{surf}}}{N_{\text{surf}} I_{\text{vol}}} \quad (1-21)$$

where:

N_{vol} = Average number of molecules per scattering volume

N_{surf} = Average number of molecules adsorbed on the substrate surface

I_{surf} = SERS response of molecules

I_{vol} = normal Raman response of molecules

It should be noted that the EF will contemplate all Raman signal enhancement mechanisms present in the adsorbate – substrate system. Careful consideration must be given to the type of Raman probe that is used for assessment of the SERS performance since there are analytes that may exhibit a combination of CE, EM, and other enhancement phenomena (i.e. resonance enhancement). Hence, this could make a huge difference at the moment of classifying SERS substrates by performance. For instance, benzenethiol is an analyte generally used to assess the plasmonic performance of a SERS platform since the enhancement exhibited pertains mostly to EM contributions. A more thorough discussion of different Raman probes used for determination of enhancement factors is provided in Chapter 4.

1.4 Finite-Difference Time-Domain (FDTD)

The interaction of an electromagnetic field with nanostructures can be described using Maxwell's equations. Unfortunately, this is accompanied with onerous mathematical complexities which are time consuming and generally require assumptions for simplification purposes. An algorithm known as Finite-Difference Time-Domain (FDTD) was developed in order to solve Maxwell's equations without the use of assumption-based simplifications.³⁸⁻⁴⁰ FDTD emulates the propagation of light by dividing the media into a cubic lattice where each unit cell is known as a Yee cell (Figure 1-12).³⁹ The set of Maxwell's curl equations for every individual Yee cell is progressively solved in a finite-difference manner until the iteration has been satisfied.

Commercial FDTD platforms are available for solving Maxwell's equation of EM wave propagation on complex substrate geometries. The studies that will be discussed further on used the Lumerical® FDTD Solutions software package which articulates the FDTD algorithm to model the propagation of light based on the interactions of the EM wave with the physical properties (e.g. dimensions, material dielectrics) of the target substrate.⁴¹ The projected spatial distribution of the plasmonic field enhancements is associated to the energy scattering by the nanostructured particles. Consequently, the performance of a SERS substrate can be predicted and LSPRs optimized without the need for physical testing.

FDTD uses an algorithm reported by Kane S. Yee in 1966 with the aim of solving Maxwell's Equations for the scattering of an electromagnetic pulse by a cylinder.³⁹ First, devices or material that will interact with the EM wave are divided into spatial grids in which the

electric field ($\vec{E}_{x,y,z}$) is surrounded by four magnetic vector components ($\vec{H}_{x,y,z}$), and every magnetic component is surrounded by four electric fields (Figure 1-12). The results are an intertwining of the differential form of Faraday's Law (Equation 1-5) and Ampere's Law (1-6). In fact, it should be noted that FDTD does not use the wave equations derived by Maxwell's Equations (described in Section 1.1.1).

The spatial grid is the unit cell for the simulation mesh and is recommended to be less than $\lambda/10$ in order to improve the numerical accuracy.⁴² Sub-gridding can also be used to reduce calculation errors in areas of high geometrical complexities or of great interest for near field enhancements.

Physical properties of the materials that may affect the EM propagation are critical for the modelling. For instance, the permittivity (ϵ) and permeability (μ) are contemplated as these form part of the electric field divergence and magnetic field curl. Simulation boundary conditions are of great importance since the right condition can effectively inhibit spurious reflections that occur at the edge of the problem space from re-entering the simulation region.⁴³

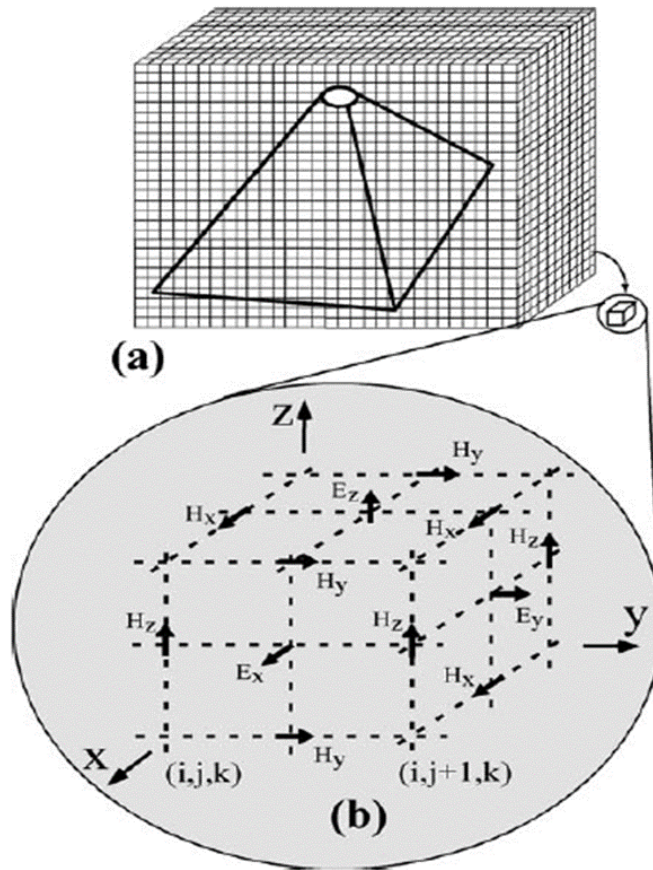


Figure 1-12: General schematic to solve for Maxwell's equations using a Yee cell.³⁹ (a) A three-dimensional problem space divided into many cubic cells. (b) A single unit cell depicting the location of the electric fields ($E_{x,y,z}$) and magnetic fields ($H_{x,y,z}$).

2 FDTD PLASMONIC SIMULATIONS OF HYBRID MORPHOLOGY NANOARRAYS

Chapter 2 is an adaptation of a research article published in Applied Spectroscopy by Jenifier Olavarria-Fullerton, Raymond A. Velez, Sabrina Wells, Michael J. Sepaniak, Samuel P. Hernandez-Rivera, and Marco A. DeJesus:

J. Olavarría-Fullerton, R. A. Velez, S. Wells, M. J. Sepaniak, S. P. Hernández-Rivera, M. A. D. Jesús. **Design and Characterization of Hybrid Morphology Nanoarrays as Plasmonic Raman Probes for Antimicrobial Detection.** Appl. Spectrosc. 2013. 67(11): 1315-1322. doi: 10.1366/13-07001.

The use of "we" in this chapter refers to the authors in the aforementioned citation, including myself. My primary contributions to this article included: (A) Design and Optimization of the FDTD Simulation Protocols, (B) Collection and processing of FDTD Simulations, (C) Data analysis of the FDTD data, (D) Collection and interpretation of the cited literature pertaining to FDTD, and (E) Complete writing of the FDTD section.

2.1 Introduction

Plasmonic nanoarrays of hybrid morphology for detection of organoarsenic antimicrobial veterinary drugs in aqueous systems were fabricated using advanced micromachining methods.⁴⁴ The SERS sensing platform consisted of alternating Ag/SiO₂/Si nanoarrays of hexagonal and elliptical features (Figure 2-1). Variations of geometrical properties were studied (i.e. interparticle spacing, nanoarray orientation referent polarization vector) and rendered an optimized morphology corresponding to a parallel-oriented array with a 200 nm interparticle gap.

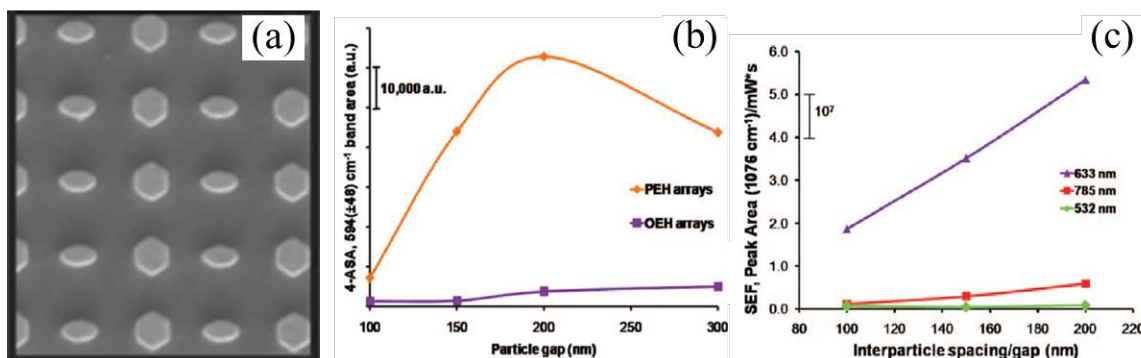


Figure 2-1: Hybrid morphology nanoarrays used for plasmonic sensing applications.

A key aspect of the study was the versatility of the hybrid morphology nanoarray for three different laser excitation sources: 532 nm, 633 nm, and 785 nm. The calculated EF were within 5, 6 and 7 orders of magnitude respectively. However, it was unclear how the different features contributed to the overall SERS response. Moreover, a non-hybrid system using the

individual features was not fabricated, hence, there was no means of assessing the advantages of using a hybrid system.

FDTD modelling was used to study the plasmonic response of three nanoarray systems: hexagon, ellipse, and hybrid morphology.

2.2 FDTD Modelling Parameters

The Lumerical[®] FDTD Solutions software articulates Finite-Difference Time-Domain (FDTD) to effectively solve Maxwell's equations required to model the electromagnetic fields (EMF) induced by the propagation of light across the substrate based on its physical properties (i.e. dimensions, material dielectrics).⁴¹ A simple 3D model of a unit cell for hybrid nanoarray consisting of a hexagon and an ellipse arranged in a parallel form (PEH) was comprised within a 2 nm² mesh simulation region (Figure 2-2). Boundary conditions consisted of (1) periodic along xy axis and (2) perfectly-matched layers (PML) at the z axis. A plane-wave source (5 nm from top of Ag layer surface and parallel to the transversal axis to the nanoarray) was used to emulate an incident laser ($\lambda = 500$ nm to 850 nm) with various monitors strategically placed to obtain EMF data. Two additional systems consisting of either ellipses or hexagons were modeled besides the fabricated PEH substrate using the aforementioned conditions. A schematic of the structural components and nanoarray layout is provided in (Figure 2-3).

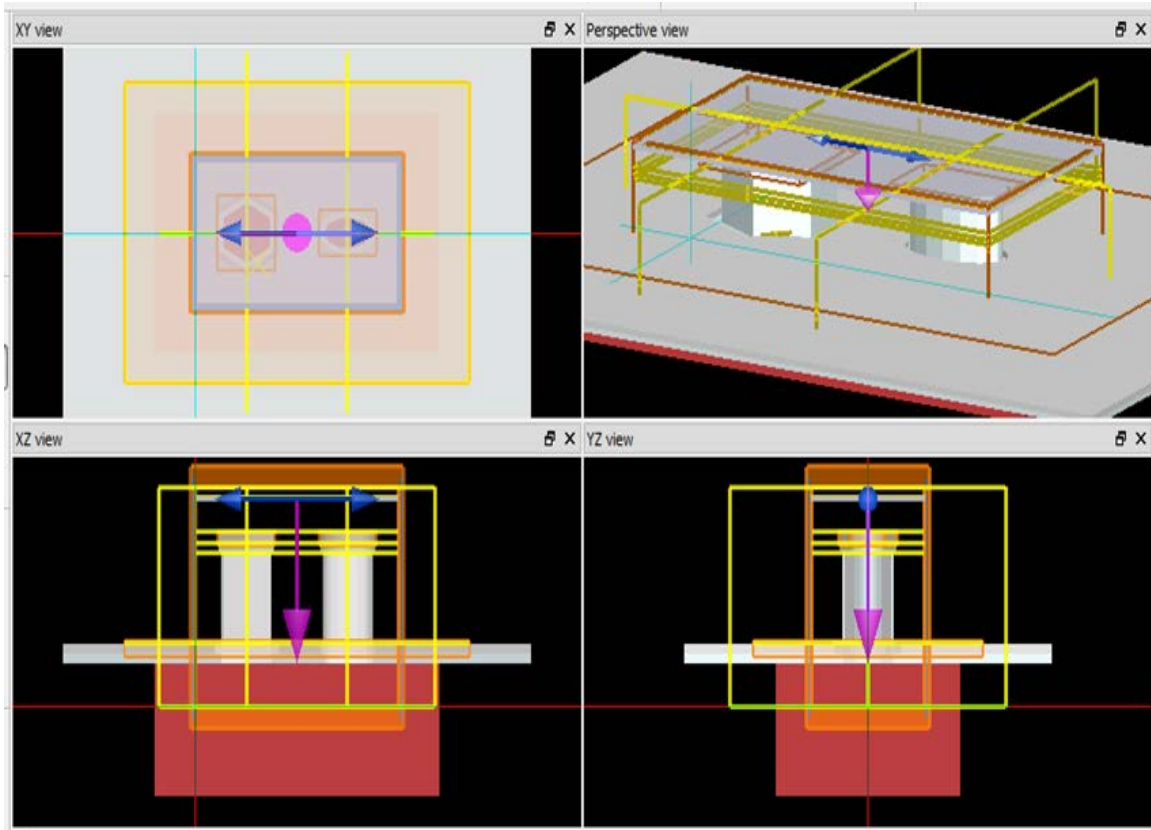


Figure 2-2: Lumerical® FDTD platform depicting the hybrid morphology nanoarray and simulation components: monitors (yellow), simulation mesh regions (orange), and source (blue/violet arrows).

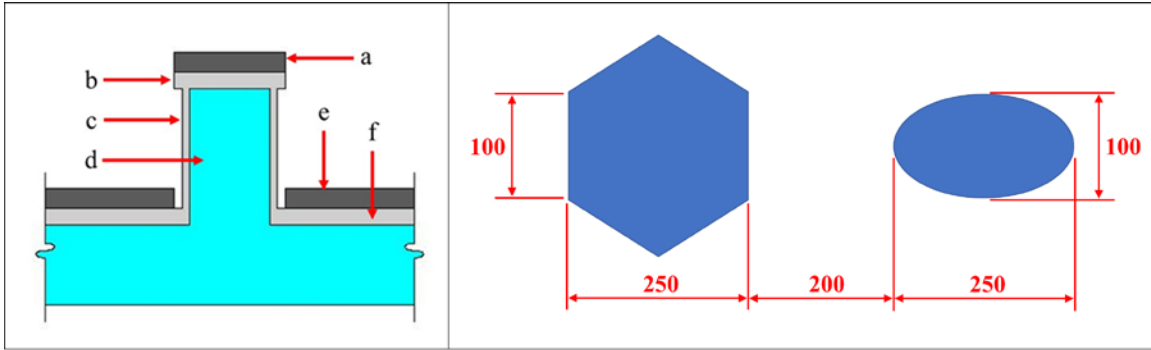


Figure 2-3: (Left): Schematic cross section of PEH nanoarray structural components used FDTD modelling. The following dimensions correspond to t = thickness, h = height: (a) Ag disk, $h = 25$ nm; (b) SiO₂ on pillar top, $h = 20$ nm; (c) SiO₂ on sidewalls, $h = 250$ nm, $t = 20$ nm; (d) Si pillar, $h = 250$ nm, (e) Ag mirror, $h = 25$ nm; (f) SiO₂ on etched wafer surface, $h = 20$ nm. (Right) Schematic of hybrid nanoarray layout with a 200 nm gap in the point closest between both features. All dimensions are given in nm. The same setup is used for the single feature system.

2.3 FDTD Modelling Projections

The near-field enhancements for the PEH hybrid array was plotted against the wavelength (Figure 2-4). The $|E/E_0|^2$ response for the hexagon depicts a well-defined band with a maxima at $\lambda = 543$ nm and two unresolved bands at 634 nm and 734 nm for the hexagon. The ellipse shows one strong band at 536 nm with a maximum intensity of 1341 a.u. The signal decreased to about 200 a.u. at 625 nm and remained consistent until 800 nm where the intensity is reduced significantly. The FDTD data predicts a suitable response for target Raman lasers with wavelengths of 632.81 nm and 785 nm mostly in part because of the hexagon feature. The PEH nanoarray is expected to render the strongest response for a 532 nm excitation source because of the ellipse feature.

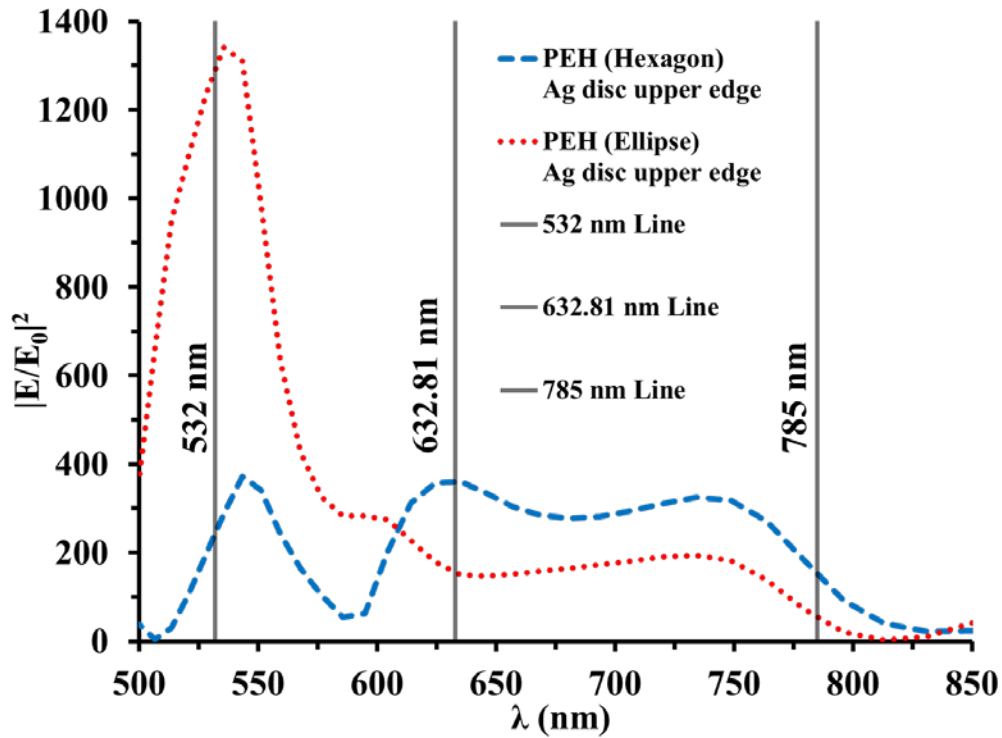


Figure 2-4: FDTD data depicting $|E/E_0|^2$ as a function of wavelength for the hybrid nanoarray consisting of hexagons and ellipses. Gray vertical lines indicate target excitation wavelengths.

The simulated electric field of the nanoarrays consisting of either hexagons or ellipses was obtained to better understand the benefits of having a hybrid system (Figure 2-5). The hexagon substrate depicted three bands as in the PEH, but with slight differences in the wavelength of the maxima. For instance, a blue shift is observed for the band at 542 nm to 551 nm with a 64% decrease in the electric field for the hexagon substrate when compared the PEH. The second band is shifted from 634 nm to 604 nm for the single hexagon feature that is not coupled to the ellipse. This is accompanied by a 40% signal decrease when not in the hybrid system. Individual hexagon arrays had significantly greater electric fields for the 780 nm region than in the PEH hybrid system.

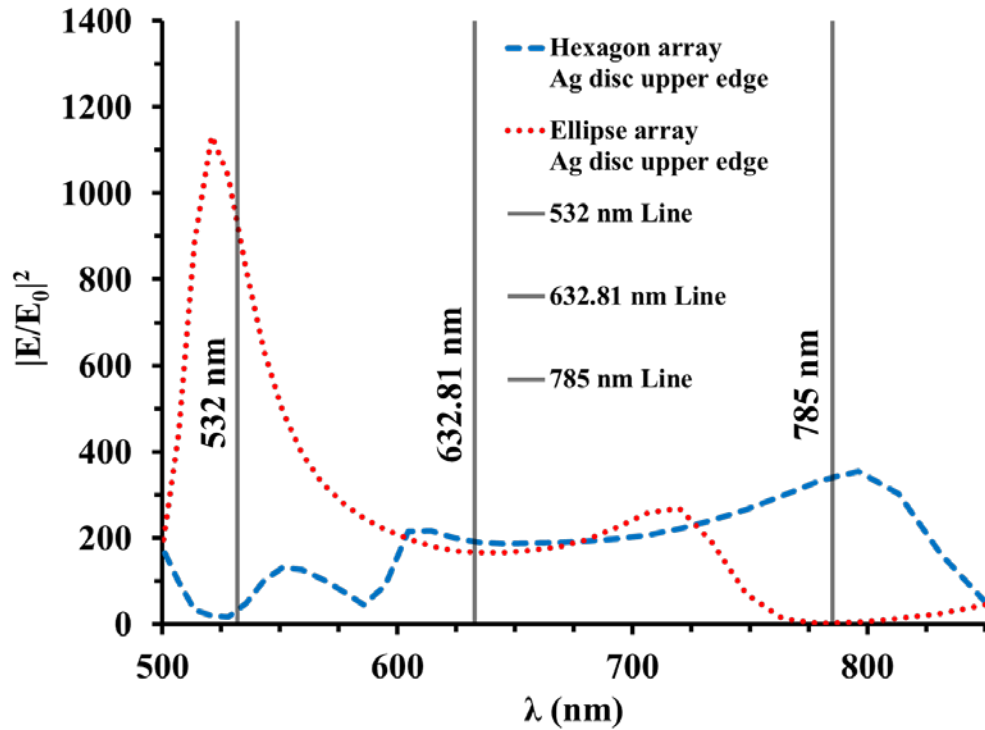
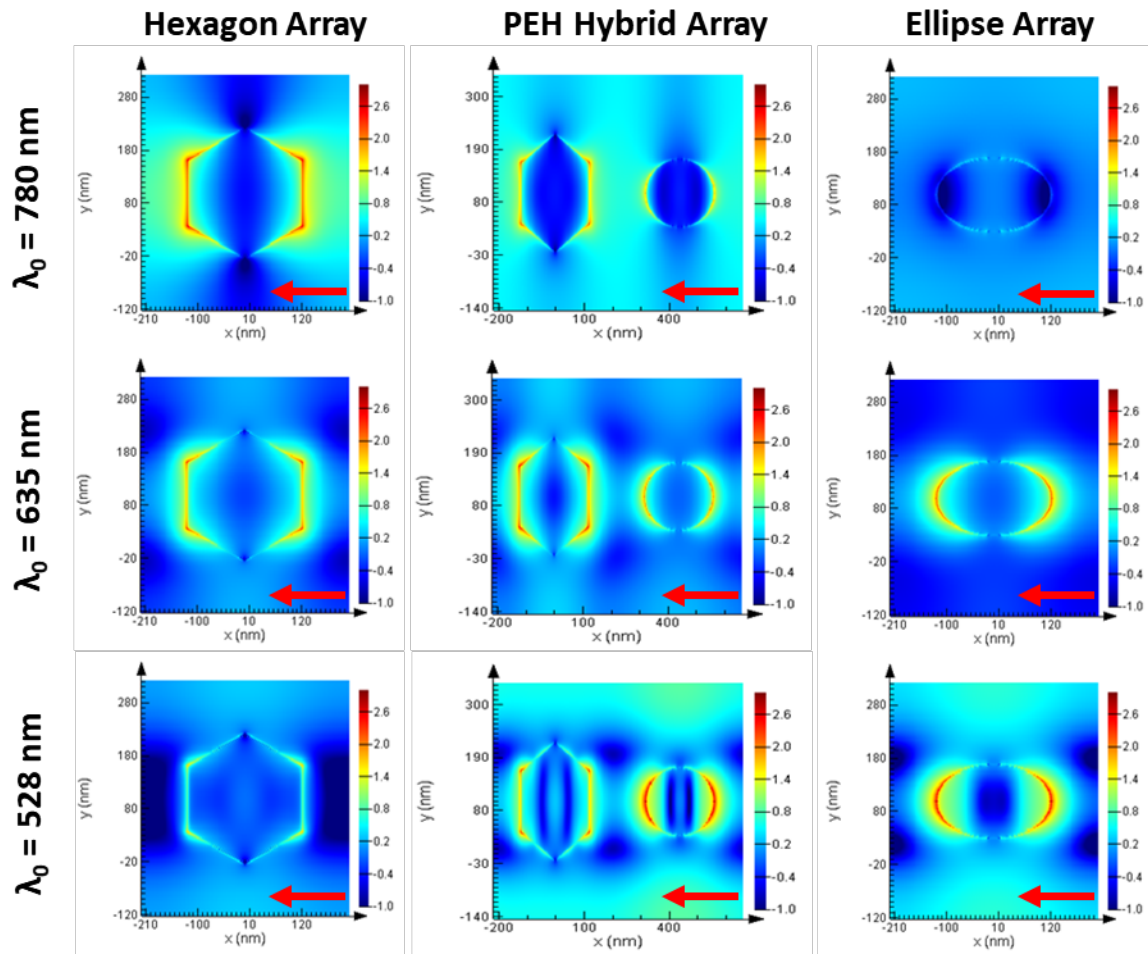


Figure 2-5: FDTD data depicting $|E/E_0|^2$ as a function of wavelength for the nanoarrays consisting of either hexagons or ellipses. Gray vertical lines indicate target excitation wavelengths for SERS applications.

Improvement in the ellipse plasmonic signal is also observed when located in the PEH system in contrast to the single feature (Figure 2-5). The ellipse substrate shows a band maximum of 1134 a.u. at 521 nm which undergoes a red shift to 536 nm, with an 18% signal increase when located in the PEH array. The most significant enhancement was the signal increase observed at 780 nm from 0.9 a.u. in the ellipse substrate to 71 a.u. when in the PEH system. This was accompanied with a redshift of the 720 nm band maxima in the ellipse substrate to 750 nm in the PEH. This suggests a coupling occurs between the hexagon and the ellipse features when placed in the hybrid system.

The $|E/E_0|^2$ distribution at different FDTD excitation sources (528 nm, 635 nm, and 780 nm) allow a clearer appreciation of how the plasmon resonance propagates across the substrates comprised of PEH hybrid arrays and individual morphologies. The near field distribution seen from xy plane (Figure 2-6) and the xz plane (Figure 2-7) are aligned with polarization vector of the EM source. The wavelengths used to generate the near field enhancement graphics are not exactly the same to those used for the physical experiments (532 nm, 632.81 nm, and 785 nm) because the data points were displaced due to resolution effects. However, we do not foresee any significant deviations between the actual Raman data and the trends observed by the modelling due to the proximities between the theoretical and experimental incident wavelengths.

The modelling at the xy plane shows a strong near field enhancement around the upper Ag edges of the feature arrays, except at 528 nm and 780 nm for the hexagon and ellipse respectively (Figure 2-6). The most intense regions of $|E/E_0|^2$ distribution occur parallel to the polarization vector for all array systems. In the PEH hybrid, there is an apparent coupling between the features which effectively propagates the resonance plasmon across hexagons and ellipses at the three wavelengths screened. This characterizes the PEH hybrid nanoarrays as a multiwavelength SERS platform that overcame the limitations confronted with single morphology nanoarrays.



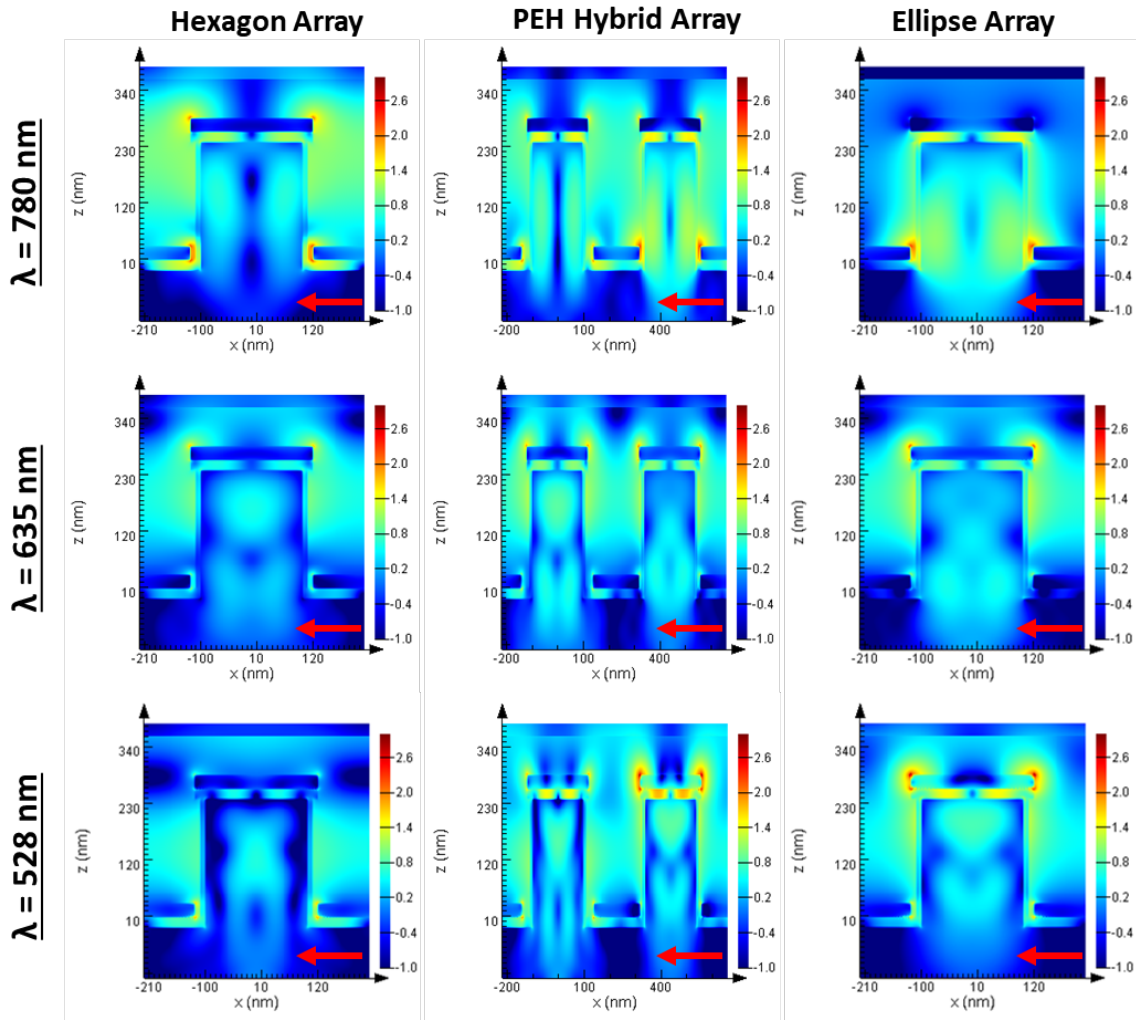


Figure 2-7: FDTD $|E/E_0|^2$ distribution at the xz plane for the simulated array systems: Hexagon (left), PEH Hybrid morphology (middle), and Ellipse (right). The resonance plasmons were induced using excitation sources: 780 nm (top row), 635 nm (middle row), and 528 nm (bottom row). The source polarization vector is indicated by the red arrow.

The graphics for the xz plane (Figure 2-7) allows for a better assessment of the coupling between the hexagon and the ellipse when in the PEH hybrid array. It is well established in this study that the ellipse and hexagon will not resonate at 780 nm and 528 nm respectively when placed in separate platforms. However, with the xz plane, it is noticed that what is actually occurring is that the electric field is propagating perpendicular to the polarization vector in the

case of the ellipse at 780 nm. The hexagon is only resonating poorly at the Ag mirror edge (at the bottom of the pillar). Integrating both features allowed for an effective coupling and a propagation parallel to the polarization vector. It is very probable that adjusting the current dimensions of both geometries would tune the plasmonic properties so as to confine the LSPR in the regions where analyte-surface interactions are most probable (the top Ag surface). A score card with a qualitative perception of the plasmonic performance provides a succinct picture of the ability to render a plasmonic signal most susceptible for the analyte adsorption (Table 2-1).

Table 2-1: Score card for $|E/E_0|^2$ per morphology feature and excitation source.

| Raman Laser (λ_0) | 528 nm | 635 nm | 780 nm |
|---|-------------------|-------------------|-----------------|
| Ellipse | Very Strong | Strong | Poor |
| Hexagon | Very Poor | Strong | Very Strong |
| PEH | Moderate / Strong | Moderate / Strong | Poor / Moderate |

The FDTD predictions of the PEH system were compared to SERS experimental data acquired to confirm the validity of model (Table 2-2).⁴⁴ The modelling projections are in the row “PEH_{FDTD}” of Table 2-2. The SERS enhancement factor (SEF) was calculated using the C-S stretching mode of 4-aminobenzoic acid (4-ABT) at 1078 cm⁻¹.

The modelling projections suggest that excitation sources of 532 nm and 633 nm will render stronger responses at the Ag disc region whereas a poor to moderate response is expected for a 785 nm. The SERS data shows the strongest responses for 4-ABT using the 532 nm and

633 nm excitation sources. Consistent with FDTD simulations, the 785 nm laser rendered a response one magnitude order below than the other two employed wavelengths. This substantiates that the PEH system produces a greater signal response for shorter wavelengths (520 nm, 532 nm) than for the longer wavelengths (780 nm, 785 nm). It should be noted that there is a lack of correlation between the SERS response and the reported SEF. It should be noted that a more thorough discussion pertaining to EFs and analytical performance is provided in Chapter 4.

Table 2-2: Contrast between FDTD Modelling projections and SERS Data⁴⁴

| Raman Laser (λ_0) | 532 nm | 633 nm | 785 nm |
|--|--------------------|--------------------|--------------------|
| Modelling Projection for PEH_{FDTD} | Strong / Moderate | Strong / Moderate | Poor / Moderate |
| SERS Data for Area $1078 \text{ cm}^{-1}(\nu_{C-S})$ | 1.48×10^4 | 4.69×10^3 | 8.01×10^3 |
| SEF_{4-ABT} | 8.61×10^5 | 5.35×10^7 | 5.90×10^6 |

3 FDTD MODELLING FOR OPTIMIZATION OF DISC-ON-PILLAR (DOP) PLASMONIC ARRAYS

Chapter 3 is an adaptation of a research article (accepted on 03/27/2019 and first published online on 04/16/2019) in Applied Spectroscopy by Raymond A. Velez, Nickolay V. Lavrik, Ivan I. Kravchenko, Michael J. Sepaniak, and Marco A. DeJesus:

R. A. Velez, N. V. Lavrik, I. I. Kravchenko, M. J. Sepaniak, M. A. D. Jesus. **Surface-Enhanced Raman Scattering (SERS) Studies of Disc-On-Pillar (DOP) Arrays: Contrasting Enhancement Factor with Analytical Performance.** Appl. Spectrosc. 2019. ##(##): ##### - #####. doi: 10.1177/0003702819846503.

The use of "we" in this chapter refers to the co-authors and me in the aforementioned citation. My primary contributions to this article included: (A) Design and Optimization of the FDTD Simulation Protocols, (B) Collection and processing of FDTD Simulations, (C) Data analysis of the FDTD data, (D) Collection and interpretation of the cited literature pertaining to FDTD, (E) Fabrication of the Nanostructures, (F) Development and optimization of the Raman testing protocols, (G) Acquisition and processing of all SERS data, (H) Data analysis and interpretation of SERS data, (I) Collection and interpretation of most of the cited literature, and (J) Most of the writing.

Chapter 3 will focus on the modelling projections for the Disc-On-Pillar plasmonic arrays which pertain to contribution items (A) to (D).

3.1 Introduction

The importance of using FDTD modelling to bridge the gap between theoretical and experimental data was presented in Chapter 2. Consistent with a lean approach, FDTD is a productivity tool that ascertains the optimum combination of plasmonic and geometric properties prior to investing in the nanofabrication processes.

This chapter presents the optimization of a Disc-On-Pillar (DOP) array designed for studying analytical performance and enhancement factors. Our goal here was to investigate how periodicity affects SERS performance of DOP arrays prior to the fabrication of the substrate using the Lumerical[®] FDTD Solutions software package. A number of geometrical and structural parameters, including pitch, pillar height and pillar diameter, are critically important for tuning the resonance in DOP arrays to the excitation wavelength of the Raman spectrometer.

3.2 FDTD Modelling and Projections

A number of geometrical and structural parameters, including pitch, pillar height and pillar diameter, are critically important for tuning the resonance in DOP arrays to the excitation wavelength of the Raman spectrometer. Our goal here was to investigate how periodicity affects SERS performance of DOP arrays prior to the fabrication of the substrate using the Lumerical[®] FDTD Solutions software package.

The electromagnetic field (EMF) was simulated in the vicinity of a DOP array comprised of a 25 nm thick Ag disc on a SiO₂/Si pillar with a final diameter and height of 120 nm and 175 nm respectively (Figure 3-1).

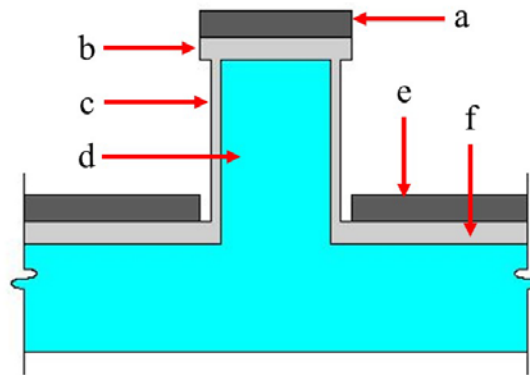


Figure 3-1: Schematic of DOP structural components used FDTD modelling. The following dimensions correspond to d = diameter, h = height, i.d. = inner diameter, and o.d. = outer diameter: (a) Ag disk, h = 25 nm, d = 120 nm; (b) SiO₂ on pillar top, h = 20 nm, d = 120 nm; (c) SiO₂ on pillar sidewalls, h = 155 nm, d = 155 nm, i.d./o.d. = 80 nm / 100 nm; (d) Si pillar, h = 175 nm, d = 80 nm; (e) Ag mirror, h = 25 nm, i.d. / o.d. = 120 nm / 4000 nm; (f) SiO₂ on etched wafer surface, h = 20 nm, d = 1000 nm.

A simplified 3D model included a linearly polarized plane-wave source impinging on the substrate from top at normal incidence to emulate an incident laser ($\lambda = 500 \text{ nm}$ to 850 nm). Several monitors were placed in X-Y, X-Z and Y-Z planes to obtain electric field enhancement data (Figure 3-2a). A conformal 2 nm refined mesh was used for the regions occupied by the Ag disc and mirror. Boundary conditions for DOP arrays consisted of (1) periodic boundary conditions along x and y axis and (2) perfectly-matched layers (PML) along the z axis. The in-plane dimensions of the 3D model combined with periodic boundary conditions were selected to emulate periodicity of the experimental DOP arrays. The mesh settings for modeling a single

DOP were the same as the arrays. Contrast to periodic arrays, the boundary conditions for an individual pillar were set to PML on all sides and a Gaussian source was used instead of a plane wave. The simulated DOP design was based on increasing the interpillar distance from 20 nm to 600 nm using the following pitches (nm): 140, 160, 180, 200, 220, 240, 370, 470, 570, 670, and 720.

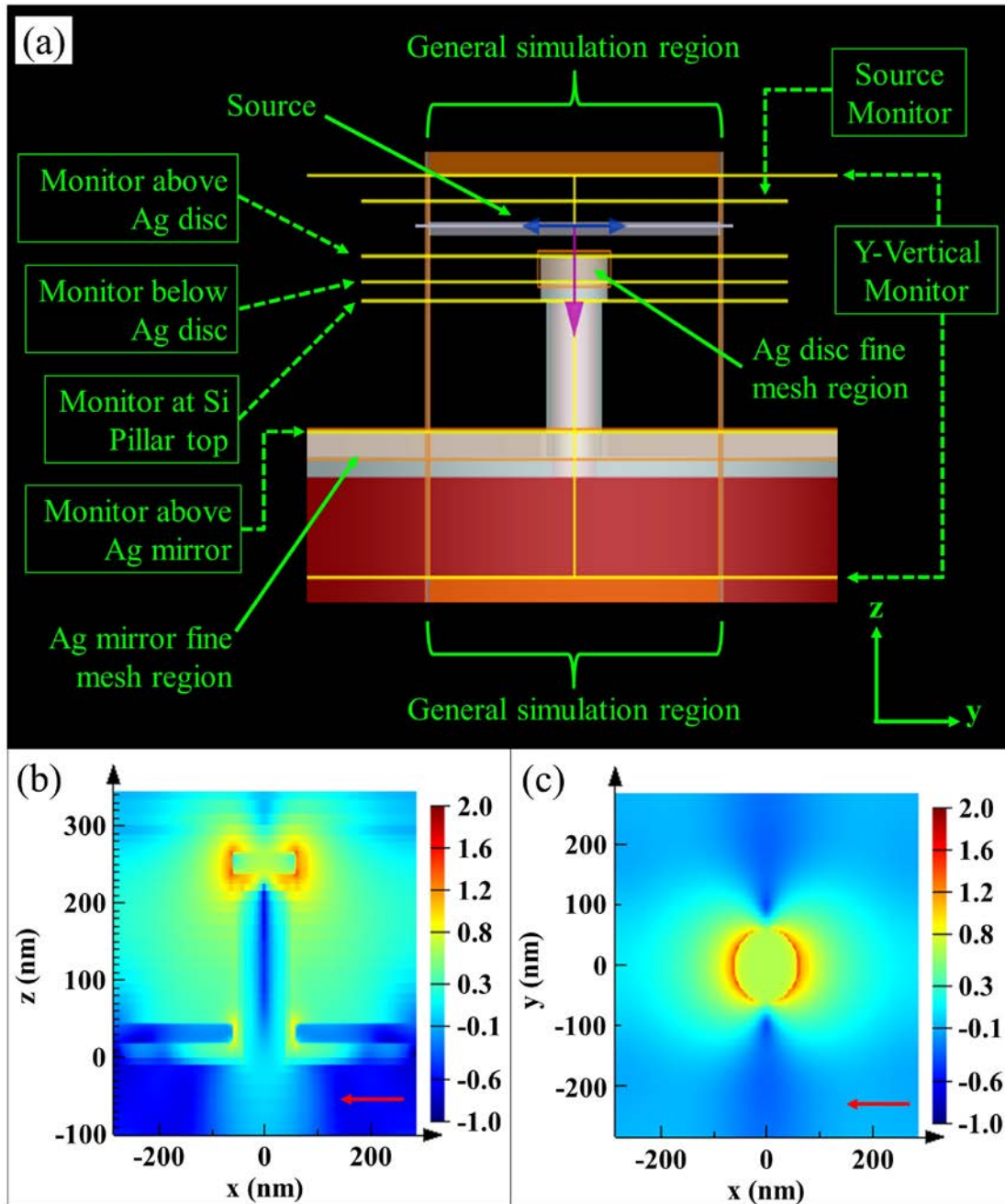


Figure 3-2: (a) Schematic of the DOP structure with simulation components used for FDTD modelling. The yellow lines represent the location of the different monitors used. Simulation mesh areas are defined by orange boxes. (b) Near-field intensity color maps (log₁₀ scale) as rendered by the X-Z monitor for DOP arrays with a 570 nm pitch at 630 nm incident wavelength. (c) Near-field intensity color maps (log₁₀ scale) produced by the X-Y monitor for DOP arrays with a 570 nm pitch at 630 nm incident wavelength. The red arrows in (b) and (c) indicate the direction of the polarization vector.

The interaction of the incident EMF with periodic DOP arrays generated local electric field enhancements, $|E/E_0|^2_{\max}$, where the strongest response was observed to be around the edge of the Ag disc (Figure 3-2b and Figure 3-2c). This is consistent with the previous observations and suggests strong LSPRs at sites accessible for interactions between the Ag surface and analytes of interest.⁴⁵ The electromagnetic field intensity was analyzed for excitation wavelengths in the range of 500 nm to 850 nm with 10 nm increments.

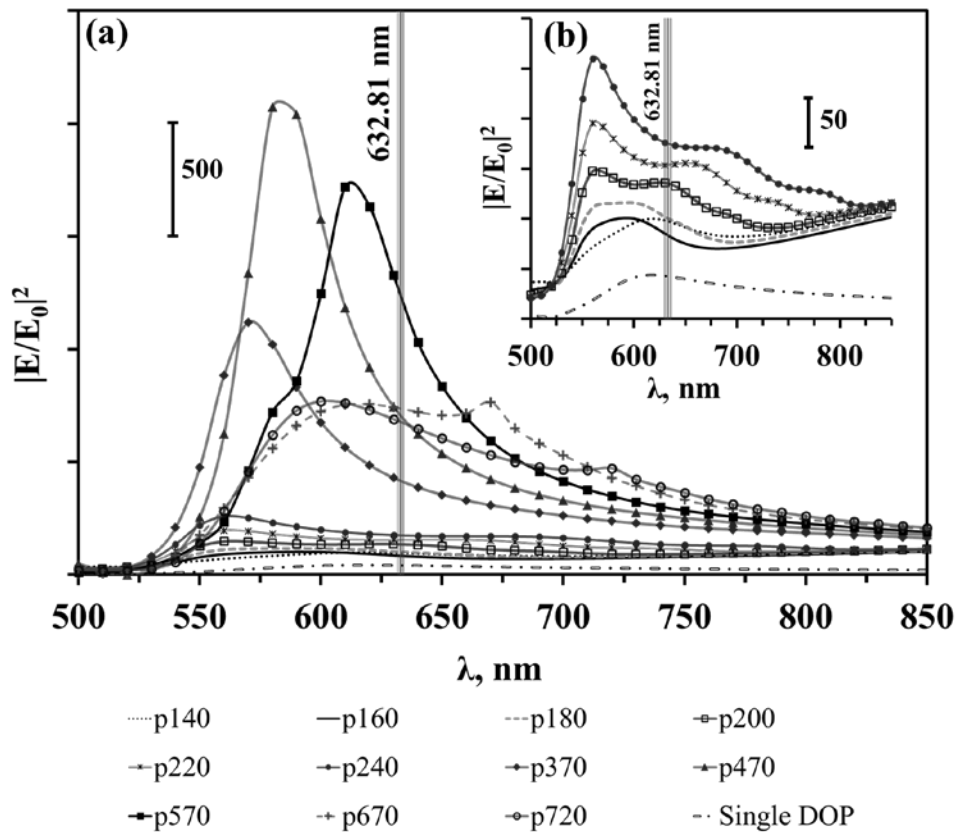


Figure 3-3: FDTD modelling and projections. (a) $|E/E_0|^2$ vs. Excitation wavelength for all DOP; (b) Inset corresponds to $|E/E_0|^2$ vs. Excitation wavelength for a single DOP and p160 to p240; (c) Scatter plot for $|E/E_0|^2_{\max}$ vs. Excitation wavelength for all simulated pitches; (d) Projected $|E/E_0|^2$ with a simulated excitation source of 630 nm.

The disc-on-pillar pitch is hereon denoted by the term “pDOP” where “DOP” is replaced with the pitch in nm. Figure 3-3a and Figure 3-3b portray the spectral dependencies of near-field enhancement calculated for a single DOP and periodic DOP arrays with various pitches. According to the FDTD projections, the single DOP is expected to produce a plasmonic response weaker than periodic arrays despite that its maximum near field enhancement was at 620 nm (Figure 3-3a and Figure 3-3b). Likewise, a blueshift was observed for all pitches between p160 to p570 and p720. Only p670 underwent a redshift which interestingly had an $|E/E_0|^2_{\max}$ at 670 nm. No changes were noted in λ_{\max} for p200, p220 and p240 although a subsequent increase for $|E/E_0|^2_{\max}$ was observed as the interpillar distance augmented for each array region. The strongest enhancement amongst all studied pitches was depicted by p470 followed by p570, although these were still short of reaching the 630 nm target. Only p140 displayed the $|E/E_0|^2_{\max}$ at 620 nm (like the single pillar), but no significant increase in magnitude was achieved with this array.

The scatter plot allows for a clear visualization of how $|E/E_0|^2_{\max}$ is affected by the pitch (Figure 3-4). Consequently, the projections for the modelled excitation source of 630 nm were used to convey the fabrication plan for the DOP substrates (Figure 3-5). In summary, the modelling projects a strong plasmonic response near 632.81 nm for a pitch of 570 nm. The simulation data confirms that the plasmonic response of DOPs can be maximized for desired wavelengths through periodic spatial arrangements.

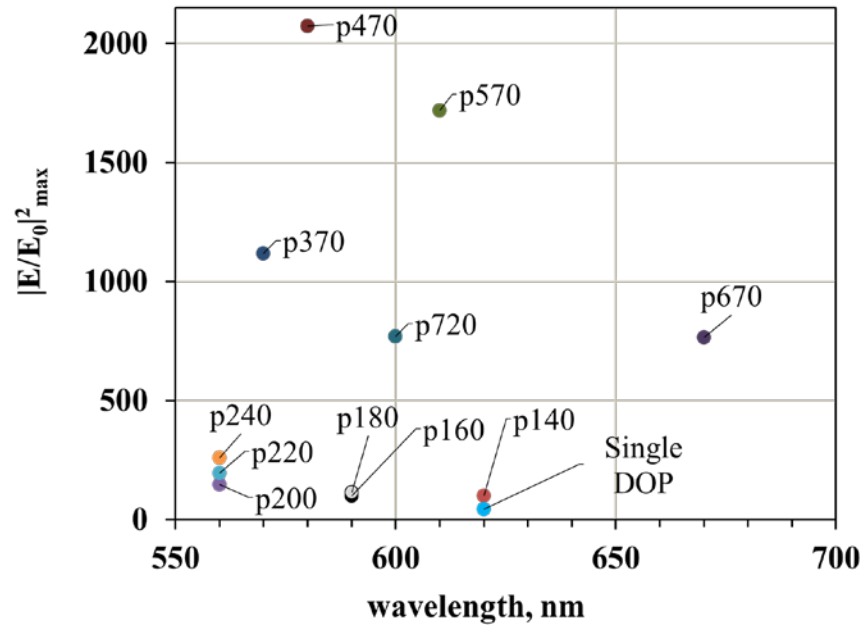


Figure 3-4: Scatter plot for $|E/E_0|^2_{\max}$ vs. Excitation wavelength for all simulated pitches

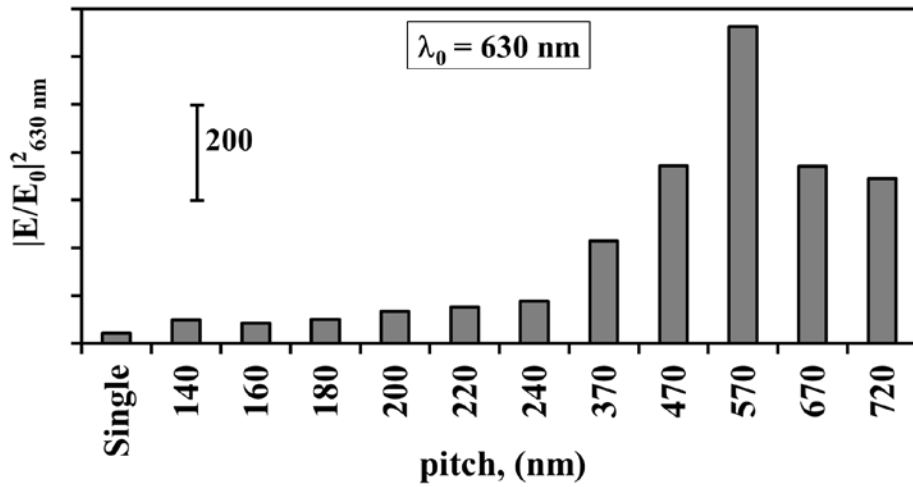


Figure 3-5: Projected $|E/E_0|^2$ with a simulated excitation source of 630 nm.

4 SURFACE-ENHANCED RAMAN SCATTERING STUDIES OF DISC-ON-PILLAR (DOP) ARRAYS: CONTRASTING ENHANCEMENT FACTOR WITH ANALYTICAL PERFORMANCE

Chapter 4 is an adaptation of a research article (accepted on 03/27/2019 and first published online on 04/16/2019) in Applied Spectroscopy by Raymond A. Velez, Nickolay V. Lavrik, Ivan I. Kravchenko, Michael J. Sepaniak, and Marco A. DeJesus:

R. A. Velez, N. V. Lavrik, I. I. Kravchenko, M. J. Sepaniak, M. A. D. Jesus. **Surface-Enhanced Raman Scattering (SERS) Studies of Disc-On-Pillar (DOP) Arrays: Contrasting Enhancement Factor with Analytical Performance.** Appl. Spectrosc. 2019. ##(##): ##### - #####. doi: 10.1177/0003702819846503.

The use of "we" in this chapter refers to the co-authors and me in the aforementioned citation. My primary contributions to this article included: (A) Design and Optimization of the FDTD Simulation Protocols, (B) Collection and processing of FDTD Simulations, (C) Data analysis of the FDTD data, (D) Collection and interpretation of the cited literature pertaining to FDTD, (E) Fabrication of the Nanostructures, (F) Development and optimization of the Raman testing protocols, (G) Acquisition and processing of all SERS data, (H) Data analysis and

interpretation of SERS data, (I) Collection and interpretation of most of the cited literature, and (J) Most of the writing.

Chapter 4 will focus on the fabrication process of the Disc-On-Pillar plasmonic arrays and SERS performance assessment which pertain to contribution items (E) to (J).

4.1 Introduction

Raman scattering is an information rich vibrational spectroscopy technique that has emerged as a promising tool for a diversity of biophysical and material science applications. Notwithstanding its benefits since its discovery in 1928 by C.V. Raman, the wide implementation of the technique in routine chemical analysis has been limited due to its inherently low cross section that leads to only one out of every 10^7 molecules to exhibit a scattering response.¹³ It was not until the 1970's where the SERS effect was pioneered through independent studies performed by Fleischmann, Jeanmaire, Van Duyne, and Moskovits.¹⁶⁻¹⁹ All coincided in observing significant Raman signal enhancements resulting from interactions between adsorbates and a roughened silver surface. Significant strides have been made on substrate development since it has been observed that adjustments in simple geometrical parameters (i.e. interparticle space, gap and morphology) can tune plasmonic responses to specific excitation frequencies thus optimizing substrate performance and reproducibility.⁴⁴⁻⁵¹

The enhancement factor (EF) is the analytical figure of merit that has gained scientific acceptance to assess the electromagnetic performance of a SERS substrate. The standard reference materials used in these analyses include benzenethiol which exhibits a combination of

both electromagnetic (EM) and chemical enhancements (CE).⁵² CE is attributed to diverse charge transfer (CT) mechanisms resulting from the chemisorption of the analyte on surface active sites of the metal although its contribution to the overall SERS enhancement ranges from 10 to 100.^{21, 27, 30-32, 53} Most attention has been focused on the EM since it has been estimated to produce the highest enhancement factors (10^6 to 10^{12}) by the localized surface plasmons resulting from the coupling of light with free electrons of the noble metals.^{20, 32}

Since the introduction of nanolithography, the majority of SERS nanofabrication studies has been aimed at the construction of substrates with small interparticle gaps and densities as the precursor for exceptional EF values.^{25, 31, 54-60} However, specifications for the substrate needed for routine quantitative analysis demands other than just a strong EF, such as good signal reproducibility, repeatability, and suitable quantitative range. Consequently, rational SERS substrate designing involves the construction of nanostructured arrays that exhibit a proper balance between strong EF and sample loading capacity that is sufficiently large for quantitative SERS measurements in a wide range of sample concentrations.

To our best knowledge, literature seldom has provided a concise approach to address the presumption of a high EF as analytical equivalent to acceptable quantitative performance. Hereon is presented a systematic study which contrasts the EF and analytical performance using an array of disc-on-pillar (DOP) nanostructures comprised of Ag/SiO₂/Si. Optimization analysis of the pillar array dimensions was achieved through Finite-Difference Time-Domain (FDTD) simulations (discussed in Chapter 3).

4.2 Experimental Section

4.2.1 Disc-on-Pillar (DOP) Fabrication

The general nanofabrication process used a previously cleaned single crystal silicon (SCS <100>) wafer. The nanofabrication recipe consisted of adding about 1 mL of P20 Adhesion Promoter and spin coating at 3000 rpm for 40 seconds. Afterwards, about 1 mL of ZEP 520A was applied and spin coated under the same conditions followed by a soft-bake at 180°C for 2 minutes thus producing the resist film with a final thickness about 250 nm. The substrate pattern was imprinted with a Jeol JX 9300FS electron beam lithography system (EBL) using a 400 $\mu\text{C}/\text{cm}^2$ dose. The total EBL process was completed in about 40 minutes. Pattern development was accomplished by submerging the wafer for 40s in Xylene, then another 40s in isopropyl alcohol (IPA), followed by a final IPA rinse and N_2 drying. The pattern was randomly checked (using a Nikon® Eclipse LV100 optical microscope (20x and 50x). A 15 s substrate descuming was performed with in an oxygen plasma asher (PVA Tepla Ion Wave 10). A 100 Å Cr mask was deposited under vacuum (4.7×10^{-6} torr), with a VE-240 dual electron gun evaporator at a rate of 1 Å/second. Lift-off process was achieved by submerging the wafer in an acetone bath for 60s, followed by a second 30 s clean on a fresh acetone batch. The cleaned surface was then rinsed with IPA and DIW. Si pillar arrays were rendered with a Plasma Lab System 100 Reactive Ion Etcher with a mixture of Ar/ C_4F_8 / SF_6 . After descuming, the etched substrate for 1 minute, the Cr mask was chemically removed by submerging substrates in CR14S for 2 minutes followed by 30 seconds of DIW. A thin, conformal layer (20 nm) of SiO_2 was deposited on the pillars using an Oxford ALD (202 cycles at 0.99 Å/cycle at 300°C). Refer to Figure 4-1 for a schematic of the DOP structure components and the fabrication process.

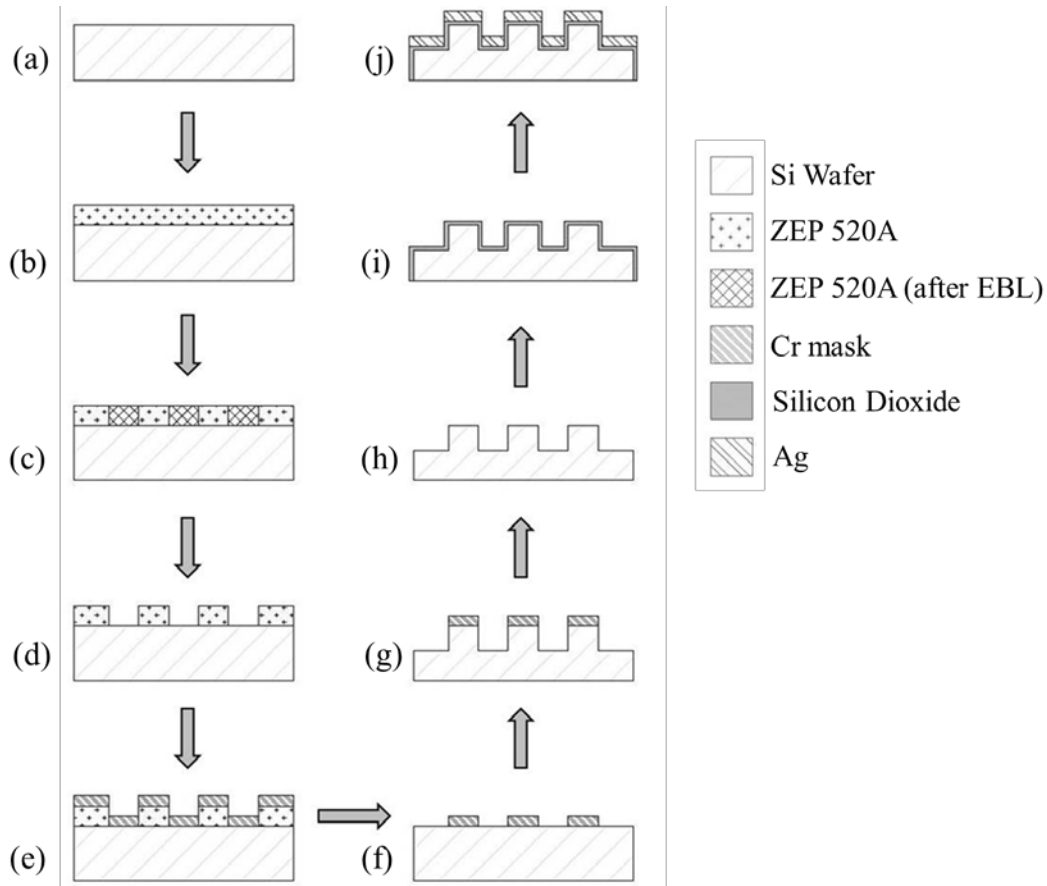


Figure 4-1: General fabrication summary of DOP periodic arrays (Drawings are not to scale). (a) Previously cleaned Si Wafer; (b) Addition of ZEP520A photoresist; (c) EBL-imprinting pattern; (d) Development and descuming; (e) Application of Cr mask; (f) Substrate after Lift-off; (g) Etched Si wafer; (h) After Cr stripping; (i) SiO₂ layer growth; (j) Metallization via PVD.

Table 4-1 shows the target pitches fabricated after evaluation of FDTD simulations. The DOP fabrication plan consisted of producing chips from a Si wafer (diameter = 4 inches) having (n × n) pillar arrays in a 2 × 2, 4 × 4, and 8 × 8 pattern, as well as a DOP fully occupied 24 μm ×

24 μm region. A 30 μm gap was left between individual array regions to avoid scattering interferences from neighboring pillars with different pitch.

Table 4-1: Disc-on-Pillar (DOP) Periodic Spatial Dimensions

| pitch / gap, nm | pitch / gap, nm | pitch / gap, nm |
|-----------------|-----------------|-----------------|
| 140 / 20 | 320 / 200 | 570 / 450 |
| 150 / 30 | 370 / 250 | 620 / 500 |
| 160 / 40 | 420 / 300 | 670 / 550 |
| 170 / 50 | 470 / 350 | 770 / 650 |
| 270 / 150 | 520 / 400 | 870 / 750 |

Micrographs of the SiO_2/Si DOPs were obtained using a Zeiss Merlin VP Scanning Electron Microscope (SEM). The general operational parameters used for obtaining micrographs were as follows: acceleration voltage (EHT) of 1.70 kV, column tilt of 30° , working distance (WD) of 4.9 mm, variable magnification (5 kx to 250 kx), and In-Lens detection.

Most of the DOPs were obtained with well-defined edges and without any considerable defects and surface artifacts (Figure 4-2). A minute fraction of the arrays, which mostly correspond to those with reduced interparticle spacing, did portray some defects. This is a foreseeable phenomenon that could be associated to manufacturing challenges such as lift-off of small interparticle spacing. Only arrays that meet the nanomanufacturing specifications were used for SERS assessment. In general, the fabrication recipe resulted in reproducible substrates with insignificant deviation from target dimensions (Table 4-2).

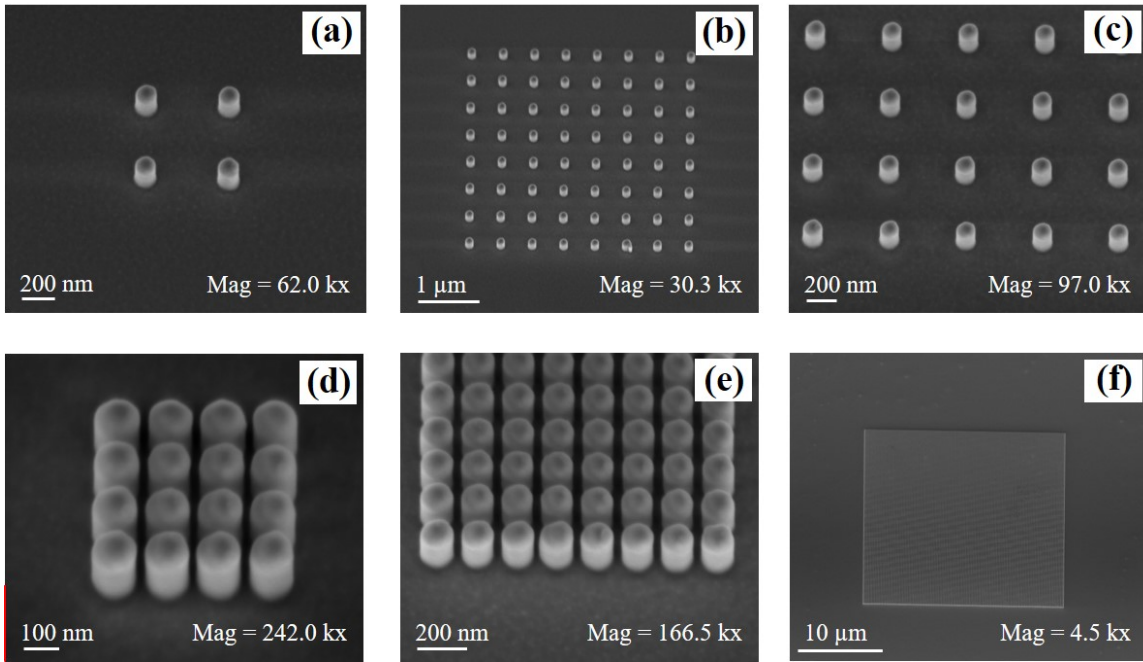


Figure 4-2: Si/SiO₂ DOP periodic arrays for (a) $p = 520$ nm, 2×2 ; (b) $p = 520$ nm, 8×8 ; (c) $p = 520$ nm, 8×8 (closer view of array) ; (d) $p = 160$ nm, 4×4 ; (e) $p = 160$ nm, 8×8 ; and (f) $24 \mu\text{m} \times 24 \mu\text{m}$ region with p160 DOPs. Dimensions are described in Table 4-2.

Table 4-2: DOP dimensions measured for pillar arrays ($n \times n$) or pillar regions (μm^2). Values correspond to target dimension / actual dimension with standard deviation ($n = 5$).

| DOP | pitch, nm | height, nm | diameter, nm |
|--------------------|---------------------------|---------------------------|-------------------------|
| 4×4 | 160 / 166.1 (± 0.9) | 175 / 172.9 (± 2.4) | 120/124.3 (± 1.2) |
| 8×8 | 160 / 162.9 (± 1.0) | 175 / 169.8 (± 2.0) | 120/123.3 (± 2.6) |
| 8×8 | 520 / 522.0 (± 1.6) | 175 / 172.1 (± 1.1) | 120/123.2 (± 1.5) |
| $24 \mu\text{m}^2$ | 160 / 162.9 (± 2.6) | 175 / 170.9 (± 2.0) | 120/122.4 (± 2.6) |

4.2.2 SERS Substrates and Standards

Unless otherwise specified, all reagents used had a minimum 99.9% purity and were used without further treatment. Ethanol, xylene, isopropyl alcohol (IPA), and acetone used for either DOP fabrication or standard solution preparations were HPLC Grade (Fisher Scientific). Aqueous solutions were prepared using 18 m Ω deionized water (DIW) obtained from a purification system (Barnstead, Co.). The silver shots (Alfa Aesar) used for metal deposition on silicon-based substrates were of reference standard grade (99.9999%). Benzenethiol (Acros Chemicals) was used to prepare a 1.0×10^{-3} M stock solution in ethanol (EtOH). An aliquot of the stock was diluted in 50% (v/v) DIW/EtOH to produce a 1.0×10^{-5} M working solution. 4-aminobenzoic acid (Sigma-Aldrich) was diluted in a 10% (v/v) ethanol to a concentration of 1.0×10^{-4} M. A portion of the stock was then diluted in DIW to its final concentration of 1.0×10^{-5} M. Rhodamine 6G (R6G) was obtained from Sigma Aldrich for assessment of calibration sensitivity.

4.2.3 Calibration Sensitivity (σ)

A 4.76×10^{-3} M stock solution of R6G was diluted as needed to prepare working standard solutions. The calibration sensitivity was assessed using R6G solutions with concentrations ranging from 5.20×10^{-6} M to 1.20×10^{-3} M.

In summary, a 20 μ L drop was placed on the chip and covered with a microscope coverslip. Replicate Raman spectra for the periodicities of interest were obtained immediately. Afterwards, the chip was washed with copious amounts of DIW, EtOH, and a final rinse of DIW followed by air drying. Spectra for R6G standards were obtained in a random order. A blank

spectrum of the chip was acquired prior to obtaining an R6G reading to confirm the absence of interferences from the previous sample.

R6G was not considered for determination of EF because the SERS response would be a result of plasmonic, chemical, and resonant enhancements, thus interfering with the determination of the LSP (electromagnetic) contribution to the EF. However, R6G resulted attractive to assess sensitivity in order to determine the breadth of the detection range for a SERS platform with an optimized plasmonic response. Spectra of 4-ABA samples at concentrations of 10^{-4} M and 10^{-5} M were obtained for pillar arrays of interest to further elucidate the performance of the optimized DOP system with an analyte of moderate physisorption onto the SERS surface.

4.2.4 SERS Assessment

The DOPs were rendered SERS active by depositing a $25 (\pm 0.2)$ nm silver layer under vacuum (10^{-6} torr) on a physical vapor deposition (PVD) apparatus (Cooke Vacuum Products, Inc.). Reference standard grade Ag (99.9999%) was deposited at a rate of $1.0 (\pm 0.1)$ Å/s until reaching the desired thickness. The metallized DOP remained under vacuum for at least 15 minutes prior to performing chemical analysis.

Benzenethiol (BT) was used as a standard reference material to calculate the SERS Substrate Enhancement Factor (SSEF). The SERS response for BT is due mostly to the plasmonic enhancement produced through the surface interactions with the Ag disc and not by other enhancement mechanisms (i.e. resonance and chemical) that are either not present (resonance) or the contributions to the overall SERS signal are insignificant (chemical

enhancement). Hence, it is reasonable to establish the SSEF calculated for the DOP system using BT as an effect of the LSP associated to the Ag disc dimensions.

A BT self-assembled monolayer (BT-SAM) was achieved on the Ag surface by submerging the chip in 7.5 mL of a 1×10^{-5} M solution and moving the recipient in a circular motion for approximately 15 minutes. Afterwards it was dipped in DIW, rinsed with an excess of DIW (~150 mL) to remove any excess BT, and finally dried with N₂. The calculated total surface area of the chip containing the DOP arrays is 0.16 cm². Based on the BT packing density of 6.80×10^{14} molecules / cm², it was estimated that 1.09×10^{14} BT molecules are required for full surface coverage. The volume of the BT solution used corresponds to 4.52×10^{16} molecules which is past the monolayer threshold of the surface thus making it of a suitable concentration for the DOP assessment within the allocated exposure time. A simplified temporal study was performed to confirm the adequacy of exposure time (refer to Appendix 1).

The Raman mapping of the chip surface was performed without further sample treatment. Raman spectra were acquired within 24 hours of creating the BT-SAM. The area of the 1075 cm⁻¹ band, corresponding to the C-S stretching, was used for assessment of the SSEF (Eq. 4-1).

$$SSEF_{1075\text{ cm}^{-1}} = \frac{N_{vol} I_{SERS}}{N_{surf} I_{RS}} \quad (4-1)$$

where N_{vol} is the average amount of BT molecules in the scattering volume of the normal Raman measurement, I_{SERS} is the BT signal obtained with the DOP system, N_{surf} is the number of BT molecules adsorbed on the Ag disc, and I_{RS} is the normal Raman signal of the BT neat sample. For this study, SSEF was considered instead of the general EF calculation commonly found in

literature since the enhancement is a result of molecular interactions occurring at the metal substrate surface (Eq. 4-2).^{26, 32}

$$EF = \frac{N_{vol} I_{surf}}{N_{surf} I_{vol}} \quad (4-2)$$

where I_{surf} and I_{vol} are the SERS response and normal raman response respectively of the BT molecules probed. It can be argued that both equations appear to be the same and that it is obvious that the BT signals compared are of the neat sample and those adsorbed on the DOP surface. However, the general EF Equation (4-2) is rather broad since it gives an EF value under the presumption that all molecules (indistinctively if these are on the LSP or not) within the integrated surface area of the laser spot contribute to the enhancement (I_{surf} / N_{surf}). Consistent with the surface spectroscopy character of SERS, the SSEF equation capitalizes on the SERS signal (I_{SERS}) dependency in the number of molecules adsorbed on the Ag disc, where the localized field enhancement occurs (as demonstrated with FDTD simulations).

Referent the Ag mirrors in pillar array systems, previous studies by our group reported this area to be rendered SERS inactive because these are beyond the percolation threshold for the plasmonic response.⁶¹ It should also be noted that the early research activities of the group have taken into account the amount of molecules that adsorbed unto the individual substrate features as the major contributor to the SERS signal despite that Equation (4-2) has been used for EF calculations.^{44, 45, 62} We are reporting the enhancement using the SSEF since the intent of this portion of the study is to effectively establish the enhancement factor of a system with an optimized plasmonic response at the SERS active sites.

The total surface area of an individual Ag disc (A_{DOP}) that will contribute to N_{surf} is given by the sum of the disc top ($A_{top} = \pi r^2$) and disc side wall ($A_{wall} = 2 \pi r h$) which is approximately $2.07 \times 10^{-10} \text{ cm}^2/\text{pillar}$. Using the BT packing density of $6.80 \times 10^{14} \text{ molecules / cm}^2$ (extensively reported elsewhere), the total amount of BT molecules covering the Ag disc is estimated to be 1.41×10^5 .⁶³⁻⁶⁵

4.2.5 Raman Operational Parameters

Mapping of the DOP periodic array regimes was performed with a JY-Horiba LabRAM microscope equipped with a HeNe laser ($\lambda = 632.81 \text{ nm}$, power = 9.82 mW) and a long working distance 50x objective (NA = 0.45 μm , effective spot size = 2.0 μm). The raman spectrometer was aligned and the signal calibrated and maximized for mapping of the DOP systems. Individual spectra were measured with 1 second acquisition time. SERS spectra for mapping were acquired on a 1 $\mu\text{m} \times 1 \mu\text{m}$ grid with the same acquisition time per spectrum. A 600 nm grating, 400 μm aperture, and 441 μm slit width were used in all SERS measurements. The spectral range was from 138 cm^{-1} to 3058 cm^{-1} . All spectra were baseline corrected and background subtracted (where the background consisted of the metallized substrate surface outside the vicinity of the pillars area).

4.3 Results and Discussion

4.3.1 SERS Performance of DOP Arrays

This portion of the discussion will contrast the plasmonic performance of the fabricated DOP arrays, 2×2 , 4×4 , and 8×8 , as well as the 24 $\mu\text{m} \times 24 \mu\text{m}$ region, using the 1075 cm^{-1} band (ν_{C-s}) average response ($n = 3$) of the BT spectra. Moreover, the reliability of the FDTD

simulations as a predictive tool is checked. As stated previously, it is expected that only pillars confined within the beam spot are to produce the overall SERS response. This is accounted for by the systematic determination of the maximum allowable pillars (MAP) for each DOP array (refer to Appendix 2 for information pertaining to MAP details and calculations). However, not all pillars within an array system will be confined within the beam spot, hence, multiple scans are needed to probe the full area of the periodic arrangement. In this study, only the 2×2 arrays have the total pillars within the $2.0 \mu\text{m}$ beam spot for all the pitches studied. This is not possible for arrays with greater amounts of pillars (i.e. 8×8 array, $24 \mu\text{m}^2$ regions) because pillars will be located outside the laser spot as the inter-particle distance increases.

4.3.1.1 DOP Arrays: 2×2 , 4×4 , and 8×8

The 2×2 arrays produced a SERS response of variable intensities for each periodic arrangement (refer to Appendix 3). The strongest signal was observed for p520. The weakest response was registered for p140, p150, and p170, which were comparable to the single pillar response. All other pitches had similar responses. The SSEF are in the orders of 10^8 for p520, 10^6 for p140 and p150, and 10^7 for all others. An excellent correlation ($R^2 = 1.000$) was obtained for the SSEF and SERS response thereby demonstrating how the interparticle spacing can be adjusted to favor stronger LSPs. It should be noted that the amount of BT molecules probed in the 2×2 arrays can be considered constant for all pitches, thereby allowing a direct assessment of the SSEF without the need for signal normalization. The results for the 2×2 arrays are somewhat consistent with the projections from FDTD simulations, where the greatest response was expected to be rendered near a 520 nm pitch. However, p160 produced a greater signal than

modelling predictions since it was expected to have weak performance very similar to p140 and p150. Considering that FDTD simulation parameters use a periodic boundary where the plasmonic response of the DOP is based on an infinite array of pillars, the experimental system should render a response profile comparable to that from the modelling predictions as the number of pillars in the array increases.⁶⁶ Based on this, as the array order increased, from 4×4 pattern to the $24 \mu\text{m} \times 24 \mu\text{m}$ DOP region, the intensity profile is expected to portray a response profile similar to the modelling.

The 4×4 arrays rendered a stronger SERS response than the 2×2 arrays confirming that a signal strengthening is expected for the pitches by increasing the available pillars in the DOP system (refer to Appendix 3). The strongest response was observed for p520, like the 2×2 arrays and consistent with simulated predictions. All pitches for the 4×4 arrays produced a plasmonic signal inherently stronger than the single pillar. Enhancement factors were within the 10^7 order of magnitude for all pitches with the stronger SSEFs corresponding to p520. The MAP values for the 4×4 arrays are consistent at 16 pillars from p140 to p420. Afterwards, there is a gradual decrease in the number of pillars occupying the beam spot from p470 (14 pillars) until p870 (4 pillars). This is interesting because approximately 75% of the total pillars in the p520 array are producing the strongest signal. Normalization of the SERS intensity by MAP shows the contribution of each individual pillar in the array where performance of p520 prevails as the strongest. Also, the SSEF values correlate to the normalized response, a pattern already noticed with the 2×2 arrays.

The 8×8 arrays depicted a stronger response than 2×2 and 4×4 arrays (refer to Appendix 3). Calculated SSEF were in the 10^7 order for p370 to p870 (the largest for p520)

whereas all other pitches had SSEF values at 10^6 . The strongest SERS response is given by p520 although the raw signal portrays a profile that is not consistent to the simulations. A slight bimodal character is observed for pitches p140 to p320 for which a thorough explanation is provided in the discussion of the $24\ \mu\text{m} \times 24\ \mu\text{m}$ array regions. Normalization with the number of pillars within the beam spot adjusted the signal profile as per FDTD simulations. Considering the MAP for 8×8 arrays, the full 64 pillars were illuminated for DOP systems from p140 to p170. All other pitches had a gradual decrease of pillars covered by the laser spot until p870 where MAP is 4 pillars. Despite the significant reduction in the number of irradiated pillars due to the greater interparticle spacing, the signal intensity continued increasing until reaching a maximum output at p520.

The overall augmentation in SERS response with the pitch increase was observed for 2×2 , 4×4 , and 8×8 arrays. It was more pronounced as the array order increased even when MAP for the latter two systems had a similar number of illuminated pillars with several pitches. For example, p520 has a MAP value of 12 in both 4×4 and 8×8 arrays, yet the latter rendered greater SERS response by a factor of 1.2 (see Table 4-3 in Section 4.3.2 for additional details on this particular). This suggests that the pillar-to-pillar interactions leading to an enhanced SERS response has contributions from the illuminated pillars as well as their neighboring pillars. The data for the $24\ \mu\text{m} \times 24\ \mu\text{m}$ region discussed hereon confirms this behavior.

4.3.1.2 DOP Region: $24\ \mu\text{m} \times 24\ \mu\text{m}$

The $n \times n$ array systems discussed until now have a defined number of pillars which were not always fully illuminated except when considering small interparticle spacing (i.e. p140,

p160). Populating a $24\ \mu\text{m} \times 24\ \mu\text{m}$ area with DOP arrays assures the effective beam spot is saturated with pillars, thereby allowing an adequate assessment of how the pitch order effects the SERS signal for each pitch. Also, a suitable approximation to an infinite period, as seen in the FDTD simulations, is better achieved with the $24\ \mu\text{m} \times 24\ \mu\text{m}$ array regions than with smaller array systems.

A consistent and homogeneous field enhancement is seen throughout the surface with several random hot spots that exhibit somewhat higher intensities (Figure 4-3a). The weaker response noticed at the initial $2\ \mu\text{m}$ of the array perimeter is consistent with the $2\ \mu\text{m}$ diameter beam used to scan with $1\ \mu\text{m}$ steps. Representative BT spectra of the pillar arrays as well as the adjacent regions beyond the $24\ \mu\text{m} \times 24\ \mu\text{m}$ area confirms the SERS signal is produced where the DOPs are located (Figure 4-3b).

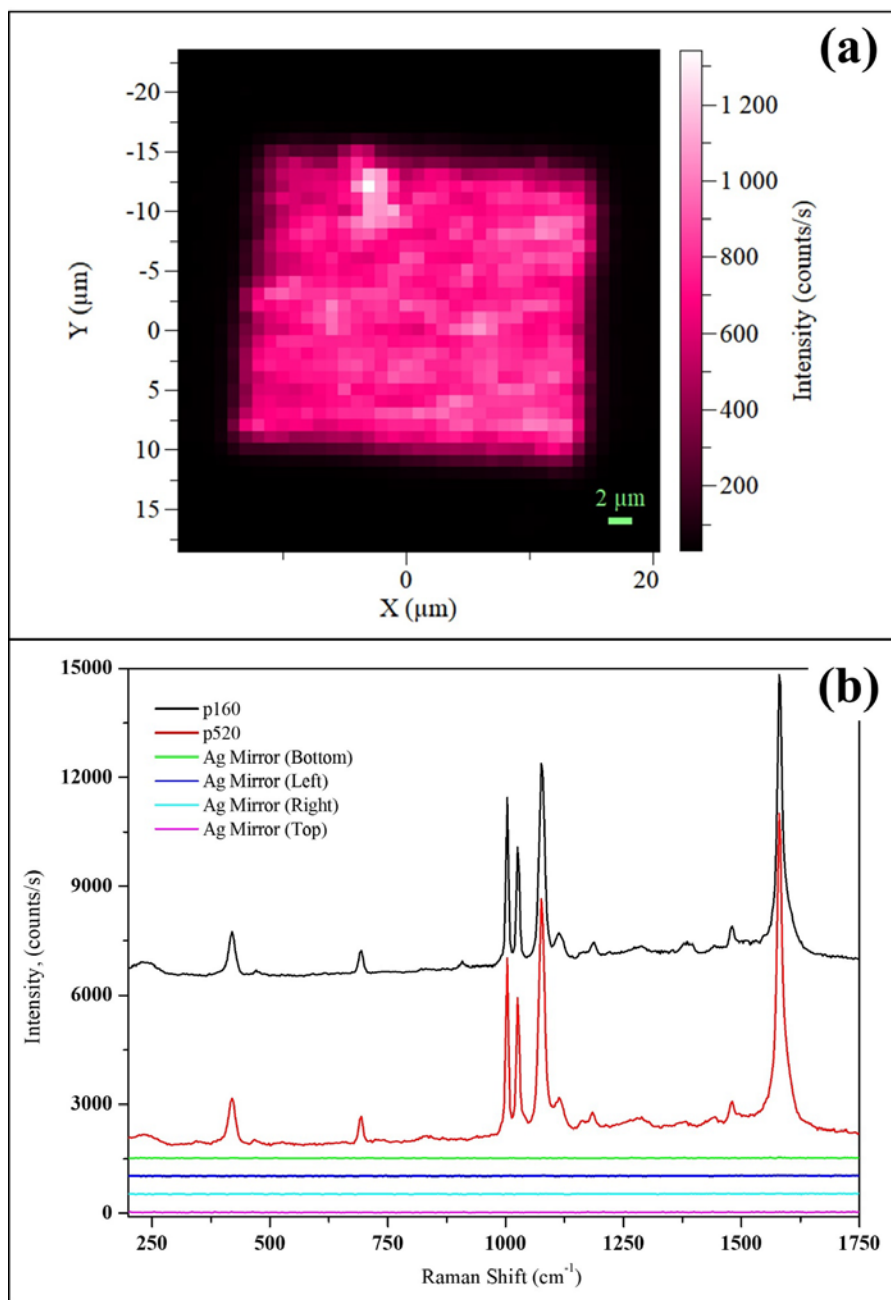


Figure 4-3: (a) SERS mapping of 24 μm × 24 μm DOP region using 1 μm steps. The weaker response noticed at the initial 2 μm of the array perimeter is consistent with a 2 μm diameter beam spot that is scanning at 1 μm steps. The map shows the signal of the C-S band across the DOP system which suggest a consistent adsorption of BT at the Ag disc surface. (b) Mean SERS spectra of the 24 μm × 24 μm DOP region using 1 μm steps at p160 and p520. The Ag mirror surrounding the pillar arrays is depicted by the lower four spectra and do not render a SERS active signal.

SSEFs were calculated from triplicate measurements around the array center (Figure 4-4) as well as the average signal of the full pillar region as determined by LabSpec software (refer to Appendix 3). Both types of measurements, center-only and full-region, rendered SSEFs at 10^7 for p140 to p370 and p870. DOPs corresponding from p420 to p770 had SSEFs at 10^8 . As with other arrays, the p520 was attributed the greatest SSEF although a bimodal peak performance is observed where p160 produced a comparable SERS response. After normalization with MAP, the relative intensities portrayed a pattern like the FDTD projections where p520 is attributed the strongest SERS response.

The normalized response between both measuring modes, center and full array, portrayed an excellent correlation ($R^2 = 0.9921$), meaning that the contributions of each pillar to the SERS signal is consistent either it be the 12 pillars corresponding to the MAP of p520 or the 2209 (total) pillars in the $24 \mu\text{m} \times 24 \mu\text{m}$ region. The average SERS raw signal obtained by mapping the full $24 \mu\text{m} \times 24 \mu\text{m}$ region was greatest for p160 followed by p520, whereas the center reading attributes the strongest response to p520 followed by p160. The differences in SERS intensity trends could be due to anomalies or imperfections in the pillar surface that may result in signal variability. However, p160 and p520 offer the strongest overall SERS response either it be through mapping of the full DOP region or by attaining the signal at the array center. The bimodal profile observed for p160 and p520 can be attributed to additional resonances that occur with waveguides which are not observed when using absorbing regions in the current modelling parameters.^{67, 68}

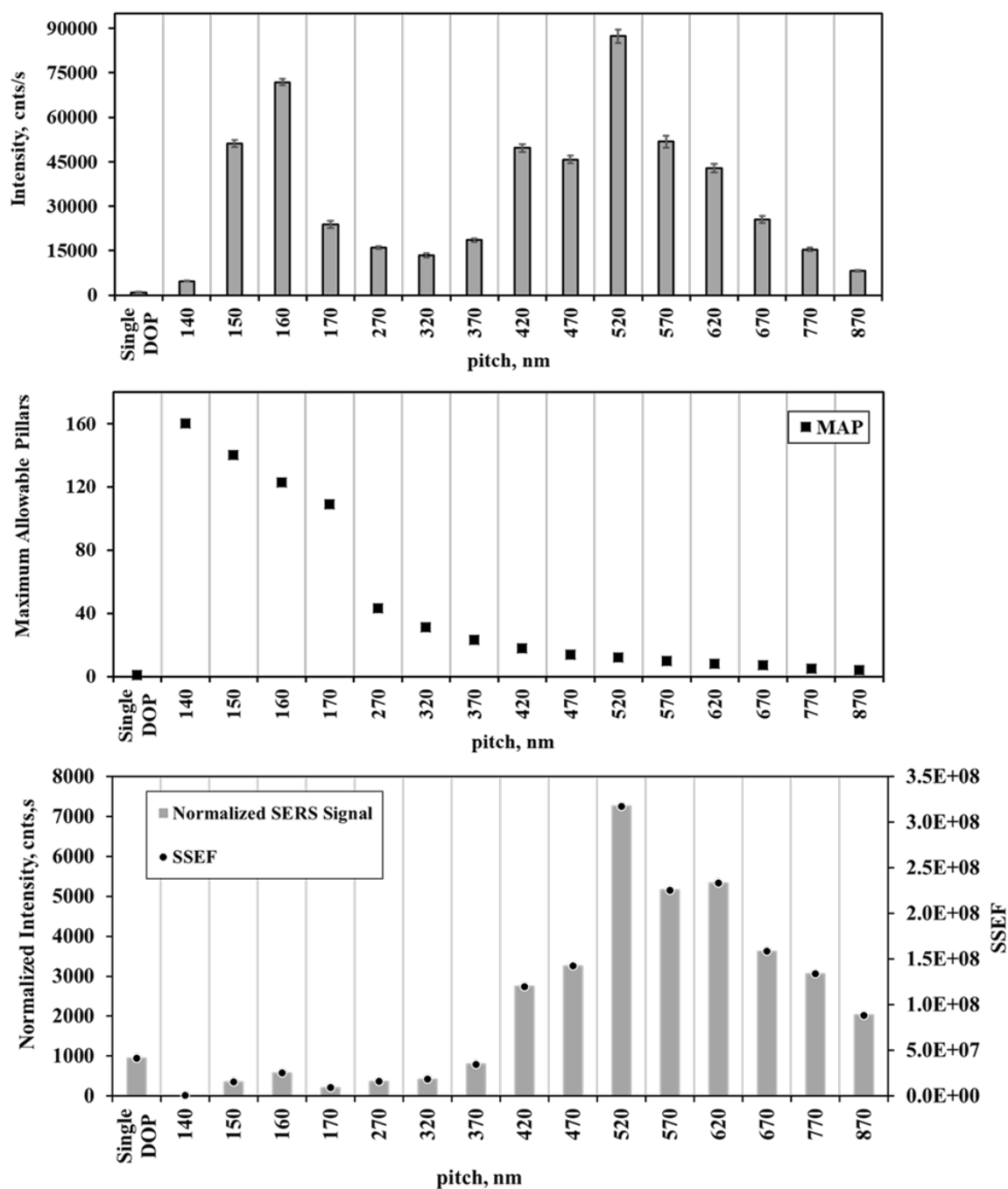


Figure 4-4: (top) BT SERS response for $24 \mu\text{m} \times 24 \mu\text{m}$ arrays measured around the center of the region. Error bars correspond to a standard deviation of 3 measurements with a CV of the SERS response ranging from 1.5% to 5.2% for each pitch. (middle) MAP as a function of pitch for a $2.0 \mu\text{m}$ laser beam spot. (bottom) BT SERS response after normalization with MAP and calculated SSEF.

4.3.2 Effects of Array Order on SERS Response

The experimental data has shown that the DOP arrays can be tailored for optimal SERS response by varying the pitch. However, even when keeping the pitch constant, stronger signals can be attained by increasing the number of pillars in the array. The p520 DOP system is used to exemplify the effects of the array order (refer to Appendix 4 for a detailed explanation of the calculations). Comparison of the single pillar and different size arrays of the 520 nm pitch are shown in

Table 4-3. The MAP for a 520 nm pitch places a maximum of 12 pillars within the beam spot, therefore the only difference between the arrays corresponding to 4×4 , 8×8 , and the $24 \mu\text{m} \times 24 \mu\text{m}$ region is the extent of neighboring pillars.

Table 4-3: DOP Pitch Order Response Factor for arrays with a 520 nm pitch.

| Array | Single DOP | 2×2 | 4×4 | 8×8 |
|--------------------|------------|--------------|--------------|--------------|
| 2×2 | 11.7 | - | - | - |
| 4×4 | 18.1 | 1.6 | - | - |
| 8×8 | 21.7 | 1.9 | 1.2 | - |
| $24 \mu\text{m}^2$ | 91.4 | 7.8 | 5.0 | 4.2 |

Interestingly, the experimental results show a concomitant increase in the SERS response with the DOP arrays despite that the number of pillars illuminated within the beam spot is constant. For instance, consider the performance of 4×4 and 8×8 arrays where the total pillars in each system are 16 and 64 respectively (rather than the irradiated ones). The 12 pillars illuminated in the 8×8 array rendered a stronger SERS response the 4×4 array by a factor of 1.2. However, the signal for the $24 \mu\text{m}^2$ region increased by a factor of 5.0 and 4.2 when compared to 4×4 and 8×8 arrays, respectively.

A suitable explanation for this effect is a signal percolation into the spot area due to the waveguide character of the SiO₂ in an array system. The energy refractance from the outer regions of the spot could be harvested into the numerical aperture of the microscope.⁶⁶ This particular effect is not captured in a finite-difference or finite-element model since the boundaries are treated as absorbing regions which do not account for reflections.^{67,68} Studies that have capitalized on waveguide modes to amplify the plasmonic response for SERS-based sensing have been reported.⁶⁹⁻⁷¹

In terms of the FDTD modelling, BT experimental results with MAP gives the contribution of a single pillar to the SERS signal which is equivalent to the periodic boundary (PB) condition used to simulate the EMF. Using PB simulation parameters does not confine the DOP to a specific $n \times n$ array, instead it uses an infinite amount of pillar arrays to determine the EMF. Normalization of the signal with the corresponding MAP value brought all periodicities to conform to that predicted by the FDTD.

The experimental data further substantiates the advantages of highly populated pillar array regions. First, no significant differences were noticed between measurements obtained around the array center and the full array region. This is greatly beneficial when probing samples multiple times without having to change the chip since the possibilities of thermal degradation in the illuminated spot area is minimized. Also, probing the central region instead of mapping the full array favors time efficiency without sacrificing signal intensity.

Considering the bimodal performance observed for pitches of 160 nm and 520 nm, the larger inter-pillar gaps in p520 provides a more feasible fabrication process, contrary to p160

where the small gaps may introduce fabrication challenges (i.e. consistent interpillar gaps, well-defined defined feature dimensions). Even so, probing the full region of the p160 is considerably attractive for applications where maximizing the number of SERS active sites is important such as single-molecule detection and remote sensing applications where mapping capabilities are hindered due to spectrometer size reduction.

4.3.3 DOP Analytical Performance

The binding to Ag through the thiol moiety is a characteristic that makes BT the choice to determine SSEF of the DOP system. However, it is of interest to assess if the DOP performance holds for analytes that have a moderate chemisorption to the Ag disc. Considering the periodic arrays that performed best with BT, the DOP systems for p160 and p520 were used for assessing the SERS performance using R6G and 4ABA as probes.

4.3.4 DOP performance with R6G

R6G is a cationic dye commonly used for demonstrating performance of SERS substrates. The basic structure of R6G is a xanthene group with a carboxyphenyl substituent in ortho position to the xanthene center ring.^{72, 73} DFT simulations have portrayed an optimized geometry for the R6G-Ag cluster with the long axis of the phenylcarboxy group rotated perpendicular to the long axis of the xanthene moiety.⁷⁴

Raman spectra depicted the typical profile for R6G with bands corresponding to C-C-C in-plane vibrations (613 cm^{-1}), C-H bending (773 cm^{-1} and 1185 cm^{-1}), and aromatic stretching (between 1300 cm^{-1} and 1700 cm^{-1}) all which have made this molecule an attractive probe for

SERS activity assessment (Figure 4-5a). The 773 cm^{-1} band was chosen to assess the calibration sensitivity (σ) because (1) it is fully resolved from other bands, (2) it corresponds to the in-plane bending of the xanthene ring which is expected to be nearest to the Ag surface due to the Ag-N interactions of the amino substituents, and (3) changes in intensity for bands above 1000 cm^{-1} have been attributed to R6G photolytic degradation mediated by Ag nanoparticles.⁷³⁻⁷⁵

Besides constructing calibration curves for p160 and p520 DOPs, additional spectra were obtained for p140, p270, and p870 to confirm that SERS activity were less than the target arrays (Figure 4-5b). A reduction in the R6G SERS response is observed for these periodicities which is consistent with the BT results when testing for SSEF.

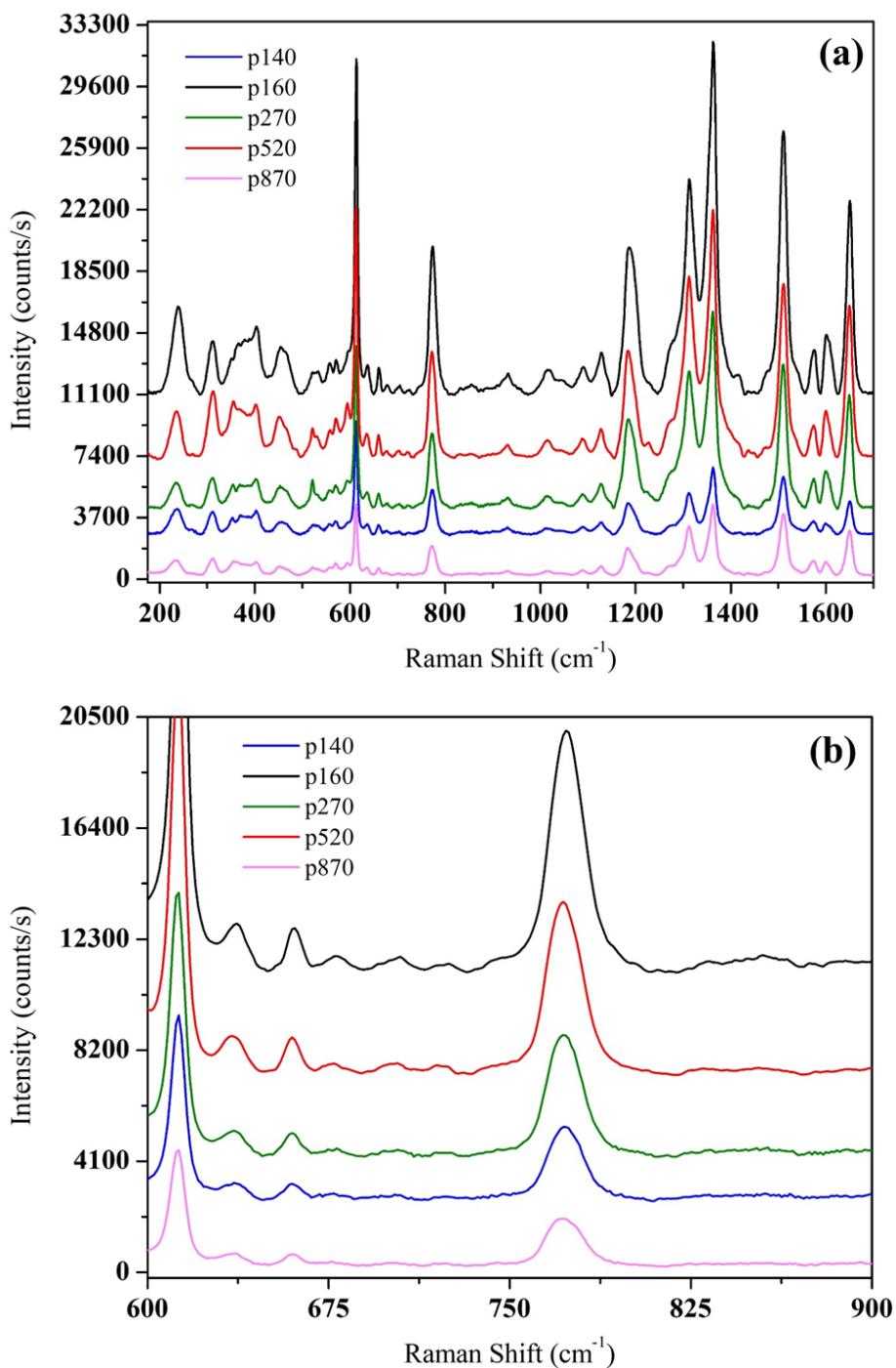


Figure 4-5: (a) SERS spectra for R6G (1.19×10^{-3} M) for a center measurement of the $24 \mu\text{m} \times 24 \mu\text{m}$ region for p140, p160, p270, p520, and p870 arrays. (b) 773 cm^{-1} band corresponding to the R6G xantheno in-plane bending. Spectra were polynomial baseline corrected. All spectra are offset in the y-axis for clarity.

There are notable differences in the working curves generated for p160 and p520 (Figure 4-6). The σ for R6G is given by the slope of the linear best fit which is 9.15×10^7 a.u./M and 3.46×10^8 a.u./M for p160 and p520 respectively. Despite that a greater σ value is portrayed by p520, it has a lower limit of linearity than p160. A pseudo-linear response ($R^2 = 0.9633$) for p520 was observed up to 1.19×10^{-4} M R6G followed by signal saturation at greater concentrations. This is not evident for p160 which was linear ($R^2 = 0.9910$) for the total range of concentrations studied.

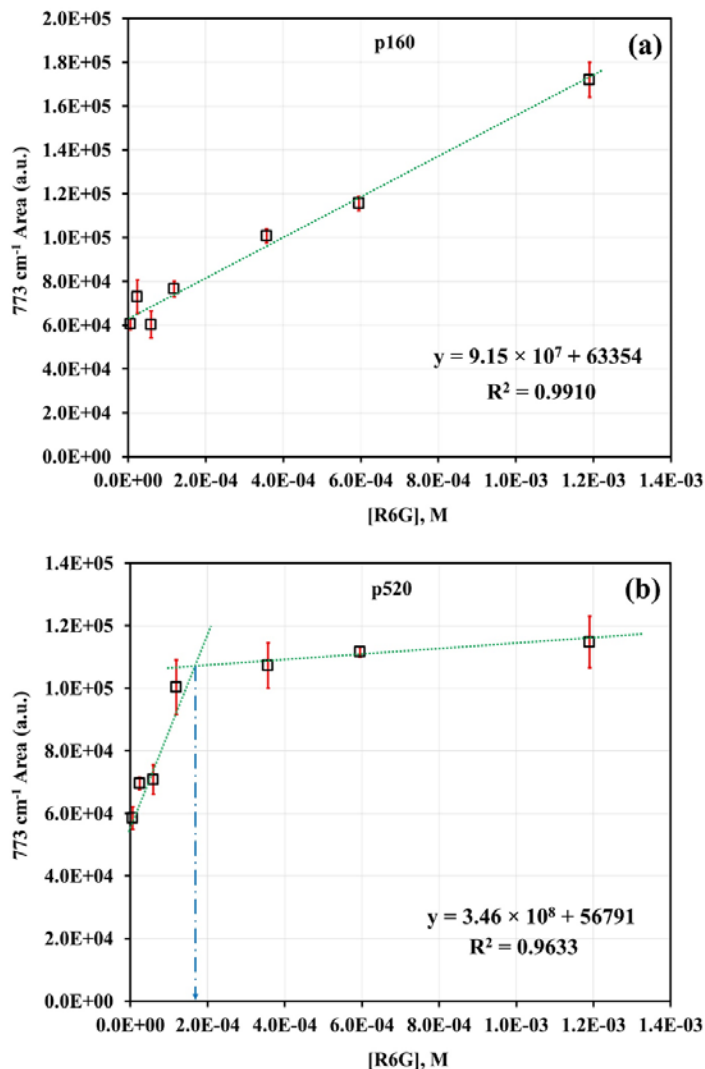


Figure 4-6: R6G working curves (5.95×10^{-6} M to 1.19×10^{-3} M) using (a) p160 and (b) p520. The error bars for both p160 and p520 correspond to duplicate measurements at each calibration level. The dashed blue lines are the linear best fit for each period. Signal saturation for the 773 cm⁻¹ band is estimated at 1.44×10^{-4} M for p520 (vertical dash-dot-dash line in graph b).

The difference in sensitivity can

be attributed to the EMF generated by each DOP system. The raw SERS measurements for BT with the $24\ \mu\text{m} \times 24\ \mu\text{m}$ array were 71,890 counts/s and 87,412 counts/s for p160 and p520 respectively, which is a relative difference of 19.5%. Applying the MAP value for each array gave the contribution of a single pillar which is greater for p520 (7284 counts/s) than for p160 (584 counts/s) by a factor of 12.5. Consequently, p520 seems more attractive for applications where high sensitivity is desired (i.e. single molecule detection), however at the expense of decreasing the sample interaction probabilities due to the reduced number of available pillars.

The most probable cause for the p520 signal saturation is attributed to the amount of SERS active sites available for interaction with R6G molecules. In the $24\ \mu\text{m} \times 24\ \mu\text{m}$ array, the 160 nm pitch has 22,500 pillars, while a 520 nm pitch provides only 2,209. Considering a single measurement with a $2\ \mu\text{m}$ beam spot, the MAP of 12 pillars for p520 has only 2% of the 123 pillars provided by p160. This further translates into a SERS active surface area of $2.55 \times 10^{-8}\ \text{cm}^2$ and $2.49 \times 10^{-9}\ \text{cm}^2$ for p160 and p520 respectively, which is a difference of one order magnitude for a single measurement.

R6G molecules will reside in areas where there are no pillars as well as on the Ag disc of the pillars. However, one must consider that the effective SERS signal corresponds to those molecules interacting with the Ag disc surface where the strongest field enhancement is rendered as per FDTD modelling. This can be seen with the linear response of the R6G rendered by each DOP array. Considering that there are significantly fewer pillars for p520, the signal will be limited to the number of molecules that interact with the SERS active sites. Consequently, the total pillar surface for p520 is expected to be fully populated with fewer molecules than for p160.

It is to our understanding that the packing density for R6G has not been reported for systems like this. In addition, R6G in solution has been found to form two different dimers when interacting with silver particles thus making geometric calculations for substrate coverage even more challenging.^{76, 77} Hence, determining the total number of R6G molecules that will effectively cover the Ag disc of the DOP arrays will be prone to much error with the current capabilities, thus we did not pursue this particular.

It is no wonder that despite being a good probe for monitoring SERS activity, the geometrical complexities introduced by R6G makes it less convenient than thiol-based moieties for characterizing a surface with the scope of determining enhancement factors. Molecules such as BT and aminothiophenol (photodegradation product is BT) are of simple geometry and can easily form monolayers on metallized structures, as commonly described throughout literature.

4.3.5 DOP performance with 4-ABA

The 4-ABA spectra of 10^{-4} M and 10^{-5} M solutions were obtained using the $24\ \mu\text{m} \times 24\ \mu\text{m}$ array region for p160 and p520 (Figure 4-7). The stronger response was given by the p160 pillar system for both 4-ABA sample concentrations. The p520 produced significantly weaker SERS spectra to the extent where the bands of the 10^{-5} M sample were barely detectable. This could be attributed to the amount of interaction sites available for p160 which are 111 more than that available for the p520 arrays.

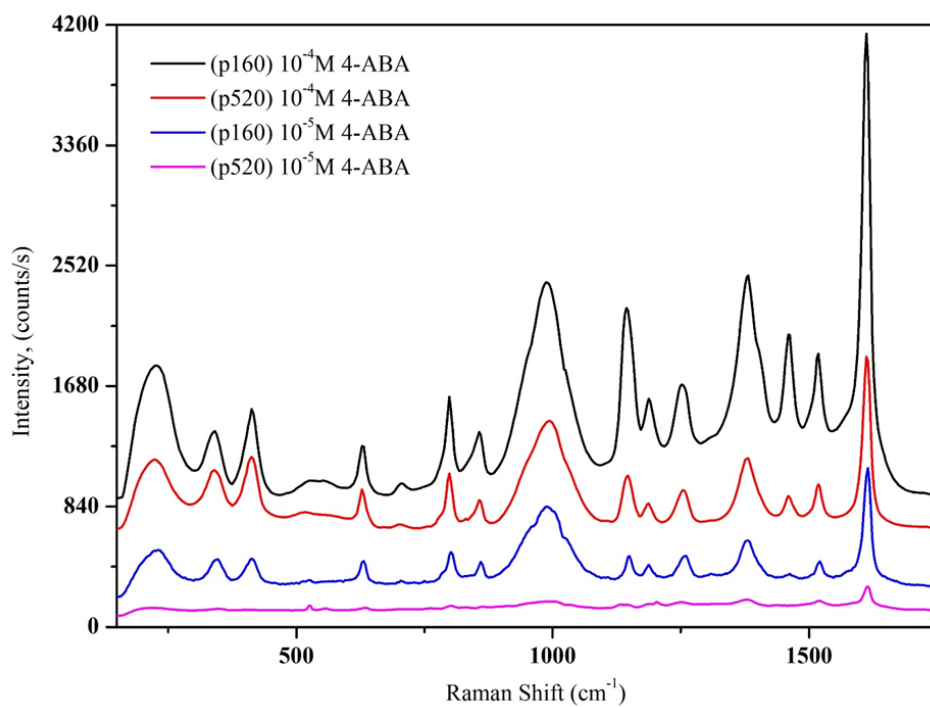


Figure 4-7: Contrasting SERS spectra of 4-aminobenzoic acid obtained using 24 $\mu\text{m} \times 24 \mu\text{m}$ DOP regions with a pitch of 160 nm and 520 nm. The spectra are offset in the y-axis for clarity.

5 CONCLUDING REMARKS

The overall excellent performance of using Finite-Difference Time-Domain simulations has been demonstrated in two separate case studies. The first pertains to a hybrid nanoarray system that had been manufactured and tested. A plausible explanation of the SERS plasmonic response was not clear, hence, requiring an assessment to validate and better understand its performance. The second case study regarded a design process of the Disc-on-Pillar plasmonic platform prior to fabrication. The dimensional properties and structural components were successfully optimized, and the SERS performance was validated with adequate chemical probes. In both cases, the FDTD projections were consistent with the SERS signal that was produced using thiol-based probes.

Considering the PEH Hybrid nanoarrays that was fabricated for multiwavelength SERS applications, the modelling depicted was capable of projecting where the surface plasmon resonances were concentrated. Moreover, it was consistent with the SERS experimental data. However, using FDTD modelling to contrast with nanoarrays comprised of single features (which had not been considered for manufacturing at the moment) revealed that the features have an affinity for certain wavelengths. Such is the case that some even appeared to not be SERS active from a given plane. However, changing the plane of view revealed that the LSPR was orthogonal to the polarization vector. Moreover, the data suggests that adjustments to the dimensional properties are required in order to bring the plasmon to a resonate with the desired excitation wavelength. Even so, the problem with poor near field enhancements was mitigated when the features were placed together in the hybrid arrangement. FDTD revealed a plasmonic

coupling between the features that rendered the SERS substrate active for the multiple wavelengths of the study. This fundamental information could not be obtained from physical experiments. Yet, FDTD was the tool that revealed this particular thus having a better understanding of the hybrid systems.

We have demonstrated the added value of using FDTD simulation software to optimize the dimensions of periodic arrays for SERS detection. The results depicted an extraordinary correlation with experimental data only after normalization of the signal by the number of pillars confined to the laser beam spot.

Furthermore, an increase in the array order within the same pitch resulted in an unforeseen strengthening of the signal. This suggests that the contribution of the pillars located at the periphery of illuminated pillars play a role in signal enhancement most likely due to the waveguide character of the DOP components. This particular discovery expands the parameters that can be explored to improve the designs of DOP array systems.

It is very interesting how outstanding enhancement factors are not necessarily attributed to densely-packed metallized substrates since further spaced particles can render exceptional SERS signals. However, molecules of moderate chemisorption, such as R6G, demonstrated that signal saturation can occur at lower concentrations when using arrays with large periodicities despite the calibration sensitivity for these were one magnitude order greater than the closely spaced pillars. Even so, the use of the denser DOP with a 160 nm pitch portrayed a response with a greater linear dynamic range. Moreover, as shown with 4-ABA, the smaller gaps produced a detectable spectrum while that for the DOP with greatest EF (calculated with the thiol analyte) was barely detectable when using other SERS probes. This further substantiates

that tailoring the geometries of plasmonic structures for specific excitation wavelengths can be achieved, but consideration must be given to the surface interactions of the targeted analytes.

As with all analytical methods, the calibration sensitivity will depend on how sensitive the detection system is towards the analyte. Unfortunately, a universal SERS substrate that will detect every available analyte does not exist, hence, it is of great importance that calibration sensitivity be assessed when screening new molecules. As an alternative, the functionalization of thiol-based probes could enable greater selectivity since this moiety adsorbs strongly to the surface of the metals mostly used for SERS applications, Ag and Au. Modifications to the sample matrix (i.e. pH adjustments, addition of dissolved ions) could be explored to improve the detection of the analytes.

Our findings show that optimization of SERS substrates based on periodic DOP arrays involves a nontrivial trade-off between the density of hot spots and the maximum field enhancement they provide. As opposed to a stochastic process, the DOP provides a means to address the analytical performance of a SERS platform by considering the packing density of the substrate in conjunction with the loading capacity.

The work presented in this study has the potential to be further developed for sensor applications due to the nano-scale feature size, the analytical performance conveyed, and the versatility to tailor the geometries for different detection wavelengths.

6 RECOMMENDATIONS FOR FUTURE WORKS

Regarding the hybrid PEH nanoarray system, it is recommended that the hexagon feature be rotated approximately 60°. This will bring the transversal axis of this geometric figure to be

aligned with the axis of polarization and with the transversal axis of the Ellipse feature (Figure 6-1). It is highly probable that a better coupling of the SPP will occur thus confining more energy and, consequently, harnessing stronger LSPRs. It is also recommended to increase the amount of arrays in the substrate (such as the DOP system described). The increase in signal should be somewhat proportional to the number of arrays available in the substrate independent of the beam spot size.

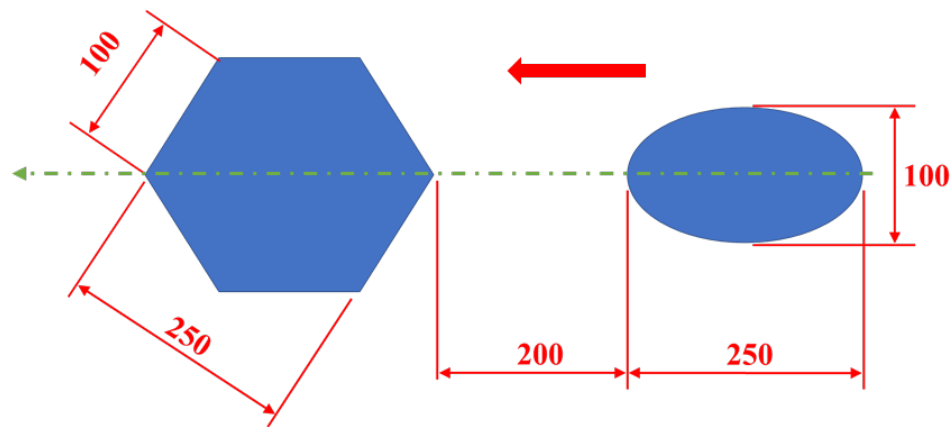


Figure 6-1: Proposed conformation for PEH arrays in which transversal axis of the hexagon and ellipse (indicated by green dashed arrow) are aligned with the polarization vector (red arrow) in order to enhance the plasmonic response.

A second recommendation is for a new plasmonic nanoarray system for increased plasmonic response and facile manufacturing process based on the aforementioned studies reported for PEH and DOPs. The Ag mirror of both hybrid PEH and DOP systems depicted a possible EM confinement. It is highly probable that the aim should be a simplification of the nanofabrication protocol in order to nurture high throughput and economically feasible processes. A succinct design presented with a near-field enhancement maximum value close to 785 nm which could be developed as the next generation of nanoarrays for plasmonic sensing (Figure 6-2).

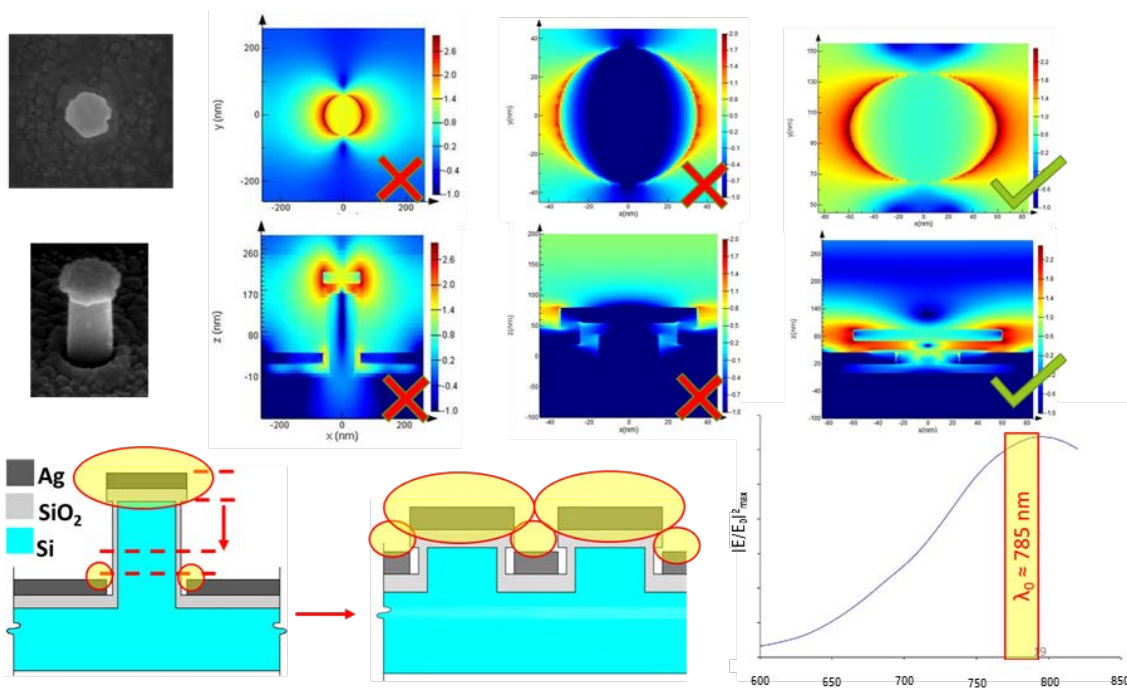


Figure 6-2: Proposed Nanoarrays for increased plasmonic sensing and feasible manufacturing based on current studies performed.

REFERENCES

1. D. L. Andrews, "Electromagnetic Radiation ☆", in *Encyclopedia of Spectroscopy and Spectrometry (Third Edition)*, J. C. Lindon, G. E. Tranter and D. W. Koppenaal, Eds. (Academic Press, Oxford, 2017), p. 427-431.
2. P. W. Milloni, "Wave-Particle Duality of Light: A Current Perspective", in *The Wave-Particle Dualism. Fundamental Theories of Physics*, S. Diner, D. Fargue, G. Lochack and F. Selleri, Eds. (Springer, Dordrecht, 1984).
3. H. Jiang, Z. Liu, Q. Sun, Y. E. D. L. X. Zhao, X. Zhang, "A demonstration of particle duality of light", in *ETOP 2017 Proceedings* (Optical Society of America, Hangzhou, 2017), p. 104523C.
4. J. C. Maxwell. VIII. A dynamical theory of the electromagnetic field. VIII. A dynamical theory of the electromagnetic field. 1865. 155: 459-512. doi: doi:10.1098/rstl.1865.0008.
5. D. Fleisch, D. Lemons. A Student's Guide to Maxwell's Equations. New York: Cambridge University Press, 2008. ed.
6. R. Fitzpatrick. Maxwell's Equations and the Principles of Electromagnetism. Hingham, Massachusetts: Infinity Science Press LLC, 2008. ed.
7. A. Kirsch, F. Hettlich. The Mathematical Theory of Time-Harmonic Maxwell's Equations: Expansion, Integral, and Variational Methods. Switzerland: Springer, 2015. 1st ed.
8. O. Passon, J. Grebe-Ellis. Planck's radiation law, the light quantum, and the prehistory of indistinguishability in the teaching of quantum mechanics. Planck's radiation law, the light quantum, and the prehistory of indistinguishability in the teaching of quantum mechanics. 2017. 38(3): 035404. doi: 10.1088/1361-6404/aa6134.
9. A. Einstein. Ist die Trägheit eines Körpers von seinem Energieinhalt abhängig? Ist die Trägheit eines Körpers von seinem Energieinhalt abhängig? 1905. 323(13): 639-641. doi: 10.1002/andp.19053231314.
10. A. B. Arons, M. B. Peppard. Einstein's Proposal of the Photon Concept—a Translation of the Annalen der Physik Paper of 1905. Einstein's Proposal of the Photon Concept—a Translation of the Annalen der Physik Paper of 1905. 1965. 33(5): 367-374. doi: 10.1119/1.1971542.
11. R. S. Krishnan, R. K. Shankar. Raman effect: History of the discovery. J. Raman Spectrosc. 1981. 10(1): 1-8. doi: 10.1002/jrs.1250100103.
12. C. V. Raman, G. T. Walker. On the molecular scattering of light in water and the colour of the sea. Proc. R. Soc. A. 1922. 101(708): 64-80. doi: doi:10.1098/rspa.1922.0025.
13. C. V. Raman. A New Radiation. Indian J. Phys. 1928. 2: 387-398. doi.
14. E. Smith, G. Dent. Modern Raman Spectroscopy: A Practical Approach. John Wiley and Sons, Ltd, 2005. 1st ed.

15. D. A. Long. *The Raman Effect: A Unified Treatment of the Theory of Raman Scattering by Molecules*. England: John Wiley & Sons, Ltd., 2002. ed.
16. M. Fleischmann, P. J. Hendra, A. J. McQuillan. Raman Spectra of Pyridine Adsorbed at a Silver Electrode. *Chem. Phys. Lett.* 1974. 26(2): 163-166. doi: 10.1016/0009-2614(74)85388-1.
17. D. L. Jeanmaire, R. P. Van Duyne. Surface raman spectroelectrochemistry: Part I. Heterocyclic, aromatic, and aliphatic amines adsorbed on the anodized silver electrode. *J. Electroanal. Chem. Interfacial Electrochem.* 1977. 84(1): 1-20. doi: 10.1016/S0022-0728(77)80224-6.
18. M. Moskovits, D. P. DiLella. Surface-Enhanced Raman Spectroscopy of Benzene and Benzene-d₆ Adsorbed on Silver. *J. Chem. Phys.* 1980. 73(12): 6068-6075. doi: 10.1063/1.440142.
19. M. Moskovits, D. P. DiLella. Enhanced Raman Spectra of Ethylene and Propylene Adsorbed on Silver. *Chem. Phys. Lett.* 1980. 73(3): 500-505. doi: 10.1016/0009-2614(80)80704-4.
20. M. Moskovits. Persistent Misconceptions Regarding SERS. *Phys. Chem. Chem. Phys.* 2013. 15: 5301-5311. doi: 10.1039/c2cp44030j.
21. N. S. Chong, K. Donthula, R. A. Davies, W. H. Ilsley, B. G. Ooi. Significance of Chemical Enhancement Effects in Surface-Enhanced Raman Scattering (SERS) Signals of Aniline and Aminobiphenyl Isomers. *Vib. Spectrosc.* 2015. 81: 22-31. doi: 10.1016/j.vibspec.2015.09.002.
22. Y. Fang, N. H. Seong, D. D. Dlott. Measurement of the Distribution of Site Enhancements in Surface-Enhanced Raman Scattering. *Measurement of the Distribution of Site Enhancements in Surface-Enhanced Raman Scattering*. 2008. 321: 388. doi.
23. G. H. Gu, J. S. Suh. Minimum Enhancement of Surface-Enhanced Raman Scattering for Single-Molecule Detections. *Minimum Enhancement of Surface-Enhanced Raman Scattering for Single-Molecule Detections*. 2009. 113: 8529. doi.
24. F. Hubenthal. Does the excitation of a plasmon resonance induce a strong chemical enhancement in SERS? On the relation between chemical interface damping and chemical enhancement in SERS. Does the excitation of a plasmon resonance induce a strong chemical enhancement in SERS? On the relation between chemical interface damping and chemical enhancement in SERS. 2014. 117(1): 1-5. doi: 10.1007/s00340-014-5907-x.
25. K. M. Kosuda, J. M. Bingham, K. L. Wustholz, R. P. Van Duyne. Nanostructures and Surface-Enhanced Raman Spectroscopy. In: D. L. Andrews, G. D. Scholes and G. P. Wiederrecht, editors. *Comprehensive Nanoscience and Technology*. Amsterdam: Academic Press, 2011. Vol. 3 Pp. 263-301.
26. E. C. Le Ru, E. Blackie, M. Meyer, P. G. Etchegoin. Surface Enhanced Raman Scattering Enhancement Factors: A Comprehensive Study. *J. Phys. Chem. C.* 2007. 111(37): 13794-13803. doi: 10.1021/jp0687908.

27. K. Kneipp. Chemical Contribution to SERS Enhancement: An Experimental Study on a Series of Polymethine Dyes on Silver Nanoaggregates. *J. Phys. Chem. C*. 2016. 120(37): 21076-21081. doi: 10.1021/acs.jpcc.6b03785.
28. Z.-m. Qi, C. Chen, "Does Surface Enhanced Raman Scattering have another Enhancement Mechanism Except for the Electromagnetic and Chemical Enhancements?", in *Advanced Photonics 2016 (IPR, NOMA, Sensors, Networks, SPCCOM, SOF)* (Optical Society of America, Vancouver, 2016), p. SeW3E.6.
29. W. E. Smith. Practical understanding and use of surface enhanced Raman scattering/surface enhanced resonance Raman scattering in chemical and biological analysis. *Chem. Soc. Rev.* 2008. 37(5): 955-964. doi: 10.1039/b708841h.
30. L. Liu, D. Chen, H. Ma, W. Liang. Spectral Characteristics of Chemical Enhancement on SERS of Benzene-like Derivatives: Franck–Condon and Herzberg–Teller Contributions. *J. Phys. Chem. C*. 2015. 119(49): 27609-27619. doi: 10.1021/acs.jpcc.5b05910.
31. T. Vo-Dinh, A. Dhawan, S. J. Norton, C. G. Khoury, H.-N. Wang, V. Misra, M. D. Gerhold. Plasmonic Nanoparticles and Nanowires: Design, Fabrication and Application in Sensing. *J. Phys. Chem. C*. 2010. 114(16): 7480-7488. doi: 10.1021/jp911355q.
32. E. C. Le Ru, P. Etchegoin. Principles of Surface Enhanced Raman Spectroscopy and Related Plasmonic Effects. Oxford, UK: Elsevier B.V., 2009. 1st ed.
33. A. G. Brolo, D. E. Irish, B. D. Smith. Applications of surface enhanced Raman scattering to the study of metal-adsorbate interactions. *Applications of surface enhanced Raman scattering to the study of metal-adsorbate interactions*. 1997. 405(1): 29-44. doi: 10.1016/S0022-2860(96)09426-4.
34. K. Kneipp, H. Kneipp, I. Itzkan, R. R. Dasari, M. S. Feld. Surface-enhanced Raman scattering and biophysics. *Surface-enhanced Raman scattering and biophysics*. 2002. 14: R597-R624. doi.
35. C. Hendrich, J. Bosbach, F. Stietz, F. Hubenthal, T. Vartanyan, F. Träger. Chemical interface damping of surface plasmon excitation in metal nanoparticles a study by persistent spectral hole burning: a study by persistent spectral hole burning. *Chemical interface damping of surface plasmon excitation in metal nanoparticles a study by persistent spectral hole burning: a study by persistent spectral hole burning*. 2003. 76: 869. doi.
36. A. Champion, J. E. Ivanecky, C. M. Child, M. Foster. On the Mechanism of Chemical Enhancement in Surface-Enhanced Raman Scattering. *J. Am. Chem. Soc.* 1995. 117(47): 11807-11808. doi: 10.1021/ja00152a024.
37. Plasmonics: From Basics to Advanced Topics. Berlin: Springer, 2012. 1st ed.
38. P. N. Minh, O. Takahito, E. Masayosh, "Simulation using the finite difference time domain (FDTD) method", in *Fabrication of Silicon Microprobes for Optical Near-Field Applications* (CRC Press, 2002).

39. K. S. Yee. Numerical solution of initial boundary value problems involving maxwell's equations in isotropic media. Numerical solution of initial boundary value problems involving maxwell's equations in isotropic media. 1966. 14(3): 302-307. doi: 10.1109/tap.1966.1138693.
40. Y. Wang, K. Lee, J. Irudayaraj. Silver Nanosphere SERS Probes for Sensitive Identification of Pathogens. Silver Nanosphere SERS Probes for Sensitive Identification of Pathogens. 2010. 114(39): 16122-16128. doi: 10.1021/jp1015406.
41. "FDTD *Solutions* Reference Guide Release 7.5", (Lumerical Solutions, Inc., 2012).
42. Y. Hao, R. Mittra. FDTD Modeling of Metamaterials: Theory and Applications. Boston: Artech House, 2009. 1st ed.
43. D. M. Sullivan. Electromagnetic Simulation Using the FDTD Method. New York: IEEE Press, 2000. 1st ed.
44. J. Olavarría-Fullerton, R. A. Velez, S. Wells, M. J. Sepaniak, S. P. Hernández-Rivera, M. A. D. Jesús. Design and Characterization of Hybrid Morphology Nanoarrays as Plasmonic Raman Probes for Antimicrobial Detection. Appl. Spectrosc. 2013. 67(11): 1315-1322. doi: 10.1366/13-07001.
45. S. M. Wells, A. Polemi, N. V. Lavrik, K. L. Shuford, M. J. Sepaniak. Efficient Disc On Pillar Substrates for Surface Enhanced Raman Spectroscopy. Chem. Commun. 2011. 47: 3814-3816. doi: 10.1039/C0CC05577H.
46. A. J. Baca, J. Baca, J. M. Montgomery, L. R. Cambrea, P. Funcheon, L. Johnson, M. Moran, D. Connor. Mosaic-like Silver Nanobowl Plasmonic Crystals as Highly Active Surface-Enhanced Raman Scattering Substrates. J. Phys. Chem. C. 2015. 119(31): 17790-17799. doi: 10.1021/acs.jpcc.5b03824.
47. C. Hou, G. Meng, Q. Huang, Z. Chuhong, Z. Huang, B. Chen, K. Sun. Ag-Nanoparticle-Decorated Au-Fractal Patterns on Bowl-Like-Dimple Arrays on Al Foil as an Effective SERS Substrate for the Rapid Detection of PCBs. Chem. Commun. 2014. 50: 569-571. doi: 10.1039/C3CC46878J.
48. Y. Y. Huang, P. Chen, C. H. Wu, K. Hoshino, K. Sokolov, N. Lane, H. Y. Liu, M. Huebschman, E. Frenkel, J. X. J. Zhang. Screening and Molecular Analysis of Single Circulating Tumor Cells Using Micromagnet Array. Sci. Rep. 2015. 5(16047): 1-11. doi: 10.1038/srep16047.
49. S. D'Agostino, F. Della Sala. Silver Nanourchins in Plasmonics: Theoretical Investigation on the Optical Properties of the Branches. J. Phys. Chem. C. 2011. 115(24): 11934-11940. doi: 10.1021/jp202229y.
50. S. Gottheim, H. Zhang, A. O. Govorov, N. J. Halas. Fractal Nanoparticle Plasmonics: The Cayley Tree. ACS Nano. 2015. 9(3): 3284-3292. doi: 10.1021/acsnano.5b00412.

51. D. Bhandari, S. M. Wells, A. Polemi, I. I. Kravchenko, K. L. Shuford, M. J. Sepaniak. Stamping Plasmonic Nanoarrays on SERS-Supporting Platforms. *J. Raman Spectrosc.* 2011. 42(11): 1916-1924. doi: 10.1002/jrs.2940.
52. E. C. Le Ru, E. Blackie, M. Meyer, P. G. Etchegoin. Surface Enhanced Raman Scattering Enhancement Factors: A Comprehensive Study. *Surface Enhanced Raman Scattering Enhancement Factors: A Comprehensive Study.* 2007. 111: 13794. doi.
53. N. Valley, N. Greeneltch, R. P. Van Duyne, G. C. Schatz. A Look at the Origin and Magnitude of the Chemical Contribution to the Enhancement Mechanism of Surface-Enhanced Raman Spectroscopy (SERS): Theory and Experiment. *J. Phys. Chem. Lett.* 2013. 4(16): 2599-2604. doi: 10.1021/jz4012383.
54. J.-M. Nam, J.-W. Oh, H. Lee, Y. D. Suh. Plasmonic Nanogap-Enhanced Raman Scattering with Nanoparticles. *Acc. Chem. Res.* 2016. 49(12): 2746-2755. doi: 10.1021/acs.accounts.6b00409.
55. M.-G. Santiago, M. Ryuji, K. Manabu. Surface Enhanced Raman Scattering of Molecules in Metallic Nanogaps. *J. Opt.* 2015. 17(11): 1-14. doi: 10.1088/2040-8978/17/11/114001.
56. J. Perumal, T. Gong, D. U. S., K. D. Buddharaju, P. L. Guo-Qiang, M. Olivo, J. D. L., V. D. R. P. Development of Optimized Nanogap Plasmonic Substrate for Improved SERS Enhancement. *AIP Adv.* 2017. 7(5): 1-7. doi: 10.1063/1.4984769.
57. U. S. Dinish, F. C. Yaw, A. Agarwal, M. Olivo. Development of Highly Reproducible Nanogap SERS Substrates: Comparative Performance Analysis and its Application for Glucose Sensing. *Biosens. Bioelectron.* 2011. 26(5): 1987-1992. doi: 10.1016/j.bios.2010.08.069.
58. G. Lu, H. Li, S. Wu, P. Chen, H. Zhang. High-Density Metallic Nanogaps Fabricated on Solid Substrates used for Surface Enhanced Raman Scattering. *Nanoscale.* 2012. 4(3): 860-863. doi: 10.1039/c1nr10997a.
59. S.-C. Cheng, T.-C. Wen. Robust SERS Substrates with Massive Nanogaps Derived from Silver Nanocubes Self-Assembled on Massed Silver Mirror via 1,2-ethanedithiol Monolayer as Linkage and Ultra-Thin Spacer. *Mater. Chem. Phys.* 2014. 143(3): 1331-1337. doi: 10.1016/j.matchemphys.2013.11.043.
60. Y. Zhu, R. A. Dluhy, Y. Zhao. Development of Silver Nanorod Array Based Fiber Optic Probes for SERS Detection. *Sens. Actuators, B.* 2011. 157(1): 42-50. doi: 10.1016/j.snb.2011.03.024.
61. M. A. De Jesús, K. S. Giesfeldt, J. M. Oran, N. A. Abu-Hatab, N. V. Lavrik, M. J. Sepaniak. Nanofabrication of Densely Packed Metal—Polymer Arrays for Surface-Enhanced Raman Spectrometry. *Appl. Spectrosc.* 2005. 59(12): 1501-1508. doi: 10.1366/000370205775142557.
62. A. Polemi, S. M. Wells, N. V. Lavrik, M. J. Sepaniak, K. L. Shuford. Dispersion Characteristics in Disk-on-Pillar Array Nanostructures for Surface-Enhanced Raman Spectroscopy. *J. Phys. Chem. C.* 2011. 115(28): 13624-13629. doi: 10.1021/jp2032059.

63. C. L. Haynes, R. P. Van Duyne. Plasmon-Sampled Surface-Enhanced Raman Excitation Spectroscopy. *J. Phys. Chem. B.* 2003. 107(30): 7426-7433. doi: 10.1021/jp027749b.
64. L.-J. Wan, M. Terashima, H. Noda, M. Osawa. Molecular Orientation and Ordered Structure of Benzenethiol Adsorbed on Gold(111). *J. Phys. Chem. B.* 2000. 104(15): 3563-3569. doi: 10.1021/jp993328r.
65. C. M. Whelan, M. R. Smyth, C. J. Barnes. HREELS, XPS, and Electrochemical Study of Benzenethiol Adsorption on Au(111). *Langmuir.* 1999. 15(1): 116-126. doi: 10.1021/la9806202.
66. J. H. Barton, R. C. Rumpf, R. W. Smith, C. Kozikowski, P. Zellner. All-Dielectric Frequency Selective Surfaces with Few Number of Periods. *Prog. Electromagn. Res., B.* 2012. 41: 269-283. doi: 10.2528/PIERB1204240.
67. J. Hu, C. R. Menyuk. Understanding Leaky Modes: Slab Waveguide Revisited. *Understanding Leaky Modes: Slab Waveguide Revisited.* 2009. 1(1): 58-106. doi: 10.1364/AOP.1.000058.
68. Y. Gu, S. Xu, H. Li, S. Wang, M. Cong, J. R. Lombardi, W. Xu. Waveguide-Enhanced Surface Plasmons for Ultrasensitive SERS Detection. *J. Phys. Chem. Lett.* 2013. 4: 3153-3157. doi: 10.1021/jz401512k.
69. H. Wang, Y. Wang, Y. Wang, W. Xu, S. Xu. Modulation of Hot Regions in Waveguide-Based Evanescent-Field-Coupled Localized Surface Plasmons for Plasmon-Enhanced Spectroscopy. *Photonics Res.* 2017. 5(5): 527-535. doi: 10.1364/prj.5.000527.
70. S. Wang, Z. Wu, L. Chen, Y. Gu, H. Wang, S. Xu, W. Xu. Leaky Mode Resonance of Polyimide Waveguide Couples Metal Plasmon Resonance for Surface-Enhanced Raman Scattering. *J. Phys. Chem. C.* 2015. 119(44): 24942-24949. doi: 10.1021/acs.jpcc.5b04791.
71. Y. Yuan, N. Panwar, S. H. K. Yap, Q. Wu, S. Zeng, J. Xu, S. C. Tjin, J. Song, J. Qu, K.-T. Yong. SERS-Based Ultrasensitive Sensing Platform: An Insight into Design and Practical Applications. *Coord. Chem. Rev.* 2017. 337: 1-33. doi: 10.1016/j.ccr.2017.02.006.
72. K. H. Drexhage. Fluorescence efficiency of laser dyes. *J. Res. Natl. Bur. Stand.* 1976. 80A(3): 421 - 428. doi: 10.6028/jres.080A.044.
73. T. Vosgröne, A. J. Meixner. Surface- and Resonance-Enhanced Micro-Raman Spectroscopy of Xanthene Dyes: From the Ensemble to Single Molecules. *ChemPhysChem.* 2005. 6(1): 154-163. doi: 10.1002/cphc.200400395.
74. H. Watanabe, N. Hayazawa, Y. Inouye, S. Kawata. DFT Vibrational Calculations of Rhodamine 6G Adsorbed on Silver: Analysis of Tip-Enhanced Raman Spectroscopy. *J. Phys. Chem. B.* 2005. 109(11): 5012-5020. doi: 10.1021/jp045771u.
75. R. Hillenbrand, T. Taubner, F. Keilmann. Phonon-enhanced light matter interaction at the nanometre scale. *Nature.* 2002. 418: 159-162. doi: 10.1038/nature00899.

76. J. Zhao, L. Jensen, J. Sung, S. Zou, G. C. Schatz, R. P. Van Duyne. Interaction of Plasmon and Molecular Resonances for Rhodamine 6G Adsorbed on Silver Nanoparticles. *J. Am. Chem. Soc.* 2007. 129(24): 7647-7656. doi: 10.1021/ja0707106.
77. V. I. Gavrilenko, M. A. Noginov. Ab Initio Study of Optical Properties of Rhodamine 6G Molecular Dimers. *J. Chem. Phys.* 2006. 124(4): 0443011-0443016. doi: 10.1063/1.2158987.
78. G. Lu, B. Shrestha, A. J. Haes. Importance of Tilt Angles of Adsorbed Aromatic Molecules on Nanoparticle Rattle SERS Substrates. *Importance of Tilt Angles of Adsorbed Aromatic Molecules on Nanoparticle Rattle SERS Substrates.* 2016. 120(37): 20759-20767. doi: 10.1021/acs.jpcc.6b02023.
79. W. Gan, G. Gonella, M. Zhang, H.-L. Dai, L. S., E.-S. M. A. Communication: Reactions and adsorption at the surface of silver nanoparticles probed by second harmonic generation. *Communication: Reactions and adsorption at the surface of silver nanoparticles probed by second harmonic generation.* 2011. 134(4): 041104. doi: 10.1063/1.3548668.
80. S. Asiaei, P. Nieva, M. M. Vijayan. Fast Kinetics of Thiolic Self-Assembled Monolayer Adsorption on Gold: Modeling and Confirmation by Protein Binding. *Fast Kinetics of Thiolic Self-Assembled Monolayer Adsorption on Gold: Modeling and Confirmation by Protein Binding.* 2014. 118(47): 13697-13703. doi: 10.1021/jp509986s.
81. R. A. Velez, N. Lavrik, I. I. Kravchenko, M. Sepaniak, M. A. De Jesus. EXPRESS: Surface-Enhanced Raman Scattering (SERS) Studies of Disc-on-Pillar (DOP) Arrays: Contrasting Enhancement Factor with Analytical Performance. *EXPRESS: Surface-Enhanced Raman Scattering (SERS) Studies of Disc-on-Pillar (DOP) Arrays: Contrasting Enhancement Factor with Analytical Performance.* doi: 10.1177/0003702819846503.

APPENDIX

Appendix 1. BT SAM TEMPORAL STUDY

Introduction

This study was executed to assess the adequacy of the BT incubation time reported in Section 4.2.4 as requested by the reviewers of the following article accepted by Applied Spectroscopy:

R. A. Velez, N. V. Lavrik, I. I. Kravchenko, M. J. Sepaniak, M. A. D. Jesus. **Surface-Enhanced Raman Scattering (SERS) Studies of Disc-On-Pillar (DOP) Arrays: Contrasting Enhancement Factor with Analytical Performance.** Appl. Spectrosc. 2019. ##(##): #### - #####. doi: 10.1177/0003702819846503.

Experimental Details

A water bath was prepared on top of a magnetic stirring plate using a shallow tray and an automatic temperature controlled recirculator (Thermo Scientific, Arctic S150-A10). Approximately 7.5 mL of ethanolic BT solutions with a final concentration of 1×10^{-3} M and 1×10^{-5} M added to individual petri dishes and equilibrated to 26.5°C. Individual chips were incubated for 15 minutes in approximately with constant stirring. A glass-coated magnetic stir bar (Cole-Palmer Item EW-04769-50) was used to minimize adsorption of BT molecules to surfaces other than the chip. Afterwards the chip was dipped in DIW followed by rinsing with copious amounts of DIW and drying with N₂. Raman spectra where obtained in duplicate of p160 and p520. The chips were returned to their original solutions and incubated for a total of

1200 minutes (20 hours). The DIW rinse and drying process was repeated and additional spectra obtained for p160 and p520.

Spectra were obtained using a JY-Horiba LabRAM HR800 Raman microscope equipped with a HeNe laser ($\lambda = 632.81$ nm, power = 7.50 mW) and a long working distance 50x objective (NA = 0.45 μm , effective spot size = 2.0 μm). Individual spectra were measured with 1 second acquisition time. A 600 nm grating, 400 μm aperture and 200 μm slit width were used in all SERS measurements. The spectral range was from 200 cm^{-1} to 4000 cm^{-1} . All spectra were baseline corrected and background subtracted.

Results and Discussion

The spectra (Figure A1-1) do not depict significant differences in band response between 10^{-5} M and 10^{-3} M at each incubation interval for p160 and p520. There was a slight redshift from 1074 cm^{-1} to 1072 cm^{-1} for samples corresponding to the incubation period of 1200 minutes. The 2 cm^{-1} represents roughly a -0.2% difference in Raman shift. Any difference less than 5 cm^{-1} is not considered significant change in Raman shift.

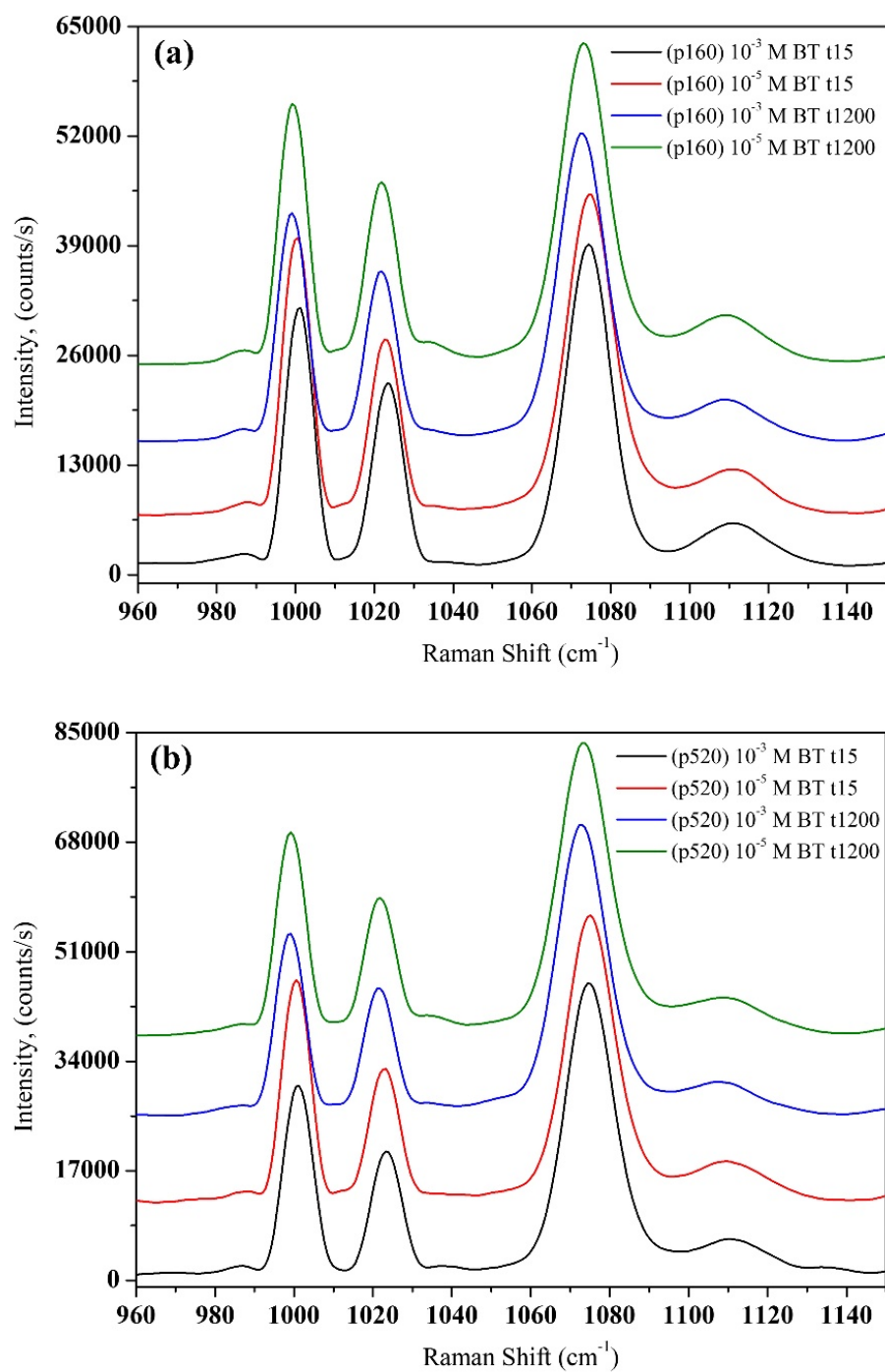


Figure A1-1: Mean SERS spectra for 1.0×10^{-3} M and 1.0×10^{-5} BT using the $24 \mu\text{m} \times 24 \mu\text{m}$ DOP region for (a) p160 and (b) p520. All spectra are offset in the y-axis for clarity. A slight red shift ($< 2 \text{ cm}^{-1}$) is observed for samples corresponding to the 1200 minutes incubation period. This shift is a -0.2% difference and is not considered significant.

The relative difference between sample intensities as per the following equation:

$$\text{Relative Intensity Difference} = \left(\frac{I_{t1200} - I_{t15}}{I_{t15}} \right) \times 100 \quad (\text{A1-1})$$

where I_{t15} and I_{t1200} correspond to the C-S band intensity for the incubation times at 15 and 1200 minutes respectively.

Table A1-1 depicts the differences calculated for the different sample iterations. The following can be established from the results:

- The relative differences between incubation periods of 15 and 1200 minutes are not considered significant ($< 1.5\%$). The greatest difference is observed for the higher concentration ($1 \times 10^{-3} \text{ M}$) although considered insignificant.
- The relative differences between concentrations within the same incubation time for each pitch is not considered significant ($< 1\%$).

Table A6-1: C-S band intensity (cnts/s) of 10^{-3} M and 10^{-5} M BT at incubation periods of 15 minutes and 1200 minutes using p160 and p520 DOP plasmonic systems.

| DOP | [BT] M | Intensity (cnts/s) | | % Relative Difference | | |
|------|--------------------|--------------------|---------|-----------------------|---|---|
| | | t15 | t1200 | t15 vs. t1200 | $10^{-3} \text{ M vs. } 10^{-5} \text{ M}$ (t15) | $10^{-3} \text{ M vs. } 10^{-5} \text{ M}$ (t1200) |
| p160 | 1×10^{-3} | 38491.3 | 38051.3 | -1.1 | -0.5 | 0.2 |
| p160 | 1×10^{-5} | 38313.4 | 38134.5 | -0.5 | | |
| p520 | 1×10^{-3} | 45948.9 | 45238.6 | -1.5 | -0.5 | 0.2 |
| p520 | 1×10^{-5} | 45250.3 | 45544.0 | 0.6 | | |

In summary, the data did not show significant differences between incubation times and BT concentration used. This suggests that the conditions reported to render a BT layer on the DOP system, which are 15 minutes incubation time with a 1×10^{-5} M, are considered adequate for SSEF assessment. Furthermore, the data is consistent with reported low ΔG_{ads} (-7.40 kcal/mol, -8.8 kcal/mol) as well as with fast thiol adsorption kinetics.⁷⁸⁻⁸⁰

Appendix 2. MAXIMUM ALLOWABLE PILLARS (MAP)

Introduction

This section describes the calculations for determining the maximum number of pillars (MAP) that can occupy the laser beam spot as reported elsewhere.⁸¹

Determination of MAP

The number of pillars within the spot is accounted for by the value of MAP, which is based on the laser spot area (A_L) and the area occupied by one pillar (A_P) as per the array pitch (Eq. A2-1 to A2-3). The beam waist of the laser is presumed to have a circular shape based on the optical imaging. A schematic representation of MAP is shown (Figure A2-1).

$$A_P = \frac{\text{pillar}}{\text{pitch}^2} \quad (\text{A2-1})$$

$$A_L = \pi r_L^2 \quad (\text{A2-2})$$

were

r_L = laser spot radius

$$\text{MAP} = A_P \times A_L = \frac{\text{pillar} \times \pi r_L^2}{\text{pitch}^2} \quad (\text{A2-3})$$

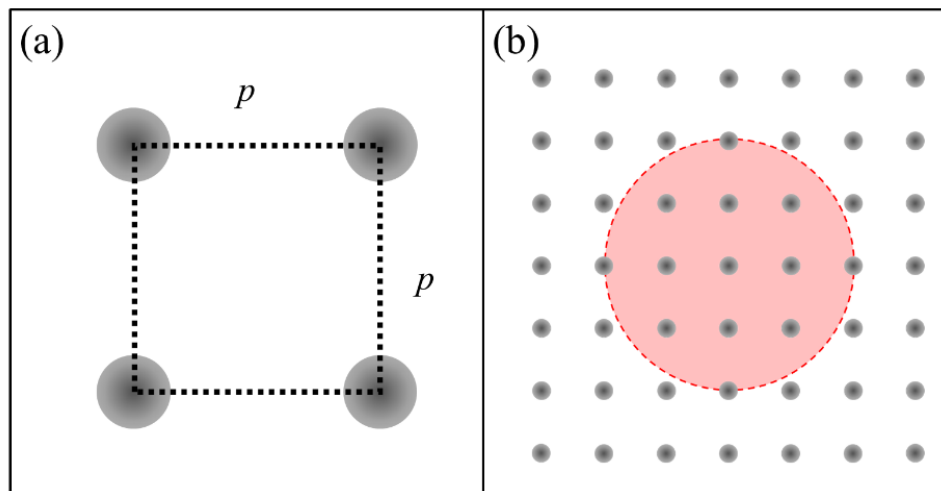


Figure A2-1: Schematic representation (not to scale) of the Maximum Allowable Pillar (MAP). (a) The area occupied by one DOP, A_p . (b) The laser beam spot, A_L , (represented by the red circle) confining an array of disc-on-pillars (DOP).

MAP plays a significant role for the DOP systems studied because it normalizes the SERS response for all periodicities thus allowing for a rational comparison between pillar arrays of different pitch values. For instance, a 50x objective with a 2 μm beam spot diameter will have an estimate MAP of 123 pillars for a 160 nm pitch (denoted as p160) and 12 pillars for 520 nm pitch (denoted as p520). Considering a 4 \times 4 array, the 16 pillars corresponding to p160 will be located within the beam spot whereas only 12 of the 16 pillars will fit for the p520. However, a 2 \times 2 array will accommodate all pillars within the laser spot regardless of the inter-pillar spacing, thus allowing a direct assertion of the SERS activity for all arrays because all parameters, except for the pitch, are kept constant. Under the current instrumentation conditions, normalization with MAP is required for the periodicities studied with DOP arrangements greater than 2 \times 2.

Appendix 3. DOP ARRAYS: SUPPLEMENTAL INFORMATION

2×2 Disc-On-Pillar Arrays

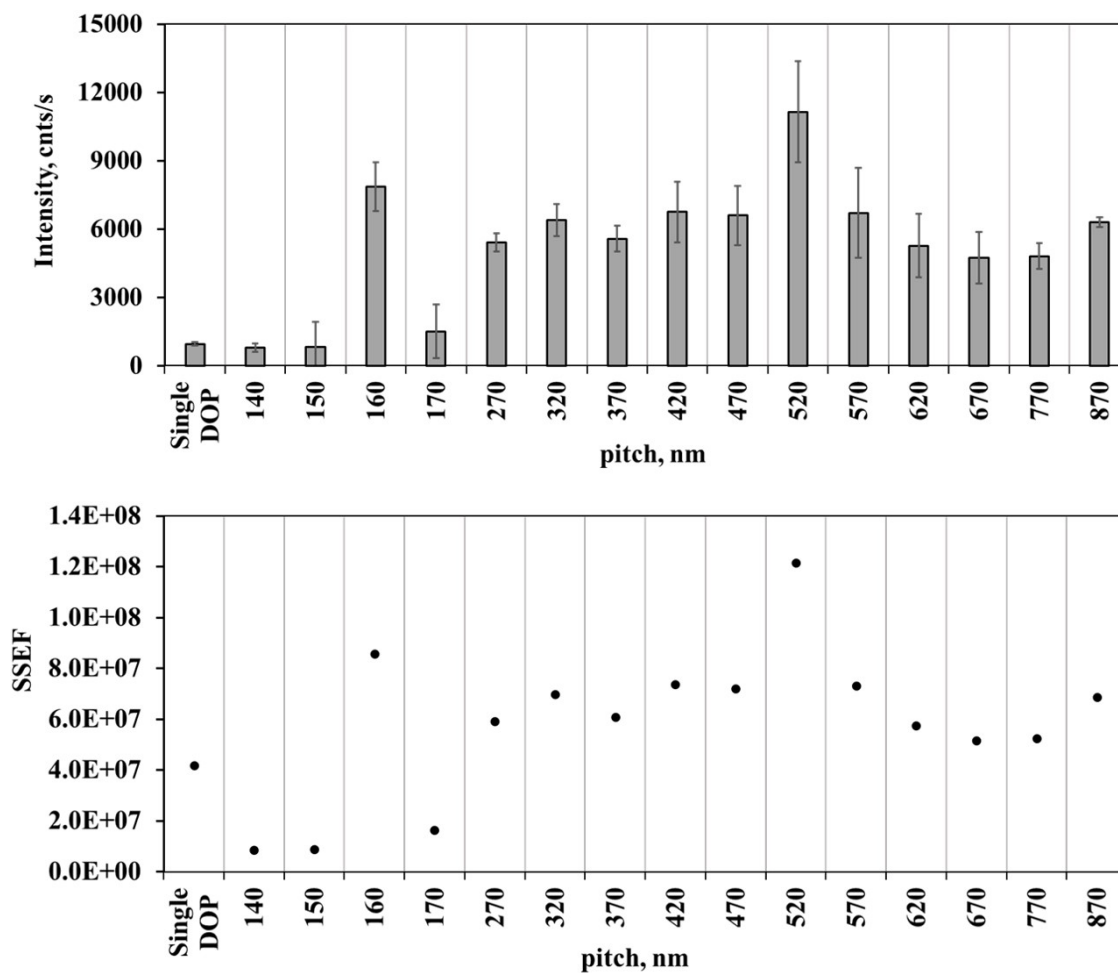


Figure A3-1: (top) BT SERS response for 2×2 DOP arrays and a single pillar. The total number of pillars probed ($n = 4$) was the same for all periodicities. The error bars are the standard deviation of triplicate measurements made around the center of the array. The CV calculated for each pitch ranged from 4.0% to 8.9%. (bottom) Calculated SSEF for single pillar and periodic arrays. An excellent correlation ($R^2 = 1.000$) was obtained for SSEF and SERS raw signal.

4 × 4 Disc-On-Pillar Arrays

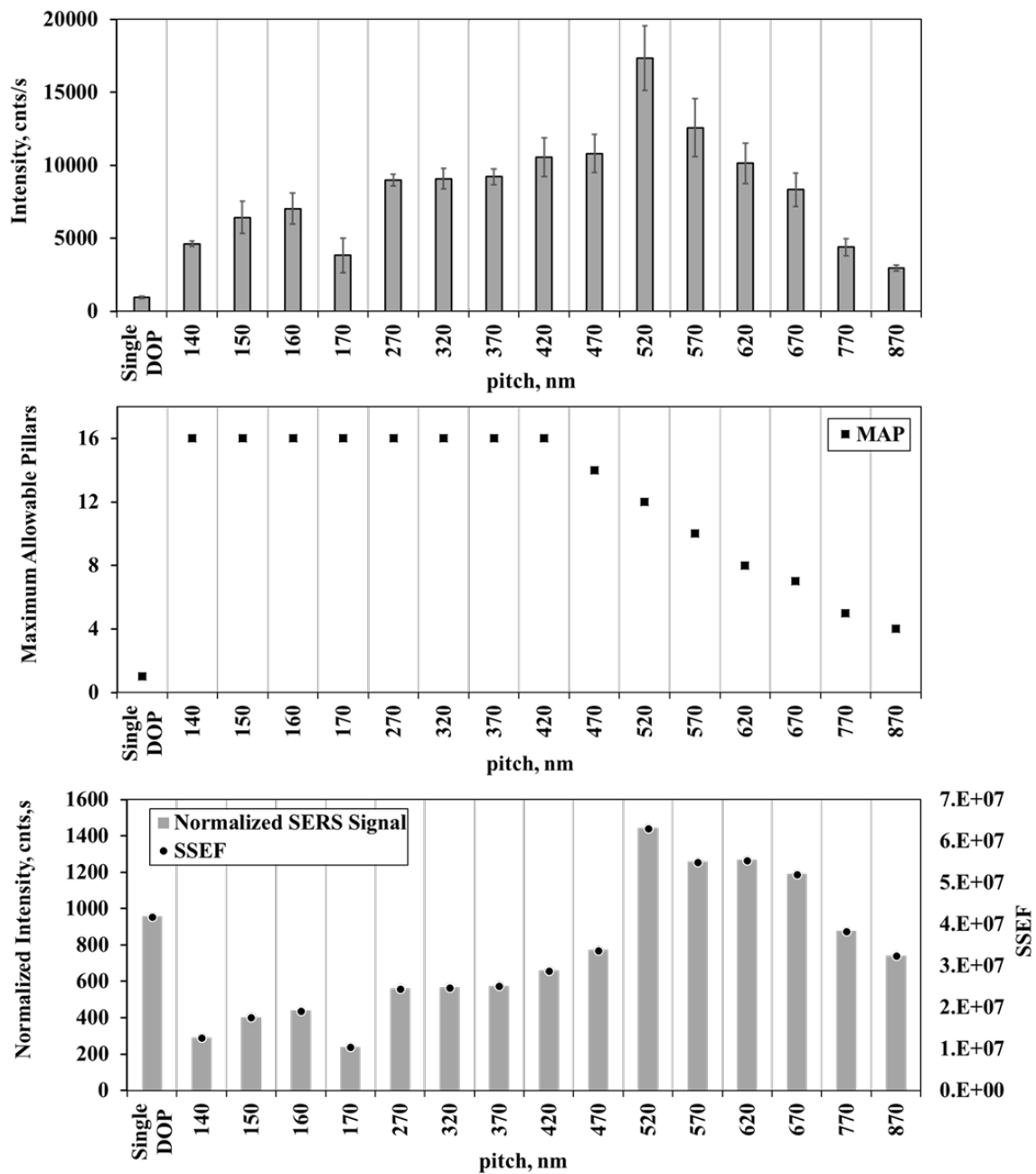


Figure A3-2: BT SERS activity using 4 × 4 DOP arrays. The error bars are the standard deviation of triplicate measurements made around the center of the array. The calculated CV for each period ranged from 3.1% to 9.2%. The area for 1075 cm⁻¹ (ν_{C-S}) was normalized with the MAP of each pitch for a 2 μm laser spot.

8 × 8 Disc-On-Pillar Arrays

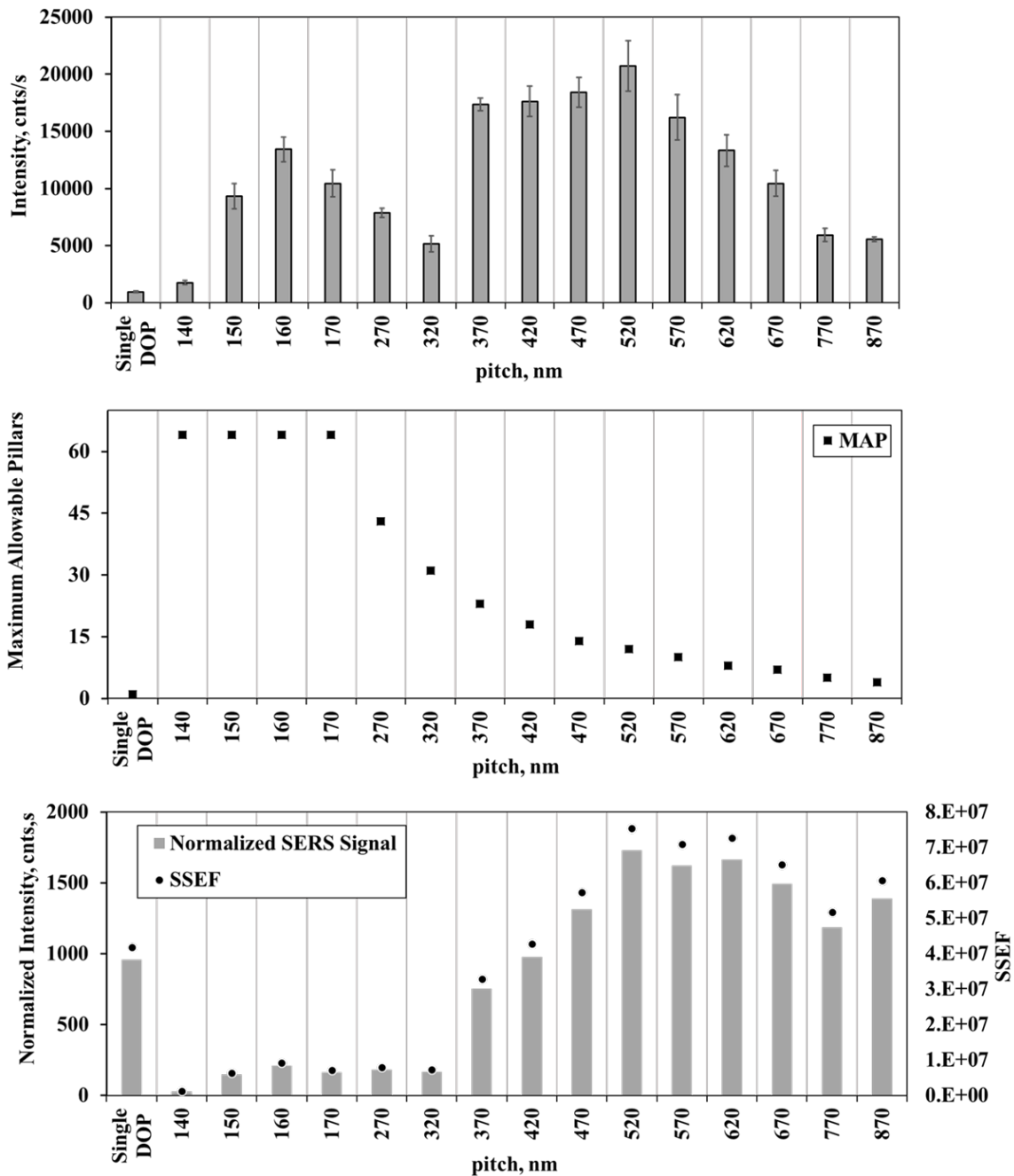


Figure A3-3: BT SERS activity using 8 × 8 DOP arrays. The error bars are the standard deviation of triplicate measurements made around the center of the array. The calculated CV for each period ranged from 2.6% to 9.6%. The area for 1075 cm⁻¹ (ν_{C-S}) was normalized with the MAP of each pitch for a 2 μm laser spot.

24 $\mu\text{m} \times 24 \mu\text{m}$ Disc-On-Pillar Arrays

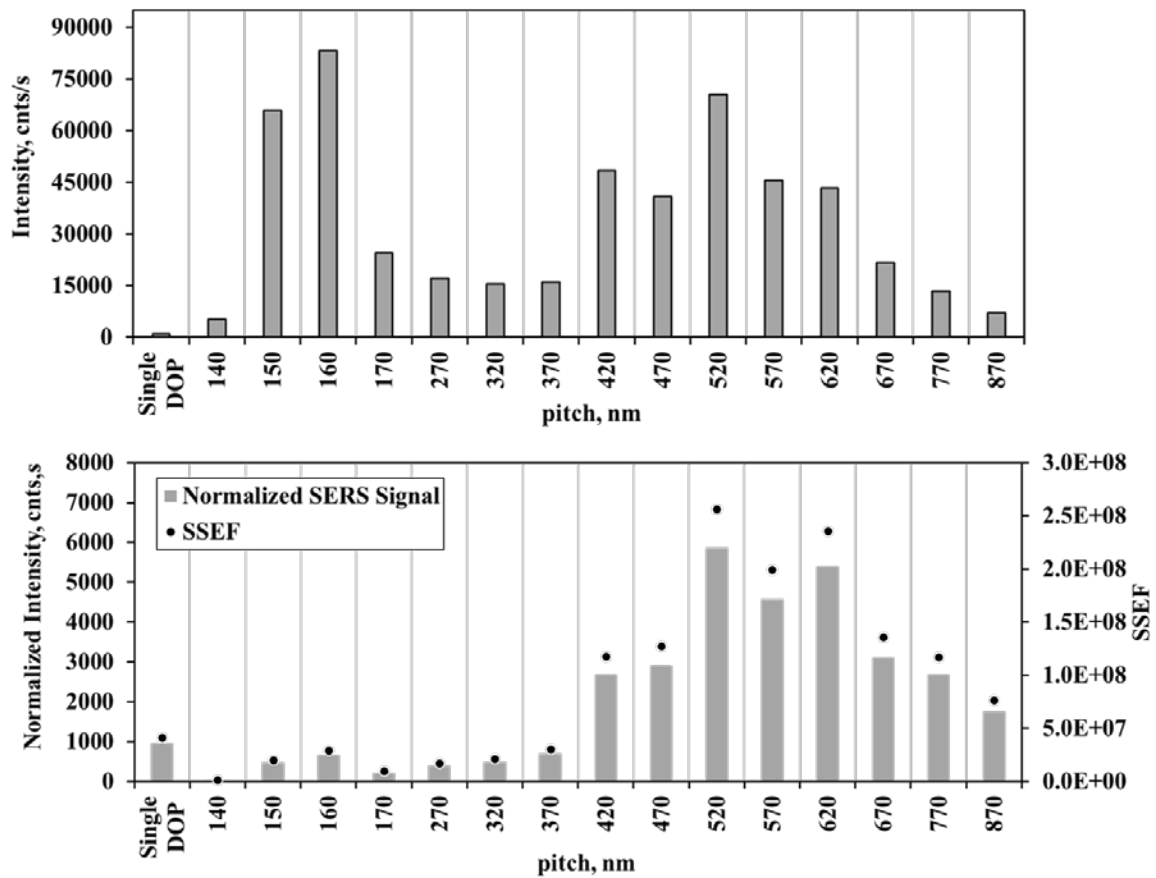


Figure A3-4: (top) Average BT SERS response for the full 24 $\mu\text{m} \times 24 \mu\text{m}$ array region as determined by LabSpec Software. (bottom) BT SERS response after normalization with MAP and calculated SSEF.

Appendix 4. DOP PITCH ORDER RESPONSE FACTOR (Φ)

Introduction

This section describes the calculations for determining the DOP pitch order response factor as reported elsewhere.⁸¹

Determination of Φ

The DOP pitch order response factor (Φ) between two arrays of the 520 nm pitch was calculated with the non-normalized SERS response of the BT 1075 cm^{-1} band using the following equation:

$$\Phi_{2,1} = \left(\frac{\text{SERS}_2}{\text{SERS}_1} \right) \quad (\text{A4-1})$$

where SERS_1 and SERS_2 correspond to SERS response of two different arrays the latter being the higher order array system (as per responses depicted in Table A6-2).

Table A6-2: SERS response of the BT for various arrays at p520 nm and single pillar.

| Pillar Arrangement | BT 1075 cm ⁻¹ Intensity (cnts/s.) |
|---|---|
| Single DOP | 956.67 |
| 2 × 2 | 11148.07 |
| 4 × 4 | 17331.30 |
| 8 × 8 | 20729.80 |
| 24 μm ² × 24 μm ² | 87412.20 |

Consider the performance of 2 × 2 and 8 × 8 pillar arrays. Using the BT band response provided in Table A6-2 renders a stronger SERS response for the 8 × 8 over 2 × 2 by a factor of 1.9. The following is the calculation:

$$\Phi_{2,1} = \left(\frac{20729.80 \text{ cnts/s}}{11148.07 \text{ cnts/s}} \right) = 1.9$$